Copyright Warning & Restrictions

The copyright law of the United States (Title 17, United States Code) governs the making of photocopies or other reproductions of copyrighted material.

Under certain conditions specified in the law, libraries and archives are authorized to furnish a photocopy or other reproduction. One of these specified conditions is that the photocopy or reproduction is not to be "used for any purpose other than private study, scholarship, or research." If a, user makes a request for, or later uses, a photocopy or reproduction for purposes in excess of "fair use" that user may be liable for copyright infringement,

This institution reserves the right to refuse to accept a copying order if, in its judgment, fulfillment of the order would involve violation of copyright law.

Please Note: The author retains the copyright while the New Jersey Institute of Technology reserves the right to distribute this thesis or dissertation

Printing note: If you do not wish to print this page, then select "Pages from: first page # to: last page #" on the print dialog screen

The Van Houten library has removed some of the personal information and all signatures from the approval page and biographical sketches of theses and dissertations in order to protect the identity of NJIT graduates and faculty.

ABSTRACT

OPTICAL PROPERTIES AND CARRIER TRANSPORT IN Si/$Si_{1-x}Ge_x$ NANOSTRUCTURES

by
Eun Kyu Lee

Defect-free epitaxial growth of Ge on a ~4 % lattice-mismatched single-crystal Si substrate is achieved using reduced dimension nanoscale heterostructures, where efficient structural relaxation might occur due to an enhanced adatom migrations and high surface-to-volume ratio. For development of novel electronic or optical devices based on these novel structures, understanding of their electrical and optical properties is crucial. This study explores the optical properties and carrier transport in two different types of Si/$Si_{1-x}Ge_x$ nanostructures: Ge nanowires (NWs) forming nanoscale heterojunctions with Si substrates and multilayers of SiGe clusters embedded into a Si matrix.

Micron-long Ge nanowires grown on n^+ (100) and p^+ (111) Si substrates exhibit distinct current-voltage (*I-V*) characteristics, which are explained using a model of an abrupt and defect-free Ge NW/Si substrate heterointerfaces. From the measurements on Si/SiGe cluster superlattices (SLs) where SiGe clusters are vertically aligned due to strain-induced self-organization, a series of step-like structures are observed in the *I-V* characteristics obtained using mapping of electrical characteristics by a scanning-tunneling-microscope (STM). The origin of this step-like *I-V* behavior and distinct peaks in differential conductivity is suggestively explained by a conduction energy band configuration that considers phonon-assisted carrier transfer at the interfaces between Si separating layers and Ge-rich SiGe clusters.

Optical measurements show that the photoluminescence (PL) intensity in Si/SiGe cluster SL exhibits excitation dependent thermal quenching under continuous wave (CW) excitation by an Ar^+ laser with the excitation intensities of 0.1–10 W/cm^2. A novel mechanism, where nonradiative carrier recombination is controlled by a competition between hole tunneling and hole thermionic emission over the valence band energy barriers at Si/SiGe heterointerfaces is suggested.

In addition, the carrier transitions at a high photoexcitation using Q-switched pulsed Nd:YAG laser are found to be mediated by Auger processes with high energy Auger holes repopulating Si barriers in valence energy band. An efficient light emission due to radiative recombination of electron-hole condensates in Si separating layers of the Si/SiGe clusters SL is observed with a lifetime approaching 10^{-8} s. These results, attributed to a mechanism similar to "Auger fountain" in quantum wells with type-II energy band alignment, indicate a new route toward light-emitters monolithically integrated into CMOS environment.

OPTICAL PROPERTIES AND CARRIER TRANSPORT IN Si/ $Si_{1-x}Ge_x$ NANOSTRUCTURES

Eun Kyu Lee

Advisor: Dr. Leonid Tsybeskov

A Dissertation
Submitted to the Faculty of
New Jersey Institute of Technology
in Partial Fulfillment of the Requirements for the Degree of
Doctor of Philosophy in Electrical Engineering

Department of Electrical and Computer Engineering

May 2008

APPROVAL PAGE

OPTICAL PROPERTIES AND CARRIER TRANSPORT IN Si/ $Si_{1-x}Ge_x$ NANOSTRUCTURES

Eun Kyu Lee

Apr. 28, 08

Dr. Leonid Tsybeskov, Dissertation Advisor — Date
Associate Professor of Electrical and Computer Engineering, NJIT

Apr. 28, 08

Dr. Haim Grebel, Committee Member — Date

4/28/08

Dr. Durga Misra, Committee Member — Date
Professor of Electrical and Computer Engineering, NJIT

04/28/08

Dr. Andrei Sirenko, Committee Member — Date
Assistant Professor of Physics, NJIT

April 28, 2008

Dr. Marek Sosnowski, Committee Member — Date
Professor of Electrical and Computer Engineering, NJIT

BIOGRAPHICAL SKETCH

Author: Eun Kyu Lee

Degree: Doctor of Philosophy

Date: May 2008

Undergraduate and Graduate Education:

- Doctor of Philosophy in Electrical Engineering,
  New Jersey Institute of Technology, Newark, NJ, 2008

- Master of Science in Electrical Engineering,
  New Jersey Institute of Technology, Newark, NJ, 2004

- Bachelor of Science in Electrical Engineering,
  Seoul National University, Seoul, Korea, 1998

Major: Electrical Engineering

Presentations and Publications:

- Oral Conference Presentations

E.-K. Lee, B. V. Kamenev, T. I. Kamins, J.-M. Baribeau, D. J. Lockwood and L. Tsybeskov, "Photoluminescence excitation dependence in three-dimensional Si/SiGe nanostructures", Material Research Society Meeting, Boston, MI, December 2006.

E.-K. Lee, B. V. Kamenev, T. I. Kamins, S. Sharma and L. Tsybeskov, "Carrier transport in Ge nanowires/Si substrate heterojunction", American Physics Society Meeting, Baltimore, MD, March 2006.

- Poster Conference Presentations

H.-Y. Chang, E.-K. Lee, B. V. Kamenev, J.-M. Baribeau, D. J. Lockwood and L. Tsybeskov, "Optical properties of multiple, delta-doped Si:B/Si layers", Material Research Society Meeting, Boston, MI, December 2006.

V. Sharma, E.-K. Lee, B. V. Kamenev, T. I. Kamins, R. S. Williams and L. Tsybeskov, "Optical and electrical properties of one-dimensional Ge nanowires/Si substrate heterojunctions", NJIT Provost's Student Research Day, April 2005.

E.-K. Lee, B. V. Kamenev, P. A. Forsh, T. I. Kamins and L. Tsybeskov, "Carrier transport in one-dimensional Ge nanowires/Si substrate heterojunctions", Material Research Society Meeting, Boston, MI, December 2004.

- Journal Publications

L. Tsybeskov, E.-K. Lee, H.-Y. Chang, B. V. Kamenev, D. J. Lockwood, J.-M. Baribeau and T. I. Kamins, "Three-dimensional silicon-germanium nanostructures for CMOS compatible light emitters and optical interconnects", Advances in Optical Technologies, accepted for publication, April 2008.

D. J. Lockwood, J.-M. Baribeau, B. V. Kamenev, E.-K. Lee and L. Tsybeskov, "Structural and optical properties of three-dimensional $Si_{1-x}Ge_x$/Si nanostructures", Semiconductor Science and Technology, in press.

E.-K. Lee, L. Tsybeskov and T. I. Kamins, "Photoluminescence thermal quenching in three-dimensional multilayer Si/SiGe nanostructures", Applied Physics Letters **92** (3), 033110-033113 (2008).

E.-K. Lee, L. Tsybeskov, S. Sharma and T. I. Kamins, "Carrier transport in Ge nanowire/Si substrate heterojunctions", Journal of Applied Physics **101** (10), 104303-104304 (2007).

B. V. Kamenev, E.-K. Lee, H.-Y. Chang. H. Han, H. Grebel, T. I. Kamins and L. Tsybeskov, "Excitation-dependent photoluminescence in Ge/Si Stranski-Krastanov nanostructures", Applied Physics Letters, **89** (15), 153106-153103(2006).

- Conference Proceedings Publications

E.-K. Lee, B. V. Kamenev, T. I. Kamins, J.-M. Baribeau, D. J. Lockwood and L. Tsybeskov, "Photoluminescence excitation dependence in three-dimensional Si/SiGe nanostructures, Materials Research Society Symposium Proceedings **958**, 63-68 (2007).

H.-Y. Chang, E.-K. Lee, B. V. Kamenev, J.-M. Baribeau, D. J. Lockwood and L. Tsybeskov, "Optical properties of multiple, delta-doped Si:B/Si layers", Materials Research Society Symposium Proceedings **958,** 49-54 (2007).

E.-K. Lee, B. V. Kamenev, P. A. Forsh, T. I. Kamins and L. Tsybeskov, "Carrier transport in one-dimensional Ge Nanowires/Si substrate heterojunctions", Materials Research Society Symposium Proceedings **832**, 335-340 (2005).

L. Tsybeskov, B. Kamenev, V. Sharma, E. K. Lee, P. Fosh, T. Kamins and S. Williams, "Optical and electrical properties of Ge nanowire-Si substrate one-dimensional heterojunctions", American Physical Society Meeting Abstracts, 1010 (2004).

- Papers in Progress

E.-K. Lee, L. Tsybeskov, A. M. Bratkovsky, T. I. Kamins, D. J. Lockwood and J.-M. Baribeau, "Auger-mediated electron-hole plasma condensation in three-dimensional silicon/silicon-germanium nanostructures".

E.-K. Lee, L. Tsybeskov, D. J. Lockwood and J.-M. Baribeau, "Mapping of differential conductance in vertically self-aligned SiGe nanoclusters using scanning tunneling microscopy".

To my parents, Sang-Hoon Lee and Young-Ok Choi for their support and love.

ACKNOWLEDGEMENT

First and foremost, I would like to express my deepest gratitude for my thesis advisor, Dr. Leonid Tsybeskov, for the guidance, inspiration, and support throughout this research project and thesis.

I would also like to thank Dr. Haim Grebel, Dr. Durga Misra, Dr. Andrei Sirenko and Dr. Marek Sosnowski for serving as members of my committee.

My thanks also go to Dr. Ted Kamins and Dr. David Lockwood for providing the samples and many valuable feedbacks throughout this research.

Last, but not least, my parents, Sang-Hoon Lee and Young-Ok Choi, receive my deepest gratitude and love for their dedication and many years of support.

TABLE OF CONTENTS

Chapter	Page
1 INTRODUCTION	1
2 BACKGROUND	4
2.1 Vapor-Liquid-Solid and Other Mechanisms of Nanowire Growth	4
2.2 Stranski-Krastanov Growth Mechanism of Si/SiGe Nanostructures	10
2.3 Si/Ge Heterojunction Band Discontinuities	12
2.4 Characterization of Low-dimensional Nanostructures	18
2.4.1 Properties of Nanowires	18
2.4.2 Properties of Si/SiGe Clusters	31
3 EXPERIMENTAL	37
3.1 Samples and Contacts	38
3.1.1 Ge Nanowires/Si Substrate Samples	38
3.1.2 Si/SiGe Clusters Superlattice Samples	43
3.1.3 Contact Fabrication	46
3.2 Measurement Setup and Procedure	48
3.2.1 Electrical Measurements	48
3.2.2 Optical Measurments	51
4 RESULTS AND DISCUSSION	54
4.1 Ge Nanowires/Si Substrate Heterosutructures	54
4.1.1 Room Temperature DC Conductivity	55
4.1.2 Room Temperature AC Conductivity	57
4.1.3 DC Conductivity Temperature Dependence	62

TABLE OF CONTENTS
(Continued)

Chapter **Page**

4.1.4 Carrier Transport in Ge Nanowires/Si Substrate Heterojunctions 67

4.2 Si/SiGe Clusters Superlattices 72

4.2.1 Carrier Transport in Si/SiGe Clusters Superlattices 72

4.2.2 Low Temperature Photoluminescence 82

4.2.3 Photoluminescence Temperature Dependence 85

4.2.4 Photoluminescence Thermal Quenching in Si/SiGe Clusters Superlattices 90

4.2.5 Electroluminescence 93

4.2.6 Photoluminescence under High Intensity Excitation 96

4.2.7 Electron-hole Condensate and Carrier Relaxation in Si/SiGe Clusters Superlattice 103

5 CONCLUSION 107

5.1 Summary of Conclusions 107

5.2 Final Thoughts 108

REFERENCES 109

LIST OF TABLES

Table **Page**

3.1 Structural data of Si/SiGe cluster SL samples; number of periods *N*; SiGe cluster heights d_{SiGe}; Si separating layer thickness d_{Si} 43

LIST OF FIGURES
(Continued)

Figure		Page
2.1	Au-Ge phase diagram showing three states along the isothermal line; (I) alloying, (II) nucleation and (III) axial growth	5
2.2	Schematic representation of NW growth mechanism	8
2.3	In situ high temperature TEM images during the growth of Ge NW. (a) Au nanoclusters in solid state at 500 °C, (b) alloying initiated at 800 °C, at this stage Au exists mostly in solid state, (c) liquid Au/Ge alloy, (d) the nucleation of Ge NW on the alloy surface, (e) Ge NW grows with further Ge condensation and eventually forms a wire (f)	9
2.4	Three film growth mode; (a) Frank-van der Merwe (b) Volmer-Weber and (c) Stranski-Krastanov	11
2.5	Schematic band alignment diagram of Si/Ge heterojunction by Anderson's rule	13
2.6	The conduction band valleys of Ge and Si in the Brillouin zone	15
2.7	Indirect energy band gap of coherently strained bulk $Si_{1-x}Ge_x$ alloys for growth on (100) Si substrates	16
2.8	Schematic energy band alignment diagram of S-K Si/SiGe cluster	17
2.9	(a) HRTEM image of a portion of Si NW and (b) SEM image of a Ge NW	18
2.10	(a) TEM image of a amorphous Si NW [12] and (b) SEM image of Ge nanorods	19
2.11	TEM image of Si NWs containing twin crystals. (a) A short Si NW and (b) Si NW with a kink. In (b), the insets are the enlarged Si crystal image at position 1, 2, and 3. The white lines corresponds to (111) planes. Si lattice at 1 is twin to that at 2, which is twin to that at position 3	21
2.12	(a) SAED pattern of a single Si NW and (b) XRD spectrum of Si NW arrays	23
2.13	Raman spectra of (a) ① bulk Ge and Ge NWs with diameters of ② 36-83 nm and ③ 12-28 nm and (b) Si NWs	25

Figure **Page**

2.14 Low-temperature PL from Si crystal containing 2×10^{14} cm^{-3} phosphorus atoms. At the top of each peak, no-phonon transition (NP) and phonon-participating transition (TA and TO) are specified. 100 μ, 300 μ, 450 μ and 1000 μ indicate spectral resolution gain (slit width) 26

2.15 (a) PL spectra of Si NWs and (b) ball-milled Si nanocrystals. In (a), oxidation conditions are ① 900 °C, 30 min; ② 700 °C, 15 min; ③ 700 °C, 10 min and ④ 700 °C, 5 min 27

2.16 SEM image of three terminal Si single NW device, with the source (S), gate (G), and drain (D) labeled 28

2.17 Three terminal transport measurement of Si NW device with Al contacts without annealing (a) and after annealing at 550 °C (b). (c) *I-V* characteristics of Si NW with Ti/Au contacts, before (solid line) and after (dashed line) annealing at 750 °C for 1 h 29

2.18 (a) *I-V* curves of Ge NWs at different temperatures and (b) Linear resistance dependence on the temperature, where diamonds are experimental data and the solid line is the fitting curve according to the thermal fluctuation-induced model 30

2.19 TEM images of (a) SiGe dome cluster and (b) a pyramid cluster formed on (100) Si and (c) AFM image of the surface of Ge clusters on (100) Si showing the co-existence of pyramidal- and dome-shaped clusters 32

2.20 TEM cross section images of cluster SL grown by (a) MBE (Si/ $Si_{0.54}Ge_{0.46}$ SL grown at 650 °C) and (b) CVD ($Si/Si_{0.4}Ge_{0.6}$ SL grown at 525 °C) 33

2.21 PL spectra of SiGe clusters SL with ten layers of SiGe clusters under different excitation power levels measured at 4.5 K. The TO and NP PL lines originating from the first WL and the upper WL are indicated by TO_{WL1}, NP_{WL1}, TO_{WL}, and NP_{WL}, respectively. The PL band from the clusters could be deconvoluted into two Gaussian line-shaped peaks which are indicated by TO_{ID} and NP_{ID}, respectively 35

3.1 SEM image of Ge NWs (a) on (100) n^+ Si substrate and (b) on (111) p^+ Si substrate 40

LIST OF FIGURES
(Continued)

Figure **Page**

3.2 (a) Raman spectrum of the Ge NWs with an estimated NW length of 360 nm grown on a (111) p^+ Si substrate and (b) Low temperature PL spectra of c-Si, Ge NWs grown on (100) $n^+$and (111) p^+ Si substrates 42

3.3 TEM images of MBE-grown Si/SiGe cluster SL samples: (a) sample 1813 and (b) sample 1831 45

3.4 Schematic representations of the samples with contacts: (a) Wood's alloy contact and (b) graphite contact configuration on Ge NWs/Si substrate samples and (c) Wood's alloy contact configuration on Si/SiGe cluster SL sample 47

3.5 Apparatus setup for electrical measurements 49

3.6 A schematic illustration of *I-V* mapping points 51

3.7 Apparatus setup for optical measurements 52

4.1 *I-V* data for samples of (a) 1400 nm Ge NWs on (100) n^+ Si substrate, (b) 710 nm Ge NWs on (100) n^+ Si substrate and (c) 1400 nm Ge NWs on (111) p^+ Si substrate with graphite contacts. *I-V* data measured using a graphite tip touching Si substrate surface outside of the Ge NW area are also plotted (dashed lines) 55

4.2 Conductance curves of (a) 1400 nm Ge NWs on (111) p^+ Si substrate, (b) 710 nm Ge NWs on (111) p^+ Si substrate and (c) 1400 nm Ge NWs on (100) n^+ Si substrate as a function of frequency (All the samples with graphite tip contacts) 58

4.3 Conductance curves of 1400 nm Ge NWs on (100) n^+ Si substrate with metal contact as a function of (a) bias voltage and (b) frequency 61

4.4 (a) *I-V* characteristics of Ge NWs grown on (111) oriented Si substrate at several temperatures under dark and illumination. The near ohmic dark *I-V* characteristics are shown for (b) reverse bias (positive voltage applied on Si substrate and negative on Ge NWs) voltage and (c) forward bias voltage 63

4.5 *I-V* characteristics in samples of Ge NWs grown on (100) oriented, n^+ Si substrate at three different temperatures (a) T=280 K, (b) T=180 K, and (c) T=110 K 64

LIST OF FIGURES
(Continued)

Figure **Page**

4.6 Photocurrent and dark current temperature dependences in Ge NW/n^+ Si samples at bias V=-0.5 V. Photocurrent is determined by subtracting dark current, and the calculated activation energies are shown. The inset shows a photocurrent transient under slow-chopped laser with clearly observed photocurrent oscillations during the "light-on" time interval 65

4.7 Photocurrent as a function of voltage at different (indicated) temperatures in Ge NW/n^+ Si samples showing clearly observed negative differential photoconductivity. 66

4.8 The proposed energy band alignment for (a) Ge NW/p^+ Si and (b) Ge NW/n^+ Si heterojunctions 68

4.9 (a) I-V curves measured at a local point under dark and different intensity illumination showing typical diode-like characteristics and (b) their differential conductance curves. The sign of the voltage is shown for the bias applied to the Si substrate. Note the different scales (linear or logarithmic) at vertical axes. 74

4.10 (a) I-V curves measured at a local point under dark and different intensity illumination showing step-like features and (b) their differential conductance curves 76

4.11 Schematic energy band diagram of the sample structure when the tip is placed between the SiGe clusters vertical stacks for different bias conditions: (a) without bias, (b) forward bias and (c) reverse bias 78

4.12 Schematic energy band diagram of the sample structure (without bias) when the tip is placed on the SiGe clusters vertical stacks 80

4.13 Schematic diagram showing variation of conduction energy band in Si/SiGe cluster SL as sample negative bias increases. Dashed lines indicate the heterointerfaces. Conduction band offset at the Si/SiGe interfaces is ignored 82

4.14 Low temperature (T=8 K) normalized PL spectra measured at different excitation intensities. SiGe cluster PL at 0.1 W/cm^2 excitation is fitted with two Gaussian curves (dashed lines). Note vertical logarithmic scale 83

4.15 Peak positions and FWHM of the two fitting curves with increasing PL excitation intensity 85

LIST OF FIGURES
(Continued)

Figure **Page**

4.16 PL spectra measured between T=8 and 210 K at 5 W/cm^2 laser excitation. The spectra are shown on a logarithmic scale and vertically shifted for clarity 86

4.17 SiGe cluster integrated PL intensity temperature dependence for various excitation intensities and fitting curves with two (indicated) thermal quenching activation energies. Dashed lines are extension of the fitting curves beyond the fitted data range. Note logarithmic scale along vertical and horizontal axes 88

4.18 Temperature dependence of SiGe cluster integrated PL intensity measured from samples with (a) 20 nm and (b) 7.5 nm thick Si separating layers at different excitation intensities. The dash lines show fittings using two thermal quenching activation energies. The values of E_2 are shown 89

4.19 The integrated PL intensity in the samples with 20 nm thick Si separating layers measured during the heating/cooling cycles under an excitation intensity of 5 W/cm^2 90

4.20 Low Low temperature (T=30 K) EL spectra at different sample bias 94

4.21 Normalized EL spectra originating from SiGe clusters at different sample bias. Solid lines are fitting curves which are deconvoluted into two symmetric Gaussian curves (dashed lines) 95

4.22 Integrated EL intensity as a function of the pulsed voltage amplitude measured at indicated temperatures 95

4.23 Sample current and (b) EL intensity as a function of the reciprocal temperatures at V=-5 V. The thermal activation energies form fits are also shown 96

4.24 Low temperature (T=15 K) PL spectra of sample 1831 measured at different excitation intensities 97

4.25 Low temperature (T=15 K) PL spectra measured at different excitation intensities using Nd:YAG Q-switched pulse laser 98

4.26 Low temperature (T=15 K) PL spectra measured in Si-related spectral region at different excitation intensity using Nd:YAG Q-switched pulse laser 99

LIST OF FIGURES
(Continued)

Figure **Page**

4.27 PL dynamics under different (indicated) pulsed laser energy densities recorded at photon energies associated with SiGe PL (~0.873 eV) and Si EHD PL (~1.079 eV). Note vertical logarithmic scale 101

4.28 PL peak intensities as functions of reciprocal temperature measured at different (indicated) excitation energy densities 102

4.29 Schematic representation of different recombination processes in Si/SiGe 3D nanostructures with a type II energy band alignment at Si/SiGe heterointerface (a) at low excess carrier concentration, (b) at high excess carrier concentration and (c) During ~0.1-1 μs after the laser pulse 104

CHAPTER 1

INTRODUCTION

For the last decade, SiGe has become the vital part of the CMOS technology, mainly due to the successful development of heterojunction bipolar transistor (HBT) technology for Bi-CMOS and RF applications [1]. However, the fabrication of Si/SiGe heterostructures with an abrupt Si/Ge heterointerface is restricted on the Ge (SiGe) layer thickness and the material composition because of a stress appearing at the heterointerface due to considerable lattice mismatch (~4 %) between bulk Si and Ge. Hence, most of the studies on Si/Ge heterostructure systems have been concentrated on thin strained layer pseudomorphic heterostructures formed with Si and SiGe alloy, until new fabrication techniques of low-dimensional self-assembled nanostructures were discovered. Among other approaches, two novel nano-systems are considered in this dissertation, quasi-one-dimensional (quasi-1D) Si/Ge hetero-junctions and three-dimensional (i.e. cluster-like) morphology Si/SiGe multilayers superlattices (SLs).

More specifically, this study focuses on electrical and optical properties of micron-long Ge nanowires (NW)/Si substrate hetero-systems and Si/SiGe clusters nanostructures where efficient structural relaxation might be allowed due to high surface-to-volume ratio of Ge NWs and 3D morphology of SiGe clusters. These systems are expected to play an important role in both, interconnects (e.g., passive) and functional (e.g., active) components in nanoscale electronics and optoelectronics.

In the extreme case (e.g. a few-nanometer dimension), the electronic band structures of these systems might change significantly due to carrier confinement in more

than one direction. The effect of quantum confinement plays a crucial role transforming indirect band gap semiconductors such as Si and Ge into quasi-direct band gap materials, where optoelectronic applications are no longer limited by an inefficient, phonon-assisted carrier recombination [2]. Also, the excitonic Bohr radius (R_B) in bulk Ge is 24.3 nm compared to Si with $R_B = 4.9$ nm, resulting in a more prominent quantum size effect [2, 3, 4].

The overall objective of this research is focused on carrier transport and optical properties (mainly photo- and electroluminescence) of Ge NWs/Si substrate heterostructures produced by a method named vapor-liquid-solid (VLS) growth and Si/SiGe clusters superlattices (SLs) fabricated by Stranski-Krastanov (S-K) growth.

Chapter 2 presents an extensive review considering details of the growth processes; structural, optical and electrical characterization methods; and physical properties of SiGe nanostructures using recently published data. The following original part of this dissertation (chapter 3 and 4) starts with descriptions on the preparations of the samples by chemical vapor deposition (CVD) or molecular beam epitaxy (MBE). Previously investigated (by Dr. Tsybeskov's group) optical properties of the Ge NW samples are also summarized in this chapter. The experimental set up and measurement procedures are described in the later part of chapter 3.

Chapter 4 is devoted to detailed presentation of the experimental results and extensive discussions. As for the NWs samples, electrical measurements including room temperature DC and AC data and current-voltage *(I-V)* temperature dependences are presented and discussed. The results show that these electrical measurements correlate with the optical measurements previously published by Dr. Tsybeskov's group [5], and

support the conclusion that Ge NWs/Si substrate interface could be modeled using an abrupt and defect-free Ge NW/Si substrate heterointerface. In the following section of chapter 4, the electrical and optical measurements on Si/SiGe clusters SLs are discussed, including analysis of the observed temporal and spectral photoluminescence (PL) at different excitation conditions and nano-scale mapping of current-voltage characteristics using a variable temperature scanning-tunneling-microscope (STM). The observed results are consistently explained using the discussed model based on type-II energy band alignment at Si/SiGe clusters heterointerface, where most of the energy band discontinuity is in valence energy band.

In chapter 5, this dissertation ends with summary of the presented work and concluding remarks.

CHAPTER 2

BACKGROUND

2.1 Vapor-Liquid-Solid and Other Mechanisms of Nanowire Growth

A critical issue in the study and application of NWs is how to assemble individual atoms into such a unique one-dimensional (1D) nanostructure in an effective and controllable way. A general requirement for any successful preparative methodology is to be able to achieve nanometer scale control in NW diameter during anisotropic crystal growth while maintaining a good overall crystallinity.

During the past decade, many methodologies have been developed to synthesize 1D nanostructures. Generally, they can be categorized into two major approaches based on the reaction media which were used during the preparation: solution and gas phase based processes. More detailed description includes several major techniques as the following:

(a) Template-directed synthesis represents a convenient and versatile method for generating 1D nanostructures. In this technique, the template simply serves as a scaffold against which other kinds of materials with similar morphologies are synthesized. These templates could be nanoscale channels within mesoporous materials or porous alumina and polycarbonate membranes, etc. The produced NWs can then be released from the templates by selectively removing the host matrix.

(b) Solution-liquid-solid (SLS) method has been used to obtain highly crystalline semiconductor NWs at low temperatures, e.g., for the growth of InP, InAs, and GaAs nanowhiskers. This approach uses simple, low-temperature (less than or equal to 203 °C), solution phase reactions. The materials are produced as near-single-crystal whiskers having widths of 10 to 150 nanometers and lengths up to several micrometers.

(c) Lately, solvothermal methodology has been extensively examined as one possible route to produce semiconductor NWs and nanorods. In these processes, a solvent was mixed with certain metal precursors and, possibly, a crystal growth regulating

or templating agent such as amines. This solution mixture was then placed in an autoclave kept at relatively high temperature and pressure to carry out the crystal growth and assembly process. This methodology seems to be quite versatile and has been demonstrated to be able to produce many different crystalline semiconductor nanorods and NWs.

(d) A well-accepted mechanism of NW growth via gas phase reaction is the so-called vapor-liquid-solid (VLS) process proposed by Wagner in 1960s during his studies of single-crystalline whisker growth [6, 7]. According to this mechanism, the anisotropic crystal growth is promoted by the presence of liquid alloy/solid interface. This process is illustrated in Fig. 2.1 for the growth of Ge NW using Au clusters as catalyst at high temperature.

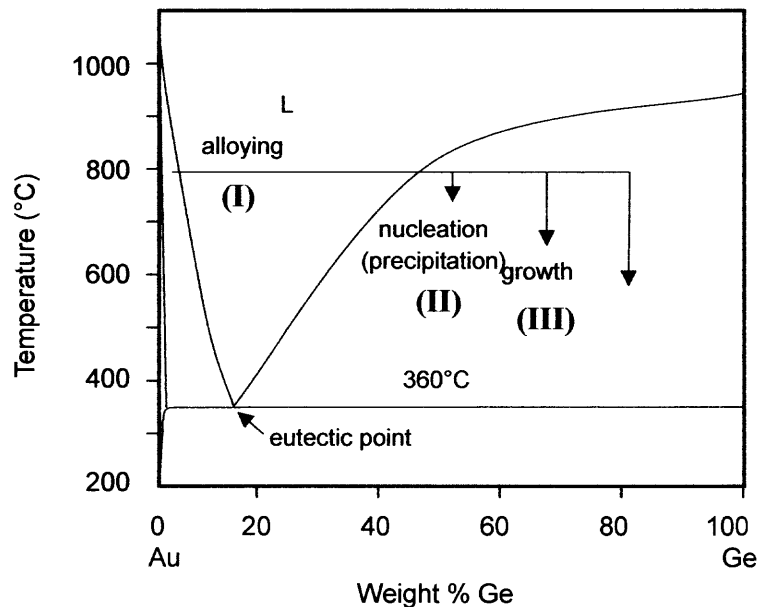

Figure 2.1 Au-Ge phase diagram showing three states along the isothermal line; (I) alloying, (II) nucleation and (III) axial growth [6].

In VLS, a metal particle is used as a catalytic nucleation site during the growth of semiconductor NWs. Various metals, such as Au, Fe, Ti, and Ga, catalytically enhance the growth of NWs. A phase diagram of these metal-semiconductor alloys determines the eutectic temperature, and the growth temperature is set in between the eutectic point and

the melting point of the materials. However, the growth temperature can be lower than the eutectic temperature reported on the binary phase diagram; the equilibrium melting point of solid decreases with decrease in the size of its particle (Gibbs-Thomson effect) [8, 9]. The Gibbs-Thomson effect relates surface curvature to vapor pressure and chemical potential. It leads to the fact that small liquid droplets (i.e. particles with a high surface curvature) exhibit a higher effective vapor pressure, since the surface is larger in comparison to the volume.

For Au-Ge system, eutectic temperatures as low as ~360 °C (Fig. 2.1) enable low temperature synthesis of Ge NWs, which is likely to give possible future advantage of easy incorporation with existing semiconductor electronic devices. It has already been shown that Au-Ge chemical vapor deposition by Au-catalyzed decomposition of GeH_4 source gas is possible even below the eutectic temperature, 360 °C [10]. At a given temperature, NWs grow passing three states as shown in Fig. 2.1 by the arrowed line from left to right through the phase diagram. The decomposition reaction can be expressed as below.

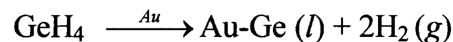

$$GeH_4 \xrightarrow{Au} \text{Au-Ge}\ (l) + 2H_2\ (g)$$

The mechanism of VLS growth mode for Au-catalyzed Ge NWs begins with a formation of an eutectic alloy between Au particle and Ge. Au particles are usually prepared by evaporating Au film onto Si wafer, which acts as catalytic sites for NWs growth. The catalytic reaction forms a very thin, Ge-rich layer on the surface of the Au-Ge alloy particle at the growing end of the wire. The excess Ge near the surface results in a concentration gradient that causes the excess Ge to diffuse into the Au-Ge island. The

excess Ge is likely to precipitate (nucleate) usually at the alloy/solid interface.

According to Kamins et al. [11], this process can be explained with respect to energy conservation law as the following. In order to form macroscopic quantities of Ge on the free surface of the Au-Ge alloy, an additional interface must be formed, probably increasing the energy of the system. On the other hand, if the excess Ge diffuses to the underlying Au-Ge and Ge interface; it can attach to Ge there without requiring an additional interface to form, and the energy of the system does not need to increase. As the Ge atoms precipitate on the underlying Ge, the Ge-Au island is pushed up, forming a wire. Transport of excess Ge from the alloy surface is accommodated by bulk diffusion through the alloy particle or surface diffusion around it on its surface, and Ge could reach the growing NW along the interface between the alloy particle and the NW. Figure 2.2 is the schematic representation of Ge NW growth mechanism.

The supersaturation and following precipitation on the growth interface depends on the NW diameter. The Gibbs-Thomson effect places a lower limit on the diameter of structures for thermal growth [12]. As the diameter of NW becomes smaller, the vapor pressure (or chemical potential) of Ge on tip of NW increases and thereby supersaturation decreases due to the reduced vapor pressure difference (i.e., thermodynamic driving force for supersaturation) at the interface between outer source gas and Au-Ge alloy droplet. Therefore, the growth rate of NWs is lower for smaller diameter and a critical diameter is found below which the growth stops completely. However, the lower limit for the wire diameter decreases for increasing gas pressure, i.e., higher pressure increase the NW growth rate. An increased source gas pressure appears to enhance the catalytic growth process.

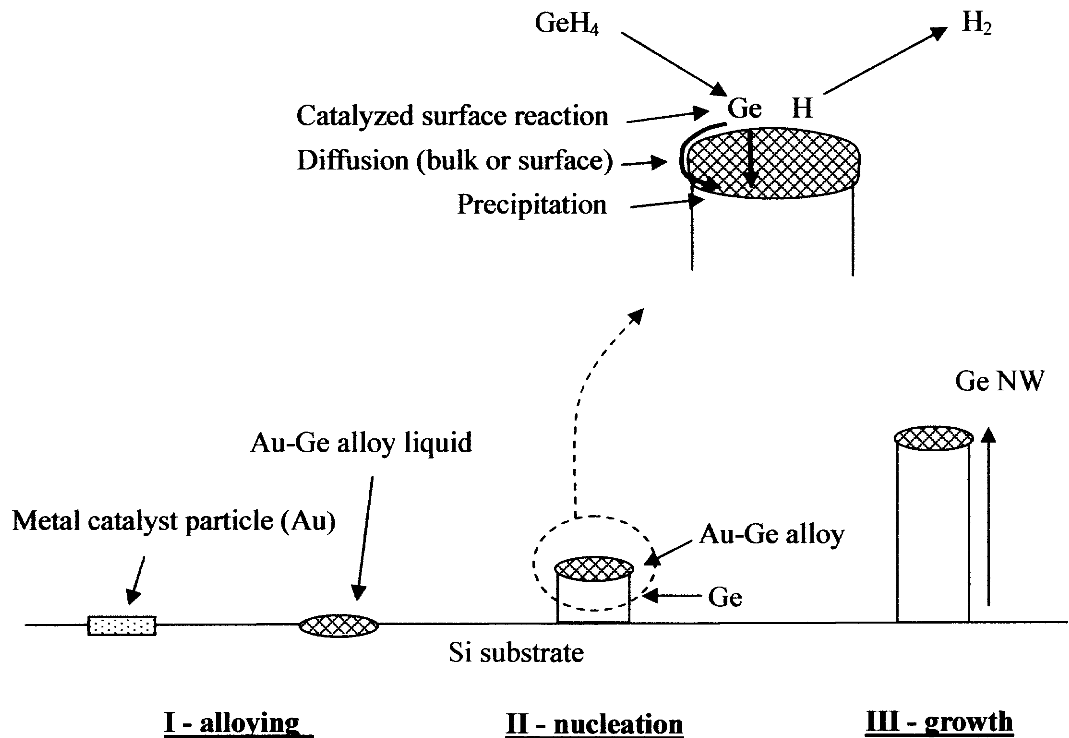

Figure 2.2 Schematic representation of NW growth mechanism.

To allow wire growth, transport of Ge away from the surface must not be the slowest process. If neither bulk nor surface diffusion is adequately rapid, the Ge decomposing on the surface covers the catalyst particle. The incoming gas is then shielded from the particle so that the particle cannot continue catalyzing the decomposition, the growth rate then slows to the normal Ge growth rate on Ge, the surrounding Ge grows at the same rate as that of the Ge above the nanoparticle, and no wires form. As metal-containing liquid nanoparticles move along with the tip of the wire, Ge NWs grow.

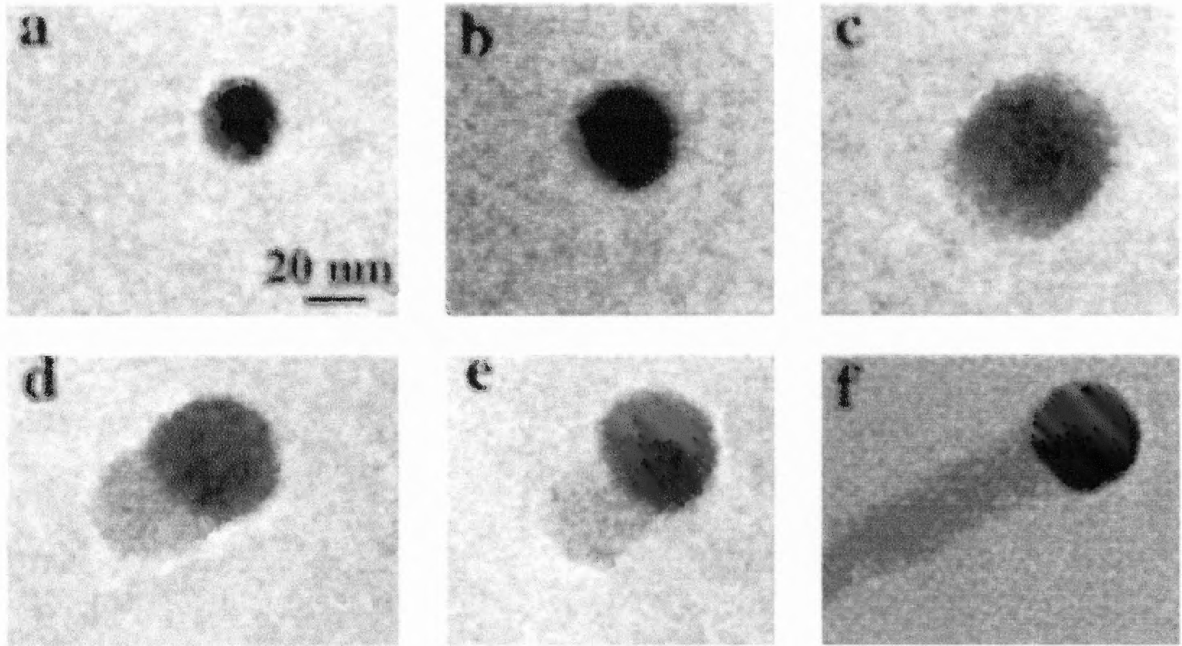

Figure 2.3 In situ high temperature TEM images during the growth of Ge NW. (a) Au nanoclusters in solid state at 500 °C, (b) alloying initiated at 800 °C, at this stage Au exists mostly in solid state, (c) liquid Au/Ge alloy, (d) the nucleation of Ge NW on the alloy surface, (e) Ge NW grows with further Ge condensation and eventually forms a wire (f) [13].

Figure 2.3 shows the real time sequential pictures of Ge NWs synthesis taken by in situ high temperature TEM performed by Wu et al. [13], which corroborate interpretation of NWs synthesis by VLS mechanism. Three stages mentioned before, (I) alloying, (II) nucleation and (III) axial growth, are well matched with the pictures (a) to (c), (d), and (e) to (f), respectively. Before Ge vapor is introduced, Au particles remain in solid state. Wu et al. observed that Au particles kept their state up to 900 °C. With increasing amount of Ge vapor on the surface of Au particle, Ge condenses, diffuses and forms an alloy with Au particle and then liquefies as the Ge fraction increases in the alloy. In Fig. 2.3a to c, the tendency of increase in size of the alloy droplet and decrease in elemental contrast indicate that, while the alloy composition changes with the increase of Ge fraction, the droplet undergoes the transition from a bi-phase region of solid Au and

Au-Ge liquid alloy to a single phase region of Au-Ge liquid alloy. With further concentration of Ge in the Au-Ge alloy droplet, the precipitation of Ge after diffusion to the interface between the liquid alloy and the solid lead to the beginning of NW nucleation (Fig. 2.3d). After the Ge nanocrystal nucleates, further transport of the Ge vapor into the system increases the amount of Ge precipitation from the alloy (Fig. 2.3e). The interface is then pushed up to form NWs (Fig. 2.3f).

2.2 Stranski-Krastanov Growth Mechanism of Si/SiGe Nanostructure

In heteroepitaxy, there are three possible growth modes, which are illustrated schematically in Fig. 2.4 [14]. The first, Frank-van der Merwe, is simply the successive addition of 2D layers to the lattice-matching substrate crystal. The second mode, Volmer-Weber, will occur if the added material can minimize its free energy by trading increased surface area for decreased interfacial area, forming an island structure like water droplets on glass. This happens when atoms or molecules in the deposit are more strongly bound to each other than to the substrate. A third possibility, an intermediate combination of the above mentioned modes, can arise if the lattice spacing of the added material mismatches the crystalline substrate. Here, growth starts with a strained 2D wetting layer (WL), but clusters form after the first few monolayers. The explanation of the driving force for 2D-3D conversion is still discussed, being controversial or incomplete, but the prevailing one is based on energetic considerations. During the growth, the strain energy accumulates in the growing film. At some point, when (i) it is energetically favorable for the film to relax by forming 3D clusters rather than by forming misfit dislocations and (ii) the strain energy relieved by forming clusters exceeds the additional surface energy resulting from

clustering, 3D clusters start forming on 2D WL. This third mode of growth is called Stranski-Krastanov (S-K).

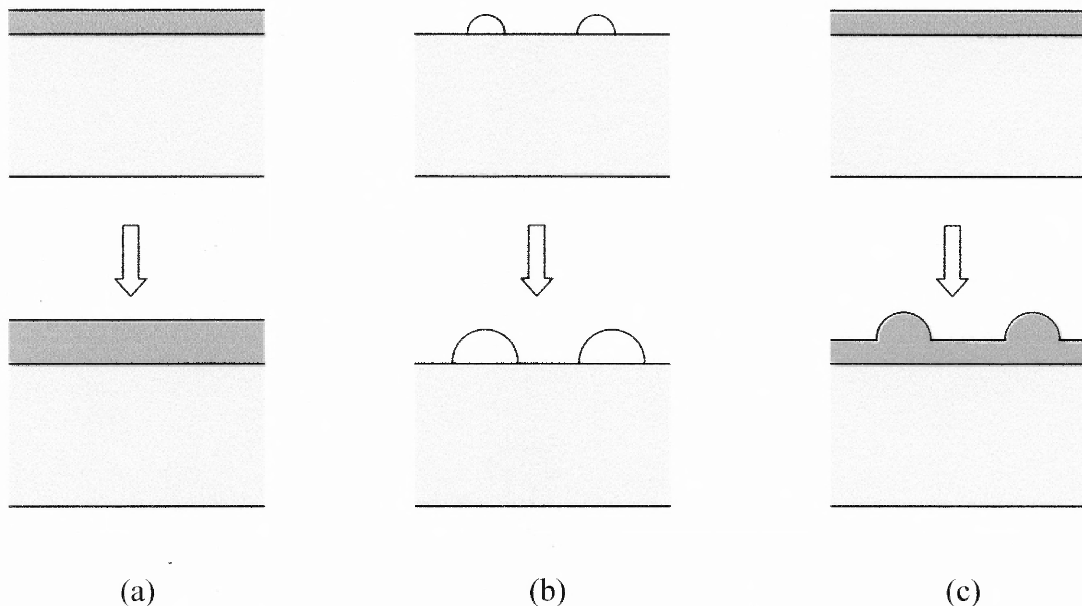

Figure 2.4 Three film growth mode; (a) Frank-van der Merwe (b) Volmer-Weber and (c) Stranski-Krastanov.

Out of the three basic growth modes of hetero-epitaxial films, the S-K growth mode is a common method applied for fabrication of high-quality semiconductor 3D nanostructures, compatible with Si technology. During growth of SiGe on Si, at temperatures of typically 600-700°C, clusters form without any misfit dislocations after the first 3-6 monolayers form a WL, i.e., 3D clusters of SiGe grow coherently on the substrate [15, 16]. The cluster properties such as composition, size, shape and spatial distributions are varied by the parameters of the deposition process. Moreover, in actual structures, the size and shape of individual clusters grown together in a structure are

nonidentical, which is a major drawback of S-K grown clusters. One of the possibilities to reduce the inhomogeneity of self-assembled SiGe clusters is the fabrication of multilayer stacks of clusters, where each cluster layer is separated from the previous one by a separating layer. In this structure, if the separating layer thickness is kept within a critical thickness, the strain fields of underlying clusters penetrate into the separating layer and induce stacks of vertically aligned and laterally more homogeneous clusters in upper layers [17, 18]. More details will be provided in the later section 2.4.2.

2.3 Si/Ge Heterojunction Band Discontinuities

Band discontinuity at the interface of a semiconductor heterojunction is one of crucial parameters which determine electrical carrier transport property, and it has been a central problem of Si/SiGe lattice-mismatched heterostructures.

In an ideal case, the conduction band discontinuity ΔE_C would be the difference in electron affinities $q(\chi_2 - \chi_1)$, and the valence band discontinuity ΔE_V would be found from $\Delta E_g - \Delta E_C$, which is known as the Anderson's affinity rule [19]. Since bulk Si and Ge have almost the same electron affinities ($\chi_{Ge} = 4.00$ eV, $\chi_{Si} = 4.05$ eV), the ideal band alignment would be like the one in Fig. 2.5. However, this approach is appropriate only under an assumption that the electron affinity of bulk material is a unique and absolute energy reference which is not affected by its surface properties, especially by the interface structures [20, 21].

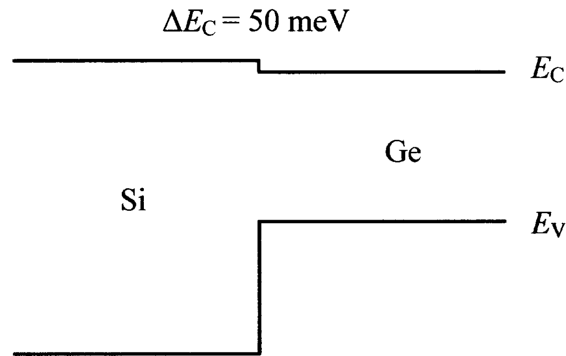

Figure 2.5 Schematic band alignment diagram of Si/Ge heterojunction by Anderson's rule.

The lattice constants of the pure elements Si and Ge are mismatched by 4.2 %, a_{Ge}=5.66 Å and a_{Si}=5.43 Å on (001) surface, and it has been impossible to fabricate abrupt Ge/Si heterojunctions without misfit defect generation [22]. The lattice mismatch, however, can also be accommodated by lattice strain. Earlier measurements and theoretical calculations confirmed that the energy band lineups at the Si/Ge interfaces are dependent on the interface properties, and also upon the strain conditions in the materials [20, 23, 24, 25, 26].

The experimental energy band gap variations of tetragonal-strained $Si_{1-x}Ge_x$ layer are well described by theoretical calculations using deformation potential theory [27, 28]. In addition, the expected valence band offsets for a strained $Si_{1-x}Ge_x$ layer grown on (001) $Si_{1-y}Ge_y$ virtual substrate (unstrained) has been calculated in a good agreement with experimental results [29, 30]: $\Delta E_{\mathrm{VB,av}} = (x-y)\cdot(0.47-0.06y)$ eV, where $\Delta E_{\mathrm{VB,av}}$ is weighted averaged potential of strain-split HH and LH bands.

According to the study by F. Schaffler [1], there are general features of the $Si_{1-x}Ge_x/Si_{1-y}Ge_y$ heterojunction band alignment. (i) The valence band maximum always occurs in the higher Ge content layer. (ii) For $x < y$ the energy band alignment is always of type-II regardless of x and y. (iii) In the case when $x > y$ for most compositions practically a flat conduction energy band is expected with the band offset smaller than ±20 meV. In fact, historically, there have been controversies on the type of the energy band alignment of SiGe alloy layer grown on Si substrate, where the conduction band alignment is expected to be practically flat with calculated band offset ΔE_{VB} smaller than several tens meV for a wide range of Ge content [1]. Hence, the accepted energy band offsets and alignment for such cases are usually based on a consensus derived from the result of a number of different measurement techniques. Nevertheless, in case when strained SiGe layers with Ge composition less than 30% are set between unstrained Si layers, the energy band alignment is accepted as type-I [31].

The understanding of the energy band edge modification in pseudomorphic 2D SiGe alloy under strain condition provides qualitative insight into the estimation of the energy band alignments in lower dimensional Si/Ge heterojunction systems such as NWs and clusters. Both Si and Ge are indirect band gap and have similar valence band structures but conduction band structures are completely different in k-space. Si has the six conduction band minima [Δ(6)] about 0.85 of the way along the Γ and X points toward [100] direction and Ge has the conduction band minima at the L points (toward [111] directions) with eight equivalent half valleys or four equivalent full valleys of the Brillouin zone (Fig. 2.6). In unstrained $Si_{1-x}Ge_x$ alloys, the conduction band is Si-like

with Δ(6) between the Γ and X points of the Brillouin zone up to a Ge content of x=0.85. For x>0.85, the alloy is Ge-like with conduction band minima at L point (Fig. 2.7) [28].

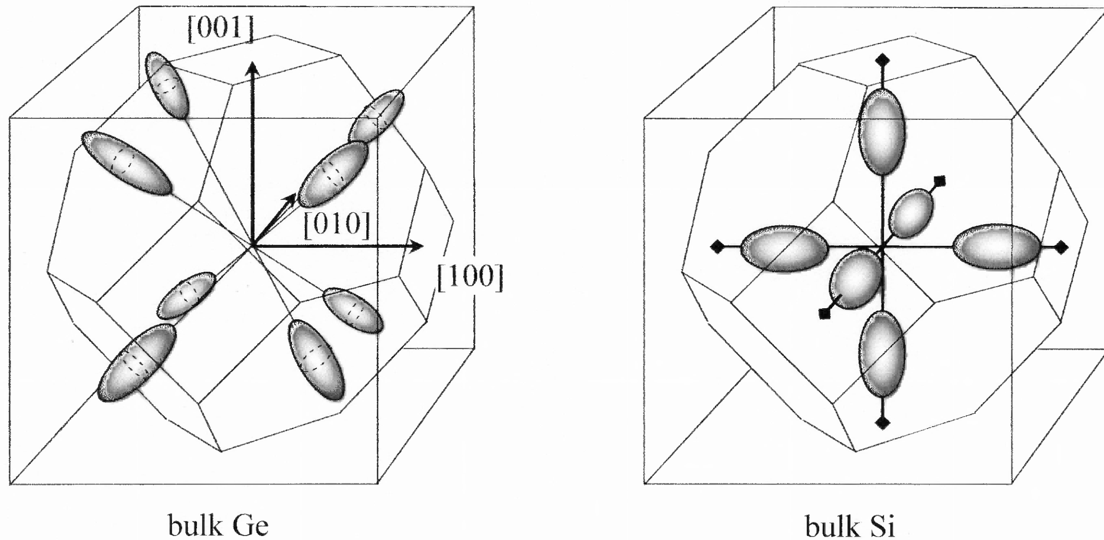

Figure 2.6 The conduction band valleys of Ge and Si in the Brillouin zone.

The energy band gap of SiGe alloy is strongly affected by strain. Epitaxially grown SiGe alloy layers on (100) Si substrate are subject to in-plain compressive strain and the strain can be fully described with two components, a hydrostatic and a uniaxial strain along [100] growth direction, which cause shifting and degeneracy splitting of energy band edges, respectively. Since the average energy band is unaffected by the uniaxial strain, the split Δ(2) and Δ(4) bands shift in opposite directions with the Δ(2) level moving by twice the amount of the Δ(4) band. As also shown in Fig. 2.7, taking the strain effect into account, the lowest conduction band of the strained SiGe layer is Si-like (i.e., conduction band minimum is formed at Δ) for whole range of x. More generally, for pseudomorphic $Si_{1-x}Ge_x$ layer grown on (100) unstrained $Si_{1-y}Ge_y$ substrate, the

fundamental band gap is formed between Δ(2) (in the [100] direction) and light hole (LH) for tensilely strained $Si_{1-x}Ge_x$ and Δ(4) (within the layer plane) and heavy hole (HH) for compressively strained $Si_{1-x}Ge_x$.

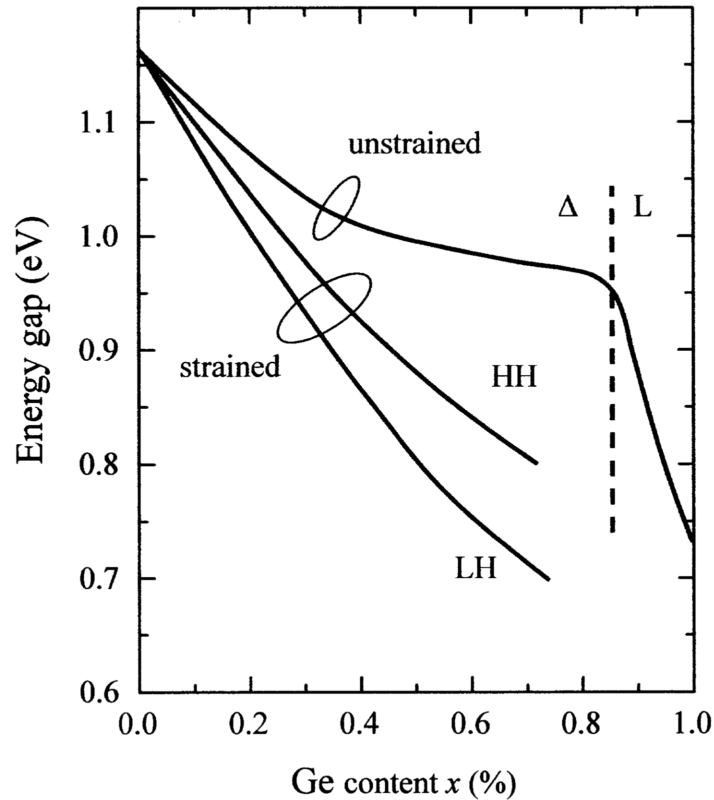

Figure 2.7 Indirect energy band gap of coherently strained bulk $Si_{1-x}Ge_x$ alloys for growth on (100) Si substrates [28].

A qualitative approach using the above-mentioned deformation-potential theory can be made for energy band alignment expectation of S-K SiGe clusters embedded into Si matrix. Since the growth mode is strain-induced and the cluster formation is a result of elastic relaxation, Si above and below the elastically relaxed SiGe clusters exhibit tensile strain. As has been mentioned previously, in tensile strained Si, the two fold degenerate Δ(2) valleys of the conduction band is downshifted. For S-K Si/SiGe cluster nanostructures, it has been shown that this splitting energy is significant compared to that

in the 2D structures [32]. This result in a clear type-II band alignment with significant offset in both bands at the interface between the SiGe clusters and the surrounding Si (Fig. 2.8) [33, 34]. As an another approach, the energy band alignment of S-K SiGe in this condition can be thought of as being analogous to the case where Si layer is grown on a SiGe substrate, which is type-II.

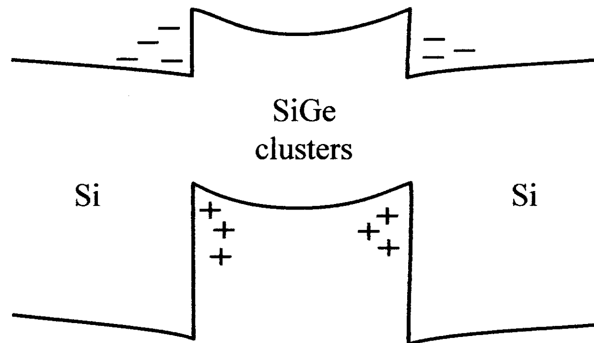

Figure 2.8 Schematic energy band alignment diagram of S-K Si/SiGe clusters.

In a 1D NW system, because of a small NW diameter, the stress from the mismatch can relax without creating defects at the interface. That is, the efficient strain relaxation occurs through the open side surface in the NW geometry. This may introduce an additional benefit, which is the advantageous condition for combining highly mismatched materials such as pure Si and Ge. However, to the best of knowledge, there has been no experimental or theoretical report on the band lineups of Ge NW grown on Si substrate.

2.4 Characterizations and Properties of Low-dimensional Nanostructures

2.4.1 Properties of Nanowires

Mostly, structural characterizations of NWs are performed by a combination of scanning electron microscopy (SEM), transmission electron microscopy (TEM), X-ray diffraction (XRD) and electron diffraction (ED). While TEM and SEM provide actual image of structure, XRD and ED helps quantitative analysis of it. Through structural characterization, it is also possible to investigate the growth mechanism.

Figure 2.9 (a) and (b) show a high resolution transmission electron microscopy (HRTEM) image of a Si NW and a SEM image of a Ge NW grown by VLS, respectively. Straight NWs show high crystallinity. It is also seen that the outer layer of Si NW is surrounded with native amorphous SiO_2; an oxide layer is characteristic of Si NWs and Ge NWs.

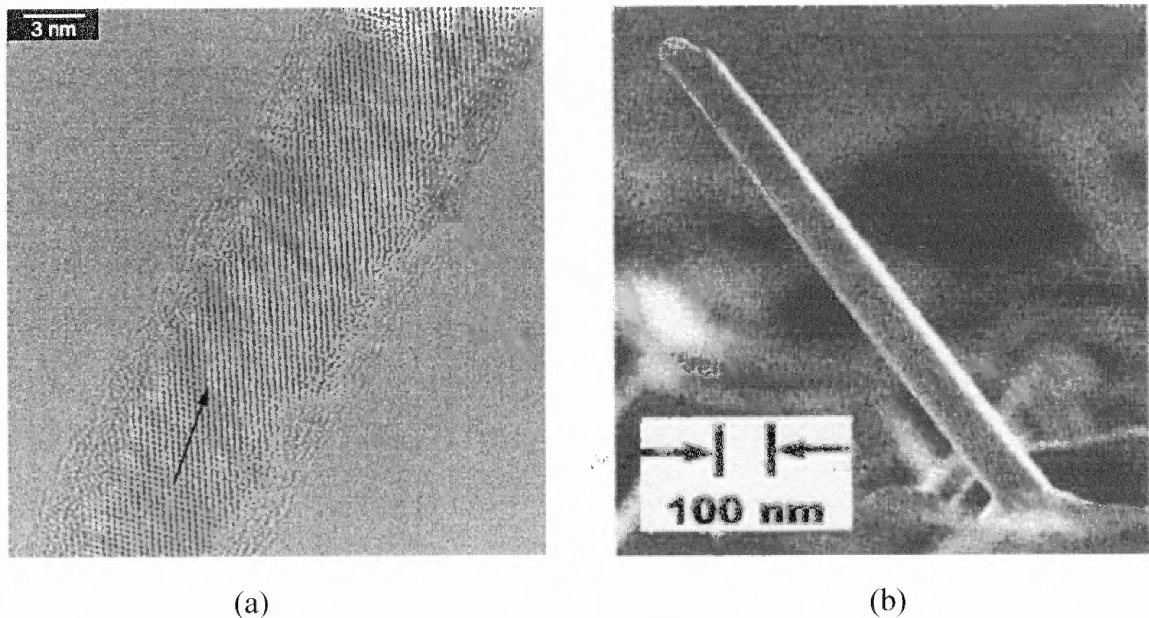

(a) (b)

Figure 2.9 (a) HRTEM image of a portion of Si NW [12] and (b) SEM image of a Ge NW [35].

Sometimes, amorphous worm-like NWs or 3D nanorods structure are formed at different growth conditions. When source gas decomposition and diffusive transport of it through or on the catalyst particle is very fast, then the transport supplies source material at a higher rate than the crystallization rate for a given diameter, resulting in amorphous NWs [12]. A TEM image of an Au-catalyzed Si NW grown by plasma enhanced CVD shows that increased growth rate, in radio-frequency plasma, causes amorphous growth (Fig. 2.10a). However, 3D nanorods can form instead of NW when the decomposition is faster than transport, as was already mentioned at section 2.1, or the diffused material can not effectively surmount chemical potential barrier at the liquid eutectic-solid interface (the energy barrier for nucleation and for growth of NWs). In VLS this barrier provides rate limiting step for NW solidification, e.g., due to a low source gas pressure (Fig. 2.10b) [36].

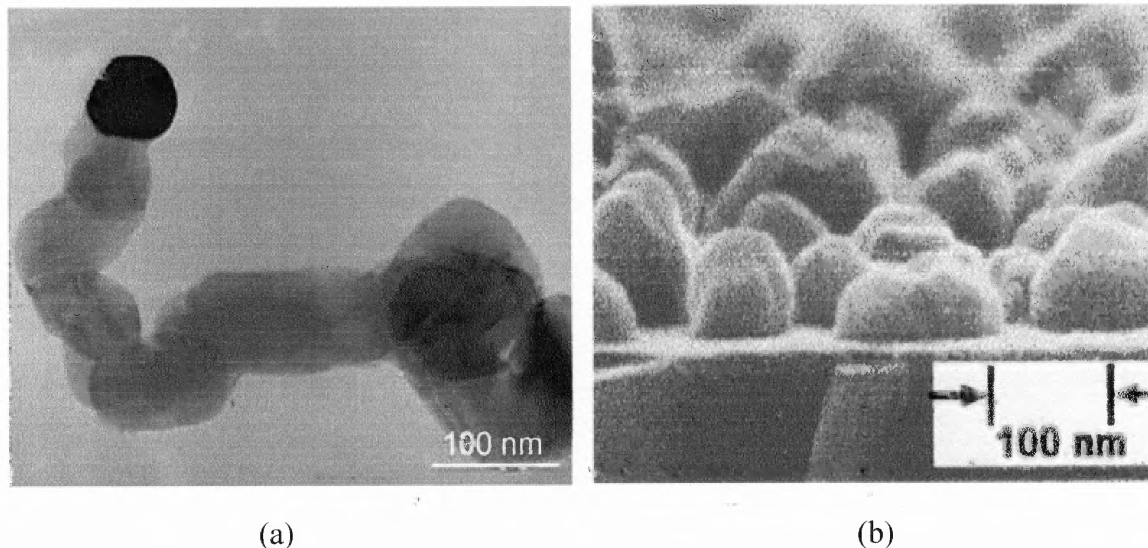

Figure 2.10 (a) TEM image of a amorphous Si NW [12] and (b) SEM image of Ge nanorods [36].

Defects in the highly crystalline NW are likely to create different crystal planes during growth, causing the shape of wire kinked [11, 35]. Kinks can be observed at sharp angles in NWs. These kinks are likely to be related to dislocation defect. Tang et al. [35] explained the origin of kinks by twin dislocation formation during the growth (Fig. 2.11a and b). In their theory, twin dislocation defect form due to lattice mismatch between catalyzing islands and NWs. Figure 2.11 (b) is TEM image of Si NW grown by molecular beam epitaxy using $TiSi_2$ catalyst and Si_2H_6 gas source. The growth process can be explained by VLS except for the situation where the catalyzing islands remain in solid state during the growth different from VLS situation wherein they are in the liquid state, reducing the stress at the island-Si interface. The strain from the lattice mismatch of ~6 % between Si NW and $TiSi_2$ island forms a twin crystal during the growth, which dominates the growth direction resulting in formation of kinks.

Figure 2.11 (a) shows a Si NW growing toward the right-hand side, in which a twin crystal is starting to develop at its lower edge and a highly defected Si crystal containing stacking faults is being formed at the upper edge. At initial stage, the lattice stress at the interface between $TiSi_2$ islands and Si causes the Shockley partial dislocation at the edge of $TiSi_2$ islands, where the stress is highest and the starting of dislocation is easiest, and then, it glides along Si {111} planes. As the partial dislocation glides through every parallel {111} plane, a twin crystal forms; otherwise, a highly defective crystal full of stacking faults forms. After the twin is formed, it grows along with the NW. When the twin is large enough to dominate the growth, the wire growth changes to a new direction dominated by the twin crystal, resulting in a kink. The twinning process can happen

several times during the NW growth. Therefore, the NW can change growth direction several times, resulting in many twinned regions in the NWs.

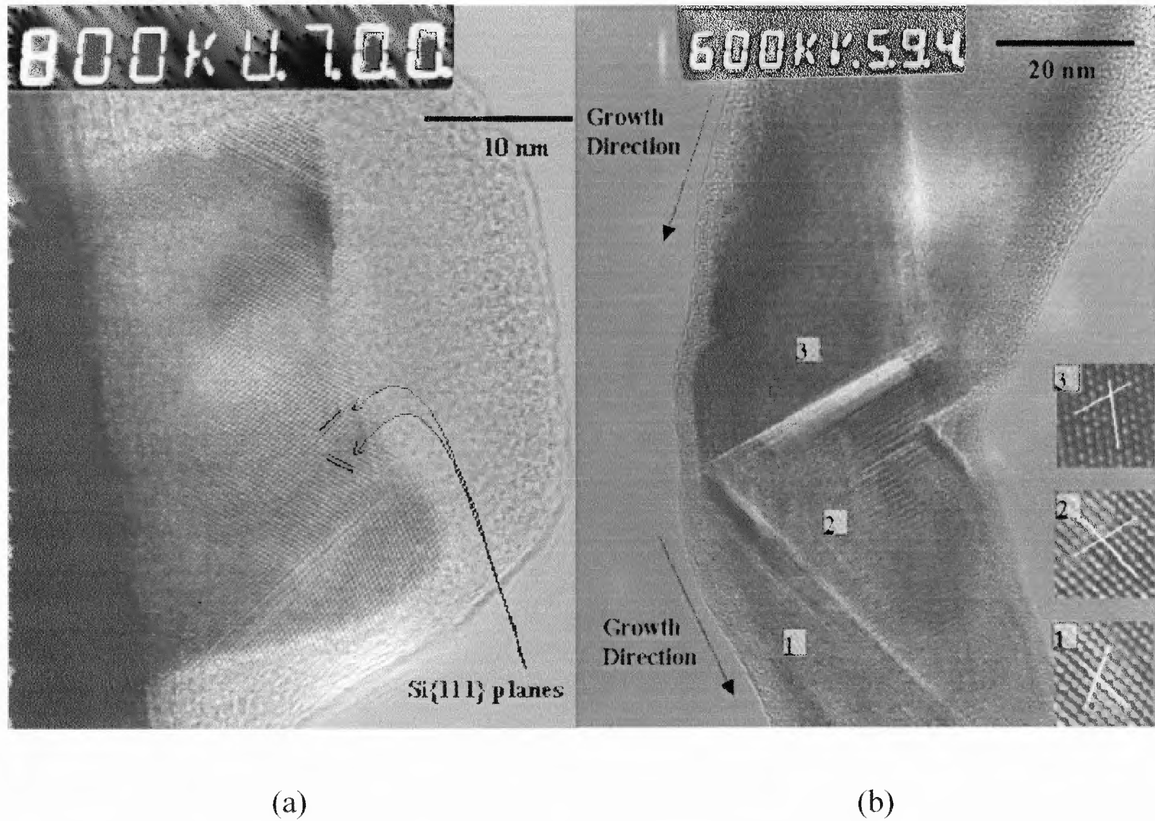

(a) (b)

Figure 2.11 TEM image of Si NWs containing twin crystals. (a) A short Si NW and (b) Si NW with a kink. In (b), the insets are the enlarged Si crystal image at position 1, 2, and 3. The white lines corresponds to (111) planes. Si lattice at 1 is twin to that at 2, which is twin to that at position 3 [35].

Compared to electron microscopy, X-ray and electron diffraction can give complementary quantitative information about the structure. Diffraction technique is the method that permits the direct identification of any crystalline material based on their unique crystal structure.

In X-ray diffraction (XRD) technique, the intensity of the diffracted X-rays is measured as a function of the diffraction angle, and the material's orientation. Electron diffraction (ED) technique enables the patterns to be directly observed on the viewing screen of the electron microscope since the diffracted electron beams have a high intensity and exposure times are in the order of a few seconds. Furthermore, diffraction patterns can be obtained from very small crystals selected with an aperture (Selected Area Electron Diffraction or SAED), and even from nm-sized regions by a focused electron beam (Convergent Beam Electron Diffraction or CBED).

Figure 2.12 shows SAED pattern and XRD spectrum of Si NWs arrays synthesized by CVD template method with an alumina template [37]. A single Si NW is taken for SAED. It can be seen that the diffraction spots are organized in a precise hexagon or parallelogram, indicating that the diamond lattice structure of bulk Si is preserved in the Si NWs. The pattern shows that the Si NW is a single crystal. From the XRD results, the arrays of Si NWs show a polycrystalline structure and the result conflicts with the SAED data above. Considering averaging nature of the XRD pattern and the diffraction pattern of different grains indicate different orientations, it can be proposed that the individual Si NW is essentially single crystal and Si NWs in an array have a different crystal orientation.

Raman scattering and photoluminescence (PL) measurements are usually done for optical characterization of NWs. Intensity and emission peaks in measured spectra give direct information about the material properties. Raman peaks of well-defined phonons in a single crystal semiconductor are very sharp. Raman spectroscopy is a suitable tool for

investigating the phonon confinement effect of nanomaterials. The peak position shift, broadening, and asymmetry of the Raman bands are characteristic of NWs [38, 39].

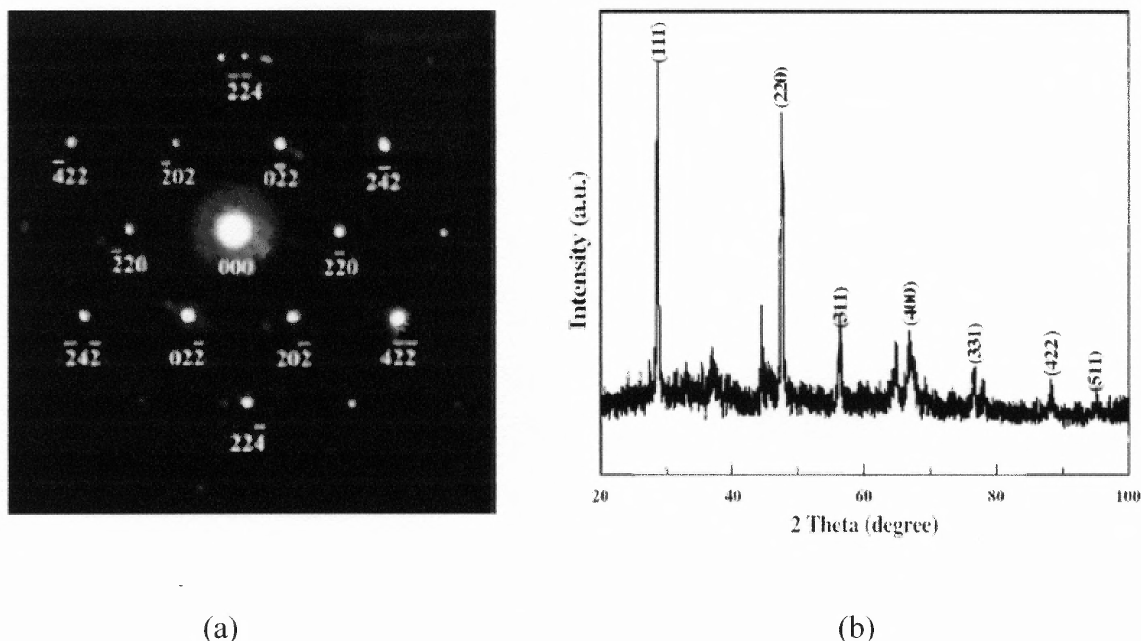

(a) (b)

Figure 2.12 (a) SAED pattern of a single Si NW and (b) XRD spectrum of Si NW arrays [37].

The small physical dimension of the crystalline NWs leads to a downshift and broadening of the first-order Raman line through a relaxation of size-dependent momentum vector selection rule [39, 40]. Because NWs are only two-dimensionally confined crystals, there is a momentum k=0 along their axis direction. Hence, the zone-center phonons allow for the Raman scattering to occur at the original peak position. However, in the direction perpendicular to the axis of NWs, nonzero k phonon dispersion may participate in Raman scattering and lead to both a peak broadening and an extension of the Raman peak towards low frequencies. Raman scattering is very sensitive to the lattice structure and crystal symmetry of microcrystalline materials. When the core

diameter of a NW is small, the Raman peak width increases and becomes more asymmetric with an extended tail at low frequencies.

Figure 2.13 (a) shows Raman spectra of bulk Ge and Ge NWs measured by Zhang et al [40]. The first-order Raman peak in bulk Ge at 298.5 cm^{-1} is symmetric with a full width at half maximum (FWHM) of 7 cm^{-1}. Raman scattering from the Ge NW sample with diameters of 36~83 nm shows a peak at 298.5 cm^{-1} that is slightly broadened (a FWHM of 10 cm^{-1}) and asymmetric. Raman peak of Ge NWs with diameters ranging from 12 to 28 nm is peaked at 293 cm^{-1}, asymmetric with a FWHM of 21 cm^{-1} and has an extended tail at low frequencies.

Figure 2.13 (b) shows Raman spectrum of Si NWs on Si substrates prepared by Lu et al [37]. The peak located at ~513 cm^{-1} is originated from the scattering of the first order transverse optical phonon mode (TO) of Si, which corresponds to the TO mode peak of Si, 520 cm^{-1} [39]. The full width at half maximum (FWHM) of the TO mode is broadened to ~18 cm^{-1} from the typical value 3~5 cm^{-1} of bulk Si [41]. They ascribed the downshift and larger FWHM to the quantum confinement effect caused by the small diameters, unique shapes and high surface-to-volume ratio of Si NWs. In addition, there are two broad peaks at ~286 cm^{-1} and 920 cm^{-1}, which are due to the scattering of the second order transverse acoustic phonon mode (2TA) and the second order optical phonon mode (2TO), respectively. It is also found that the two broad peaks are down-shifted from the value ~300 cm^{-1} and 970 cm^{-1} and their relative intensities increase as compared with those of 2TA and 2TO mode of Si. These properties are typical of crystalline Si NWs.

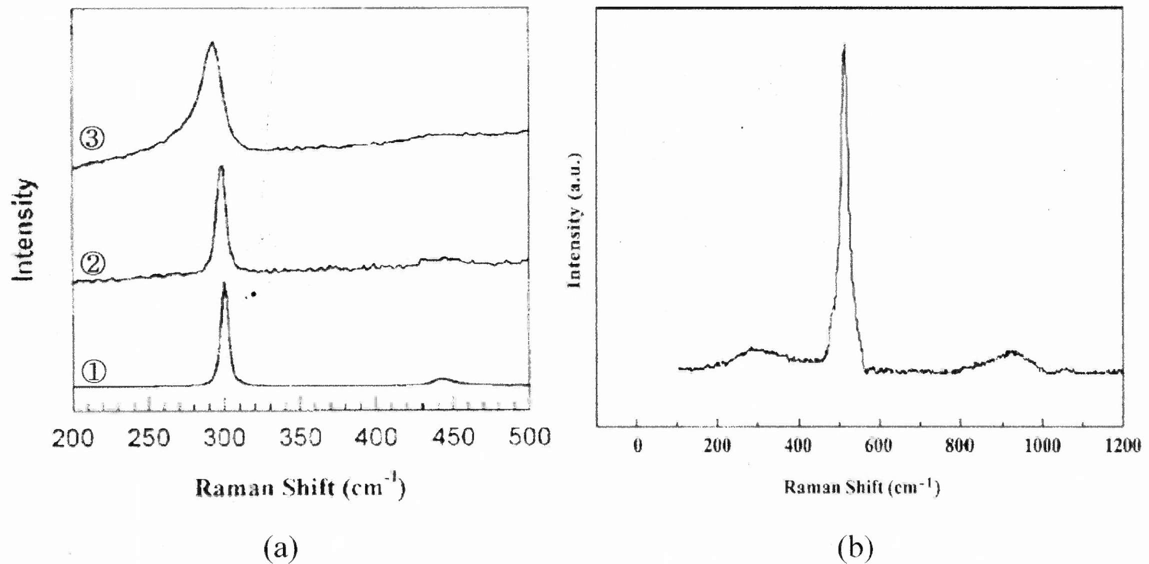

Figure 2.13 Raman spectra of (a) ① bulk Ge and Ge NWs with diameters of ② 36-83 nm and ③ 12-28 nm [40] and (b) Si NWs [37].

A typical low-temperature PL spectrum from a Si crystal containing low concentration of phosphorus atoms is shown in Fig. 2.14, which consists of the bound-exciton no-phonon (NP) transition and their phonon replicas, TA and TO, at lower photon energies [42]. Due to the indirect nature, the radiative recombination of electron-hole pairs in Si requires creation of a phonon with a certain k value to conserve momentum. On the other hand, in doped Si, it is possible for the bound electron-hole pair to recombine without phonon participation because impurity itself transfers the momentum in NP transition. In general, the NP line is weak and even forbidden in intrinsic bulk silicon. The intensity ratio of the NP line to the phonon replicas depends strongly on the binding energy and the type of impurity and is different for materials. In Si, coupling to TO phonon is strongest followed by the coupling to TA phonons. In Ge, LA and LO phonon replicas are favored.

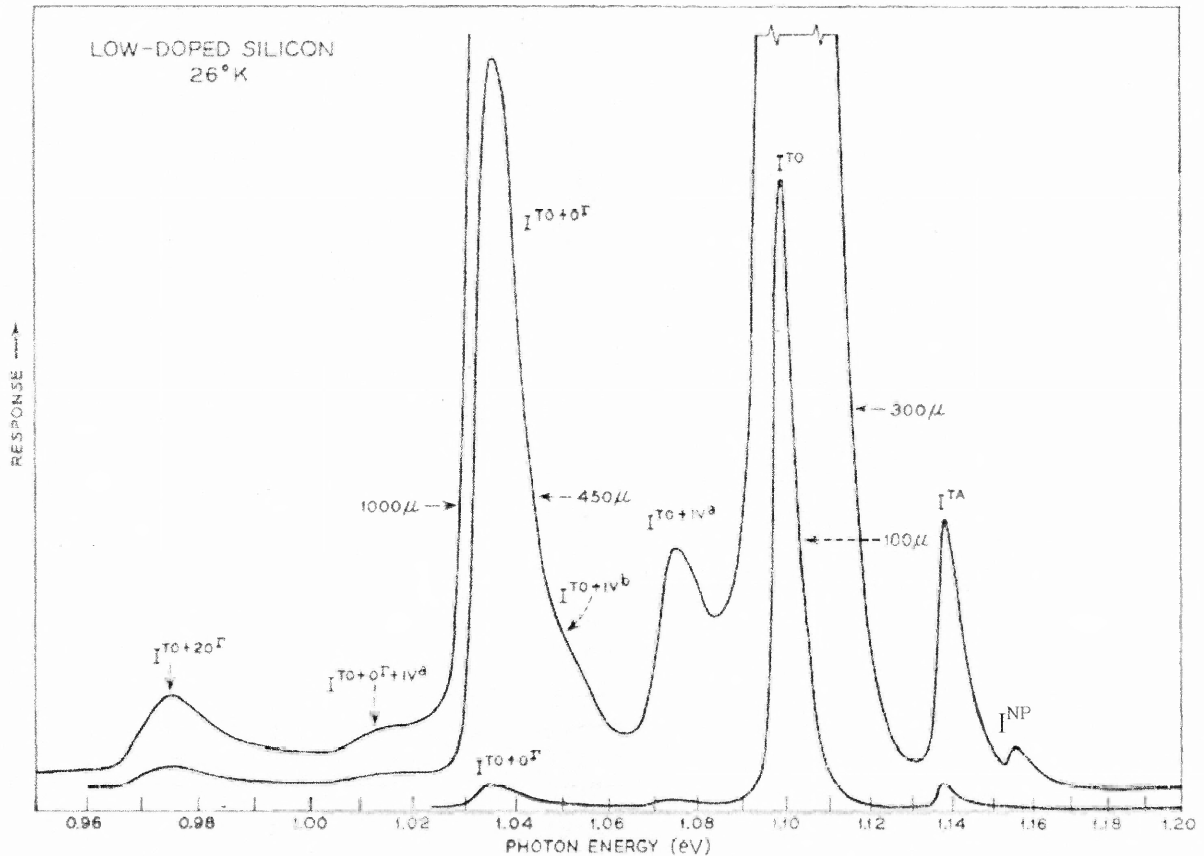

Figure 2.14 Low-temperature PL from Si crystal containing 2×10^{14} cm^{-3} phosphorus atoms [42]. At the top of each peak, no-phonon transition (NP) and phonon-participating transition (TA and TO) are specified. 100 μ, 300 μ, 450 μ and 1000 μ indicate spectral resolution gain (slit width).

The PL spectrum modification due to quantum confinement in an undoped Si has been reported besides those due to phonon assisted excitonic recombination characteristic for bulk indirect band gap Si (Fig. 2.15a) [43]. Bai et al. observed three emission bands in the red, green and blue regions from the oxidized Si NWs and found out that as the core size of Si NWs decreases with additional oxidation time, especially the red peak intensity increases much faster than the other two (Fig. 2.15). They proposed that the green and blue bands are attributed to recombination from the defects centers in oxidized layer and

the quantum confinement results in both the blue shift of the energy gap and a transition from the indirect towards the direct gap, which in turn dramatically increase the efficiency and intensity of red PL and cause the blue shift of red PL.

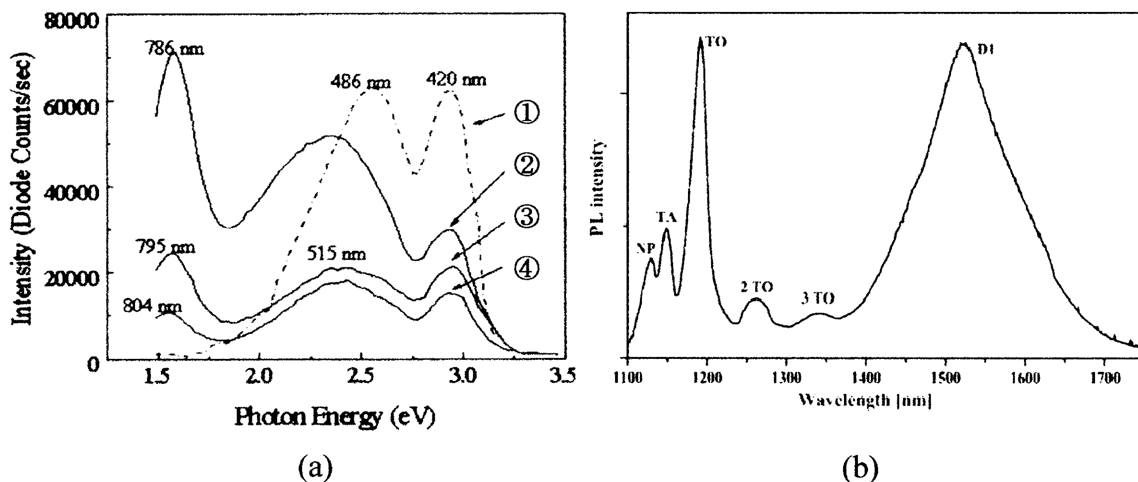

Figure 2.15 (a) PL spectra of Si NWs [43] and (b) ball-milled Si nanocrystals [44]. In (a), oxidation conditions are ① 900 °C, 30 min; ② 700 °C, 15 min; ③ 700 °C, 10 min and ④ 700 °C, 5 min

Figure 2.15 (b) is PL spectra of ball-milled Si nanocrystals (average diameter d = 100 nm) at T~4 K obtained by B.J. Pawlak [44]. D1 in Fig. 2.12b is a band related to dislocations in Si nanocrystal due to fabrication process. There were some indications of confinement effect in the investigated silicon nanocrystals. First, the ratio between NP transition and its replica is significantly different from the ratio usually found for bulk material. Second, they also found from their experiments that this excitonic lines up-shifted with diminishing grain diameter, leading to conclusion that these were associated with band structure perturbation due to size confinement.

Much useful information about NWs such as doping status and transport mechanism can be obtained by electrical characterization. However, little has been

reported regarding electrical characterization compared with structural and optical properties. To date, most of electrical characterizations are performed through the investigation of single NW.

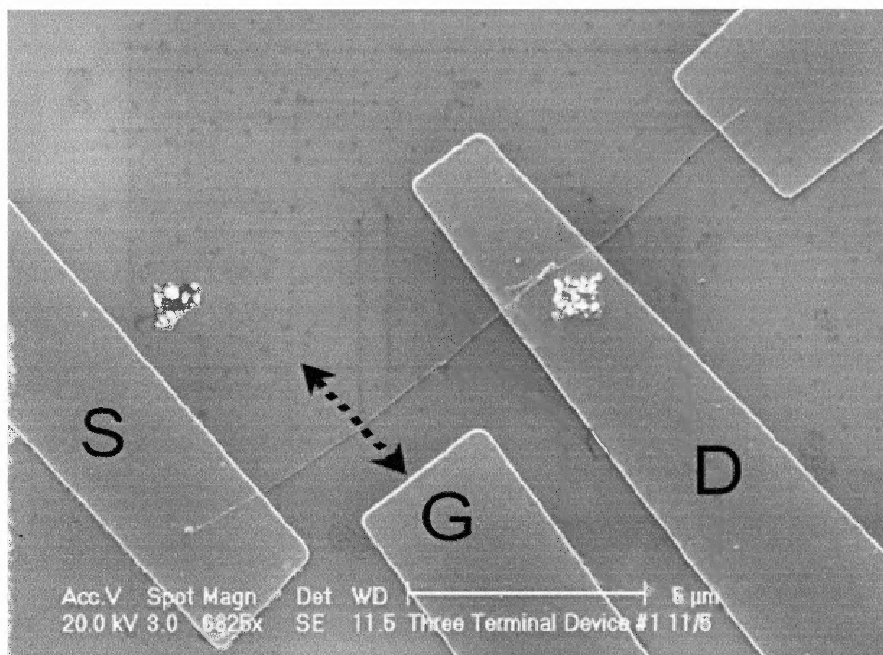

Figure 2.16 SEM image of three terminal Si single NW device, with the source (S), gate (G), and drain (D) labeled [45].

Figure 2.16 is an SEM image of a Si NW device produced via VLS growth with Au particles for the electrical measurement carried out by a group of Chung et al. [45]. A gate electrode is used to vary the electrostatic potential of a NW while measuring current versus voltage of the NW. The change in conductance from *I-V* curves of Si NW as a function of gate voltage can be used to distinguish whether a given NW is *p*-type or *n*-type since the conductance will vary oppositely for increasing positive and negative gate voltage.

They found out that the NWs were *p*-doped even before annealing and the comparison between the devices before and after thermal annealing (as indicated in Fig. 2.17a and b) led them to the conclusion that thermal treatment of the device resulted in better electrical contacts. The metallic-like *I-V* curves in Fig. 2.14c show no gate-voltage effect up to V_G=±40 V, indicates that diffusion of dopant atoms from Au contacts heavily doped the NWs during the thermal treatment; the diffusion coefficient of Au in Si at 750 °C is sufficient to heavily dope the entire wire with Au.

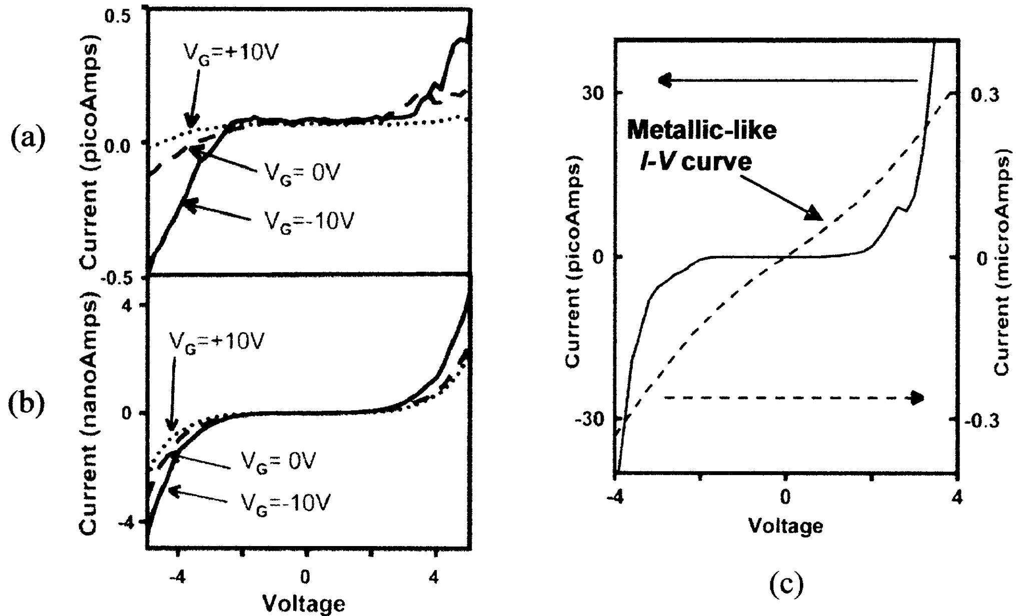

Figure 2.17 Three terminal transport measurement of Si NW device with Al contacts without annealing (a) and after annealing at 550 °C (b). (c) *I-V* characteristics of Si NW with Ti/Au contacts, before (solid line) and after (dashed line) annealing at 750 °C for 1 h [45].

Because nonlinear *I-V* curve indicates that metal/NW contact is characterized by a non-ohmic Schottky barrier, this measurement could not directly give the intrinsic

resistance of the NW without the knowledge of the contact resistance due to the metal/NW junction.

The first demonstration of intended and controlled doping of Si NWs and the characterization of the electrical properties of these doped NWs was achieved by Cui et al. [46]. They doped Si NW during the growth by incorporating dopants in the reactant flow and their estimates of the carrier mobility made from gate-dependent transport measurements were consistent with diffusive transport and showed an indication of reduced mobility in smaller diameter wires due to the enhanced scattering in the smaller diameter NWs.

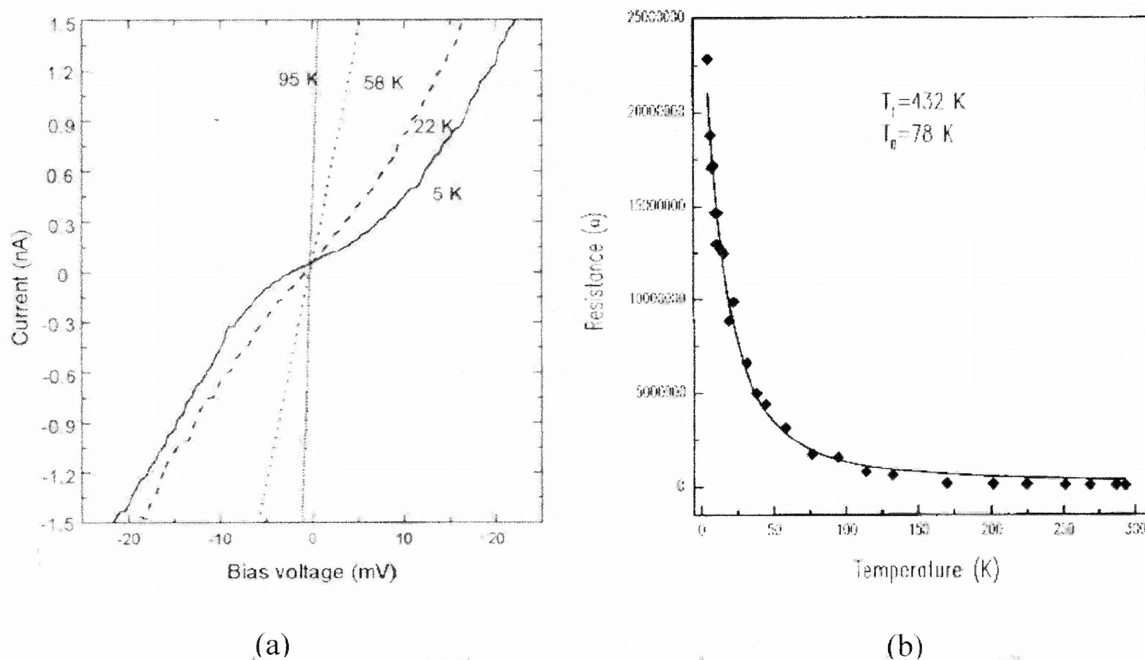

(a) (b)

Figure 2.18 (a) *I-V* curves of Ge NWs at different temperatures and (b) Linear resistance dependence on the temperature, where diamonds are experimental data and the solid line is the fitting curve according to the thermal fluctuation-induced model [3].

Temperature dependent scanning of resistance of individual NW also can be used for the study of transport mechanism. Figure 2.18 (a) and (b) are the *I-V* curves and

temperature dependent resistance curve measured on individual Ge NWs grown by Au-catalyst particle with Au contacts [3].

At temperatures higher than 100 K, linear current dependence on voltage indicates ohmic contacts between Ge NW and Au contacts. From the temperature dependence of the linear resistance at small bias voltage (Fig. 2.18b), Gu et al. found out that the resistance data could be fitted well with the fluctuation-induced tunneling model in heavily doped Ge NWs with Au atoms which could serve as both *p*-type and *n*-type dopants in Ge NWs.

2.4.2 Properties of S-K Si/SiGe Clusters

Si/SiGe nanostructures grown via S-K growth mode have been characterized mainly by structural and optical spectroscopy. The original reports on the structures SiGe clusters without dislocations on (100) Si were in the early 1990s [47, 48], and since then considerable work has been done with respect to their growth and structural investigation in the initial period, which now moved toward the study of their optical properties and applications. The optoelectronic properties of SiGe clusters strongly depend on their morphology, strain and compositional profiles, and accurate control of those is crucial for applications.

Figure 2.19 shows structures of SiGe clusters grown by molecular beam epitaxy (MBE) [49]. TEM and AFM allow the assessment of the cluster's size, shape, and distribution. During epitaxial growth, as Ge coverage increases, clusters initially form square or rectangular pyramid bounded by {105} facets, and then, further Ge coverage leads to formation of multi-faceted large dome clusters [50]. The shape transition is

suggested to be caused by the difference in the volume dependence of the energy of the surfaces, edges, and interfaces of the pyramids and domes. Depending on growth conditions, co-existence of pyramidal- and dome-shaped clusters is also observed as shown in Fig. 2.19c [50, 51].

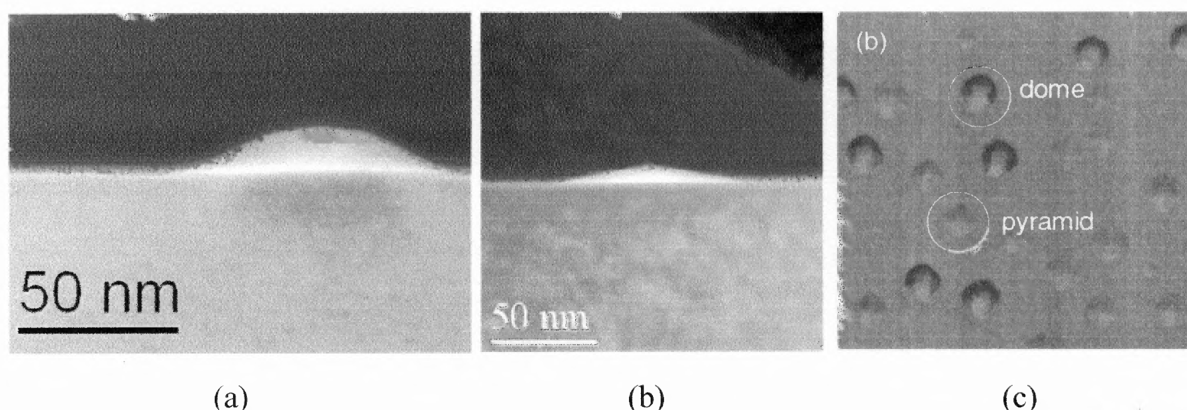

(a) (b) (c)

Figure 2.19 TEM images of (a) SiGe dome cluster and (b) a pyramid cluster formed on (100) Si and (c) AFM image of the surface of Ge clusters on (100) Si showing the co-existence of pyramidal- and dome-shaped clusters [49, 52].

Examples of MBE and CVD grown Si/SiGe clusters SL are shown in Fig. 2.20. Si/SiGe SL grown by MBE shows extremely regular stacks of SiGe clusters layers. In these structures, lattice mismatch between the two materials causes a lateral expansion in the Si surface above the SiGe clusters. This locally reduces the misfit to the following SiGe layer and causes the clusters of the next SiGe layer to be formed right above the buried clusters on the previous SiGe layer. The vertical alignments can be maintained within a critical separating layer thickness, which depends on the growth methods and conditions [52]. In many publications a WL thickness decrease accompanied by an additional cluster size increase in the upper layers due to these strain fields has been observed when the separating layers are thinner than a certain value [17, 18, 52]. Thus,

careful choice of separating layer thickness might be necessary within these two limitations for the fabrication of more regular stacks of clusters layers.

Different interface morphology is observed in cluster SL prepared by CVD as can be seen in Fig. 2.17b. Most likely due to the lower temperature used in CVD and conformal nature of the growth, although the structure exhibits waviness similar to MBE case, thickness variations is small and the separating layer is not observed to be planar [52].

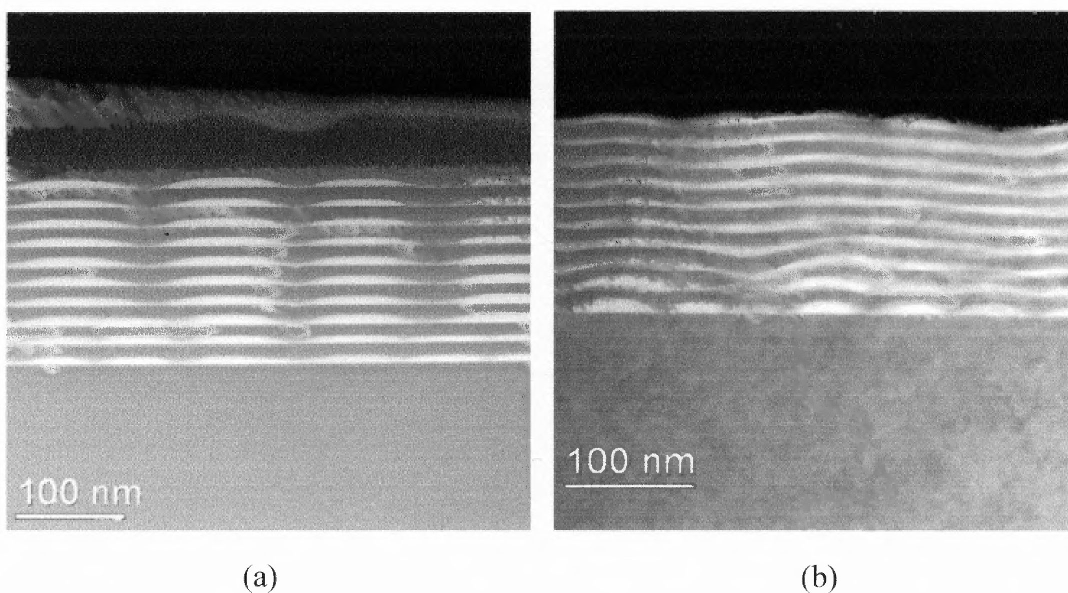

Figure 2.20 TEM cross section images of cluster SL grown by (a) MBE (Si/ $Si_{0.54}Ge_{0.46}$ SL grown at 650 °C) and (b) CVD ($Si/Si_{0.4}Ge_{0.6}$ SL grown at 525 °C) [52].

For the investigation of optical properties of SiGe clusters, PL technique is typically used. Both Si and Ge are indirect band gap materials and in optical transitions, phonons are required for momentum conservation. On the contrary, in SiGe alloys, direct optical transitions are observed due to the broken lattice symmetry [53]. Moreover, in

SiGe quantum structures such as quantum wells (QWs) and S-K SiGe clusters, the spatial confinement of the carriers spreads the wave functions in *k*-space and, thus, increases the probability of direct optical transitions [54, 55]. It has also been proposed and demonstrated that zone-folding effect creates a quasi direct gap in Si/Ge ultra thin layer superlattices [56, 57, 58].

Compared to SiGe planar QW structures, SiGe cluster structure makes it possible to access to much lower energy transitions of carriers. A planar pseudomorphic SiGe layer can only be grown up to a certain critical thickness, which limits the access to low energies for SiGe QW due to confinement shift. However, in S-K grown SiGe clusters, the height of SiGe clusters and higher composition of Ge reduce the energy transition gap. Other advantages over planar QW structures for optoelectronic device applications include enhancement of light emission and absorption due to three-dimensional spatial carrier localization [59]. The stronger spatial carrier localization causes more effective spread and overlap of hole and electron wave functions in *k*-space.

Figure 2.21 shows an example of PL spectra measured by Wan et al. with SiGe clusters SL grown by MBE [60]. Apart from the PL peaks of Si, the spectrum consists of two separate PL components, that are typical for SiGe WL and SiGe clusters, respectively. Two main peaks located at 1007 and 949 meV are attributed to the WL no-phonon (NP_{WL}) transition and its transverse-optical (TO_{WL}) assisted transitions.

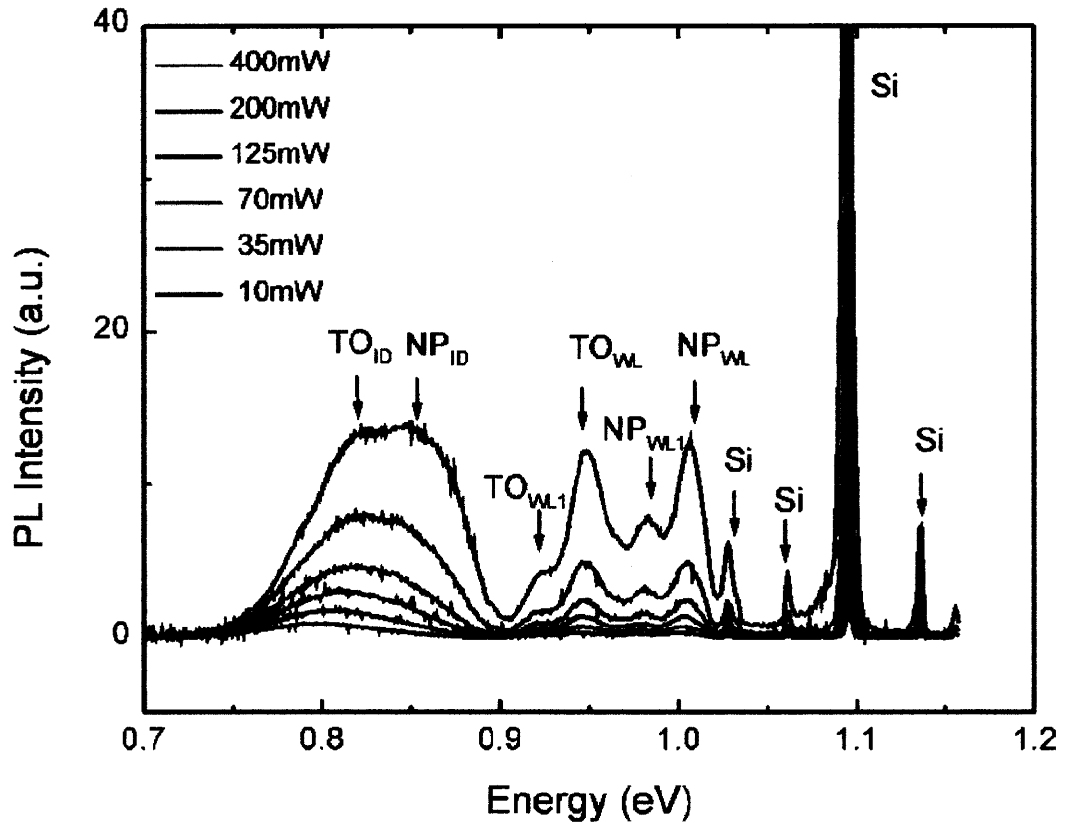

Figure 2.21 PL spectra of SiGe clusters SL with ten layers of SiGe clusters under different excitation power levels measured at 4.5 K. The TO and NP PL lines originating from the first WL and the upper WL are indicated by TO_{WL1}, NP_{WL1}, TO_{WL}, and NP_{WL}, respectively. The PL band from the clusters could be deconvoluted into two Gaussian line-shaped peaks which are indicated by TO_{ID} and NP_{ID}, respectively [60].

The energy difference between WL TO and NP lines is 58 meV, which corresponds to the Si-Si optical phonon energy in Si. The broad band in lower energy range is assigned to PL from SiGe clusters. The optical transitions in SiGe clusters are spatially indirect since the holes are confined in valence band of the clusters while electrons are localized outside of the clusters. The probability for this transition increases with the magnitude of the overlap of the electron/hole wave functions leaking into the potential barriers. The broad features in cluster related PL is attributed to inhomogeneous broadening of the energy levels of clusters system due to a non-uniform distribution of the size and shape of

individual clusters [61]. Additionally, the origin of these two peaks might be attributed to either a bimodal distribution of pyramid- and dome-shaped clusters or the NP transition and TO replica of the SiGe clusters [60].

There are also some studies by electrical methods such as capacitance-voltage, deep level transient spectroscopy and admittance spectroscopy focusing on the energy levels in Si/SiGe clusters structures [62, 63, 64]. Those studies revealed the discrete energy states due to confinement effect in the clusters as well as type-II heterostructure where holes and electrons are localized on different sides of the heterointerface. Electrons and holes in these states are spatially separated, and the transition between theses states is spatially indirect.

CHAPTER 3

EXPERIMENTAL

Ge NWs/Si substrate heterojunction samples for this study were grown via the VLS technique using low pressure chemical vapor deposition (LPCVD). The samples were prepared on (100) n^+ and (111) p^+ Si substrates and found to have different structural [10] and optical [5] properties, which will be described in the first section of this chapter. Si/SiGe clusters SL samples were also grown by CVD or MBE and the details on sample structures are dealt with in the following section.

Measurements on NWs were carried out by preparing contacts on the samples, and direct current-voltage (*I-V*) measurement at different sample temperatures and AC admittance spectroscopy were applied for the electrical characterization of Ge NWs/Si substrate heterojunctions.

For Si/SiGe clusters SL samples, which were grown by CVD or MBE with different structural parameters (i.e., different Si separating layer thicknesses or SiGe clusters sizes), electrical and optical measurements were performed. For the electrical measurements, a scanning-tunneling-microscope (STM) was used to investigate local carrier vertical transport in Si/SiGe clusters SL. Optical properties of the samples were studied using PL techniques. PL spectra were measured using a CW Ar^+ laser at different excitation intensity and temperatures. PL dynamics under Q-switched neodymium doped yttrium aluminum garnet (Nd:YAG) pulse laser excitation were also studied. Detailed measurement setup including apparatus arrangement, experimental procedure and specifications will be described in this chapter.

3.1 Samples and Contacts

The descriptions on the sample growth, known properties of Ge NW/Si substrate heterostructure samples in the following sections refer to the previous publications [5, 10]. The NW samples have been grown and structurally characterized using SEM/TEM by a research collaboration group in Hewlett-Packard Laboratories, California. Optical measurements using Raman scattering and PL have been conducted by Kamenev et al. at NJIT.

The Si/SiGe clusters SL samples have been grown using CVD in the above-mentioned group in Hewlett-Packard Laboratories or using MBE by another collaboration group in Institute for Microstructural Sciences, National Research Council, Canada.

3.1.1 Ge Nanowires/Si Substrate Samples

CVD by Au-catalyzed decomposition of GeH_4, has been used to grow Ge NWs on single crystal silicon. First, 20-nm-diamter nanoparticles as catalyst were deposited by dispersion of Au aqueous suspension onto cleaned (100) n^+ and (111) p^+ Si substrates and subsequent drying. The density of nanoparticles in aqueous suspension was 7×10^{11}/mL. The suspension contained less than 0.01 % of $HAuCl_4$. Substrate cleaning via 5% HF/H_2O was performed before the deposition of Au particles to remove surface oxide layer and obtain H-termination accompanied by minimal deionized water rinsing; it is known that the NWs direction loses preferential orientation during the growth due to the high growth rate and the oxide layer screening the substrate orientation [12].

After inserting the substrates into the lamp-heated CVD reactor, they were annealed at ~650 °C in H_2 at a pressure of 12.6 kPa for 10 min to remove surface contamination from the nanoparticles and to enhance contact to the Si substrates, which would contribute to the NWs adopting the orientation of the substrates during the growth. Then GeH_4 was introduced into the chamber after temperature was reduced to 320°C. The length of the grown Ge NWs increased approximately linearly with the deposition time. The typical diameter of the wires were 40 nm and the samples were prepared with different length of 360, 710, and 1400 nm, which depended on the deposition time 9, 18, and 36 minutes, respectively. Finally, the samples were cooled in H_2 and then N_2 to < 200 °C to minimize oxidation of the wire surface.

Figure 3.1 shows SEM image of the as-grown Ge NWs, where both the Ge NWs on (100) and (111) oriented Si wafers have the same <111> preferential growth direction, i.e., on (100) n^+ Si substrate, most of NWs grow at an angle of ~55° to the substrate (Figure 3.1 is a view in a <110> direction which is perpendicular to Si substrate normal), which corresponds to <111> direction, and on (111) p^+ Si substrate, they grow in the direction perpendicular to the substrate, in the same <111> direction. The preferential growth direction and structural investigation show that NWs are highly crystalline.

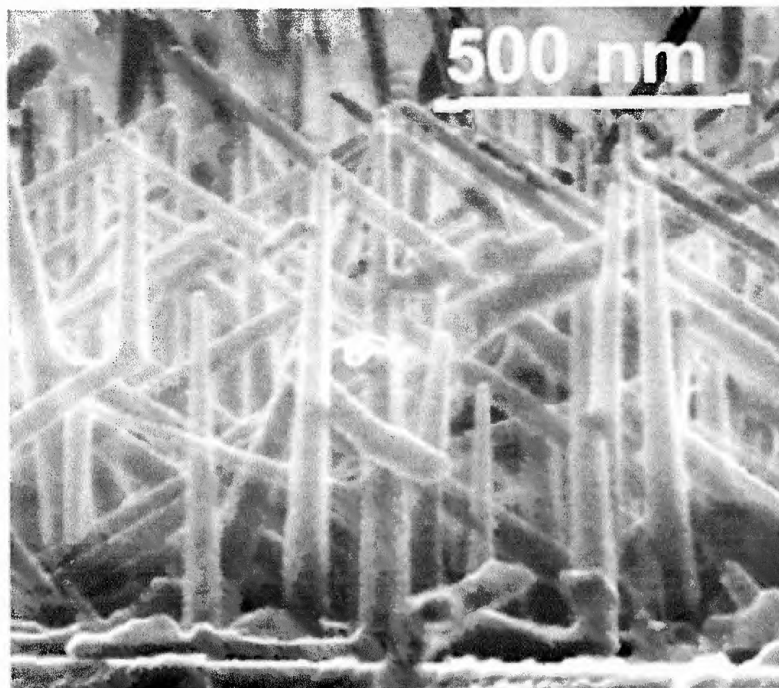

(a)

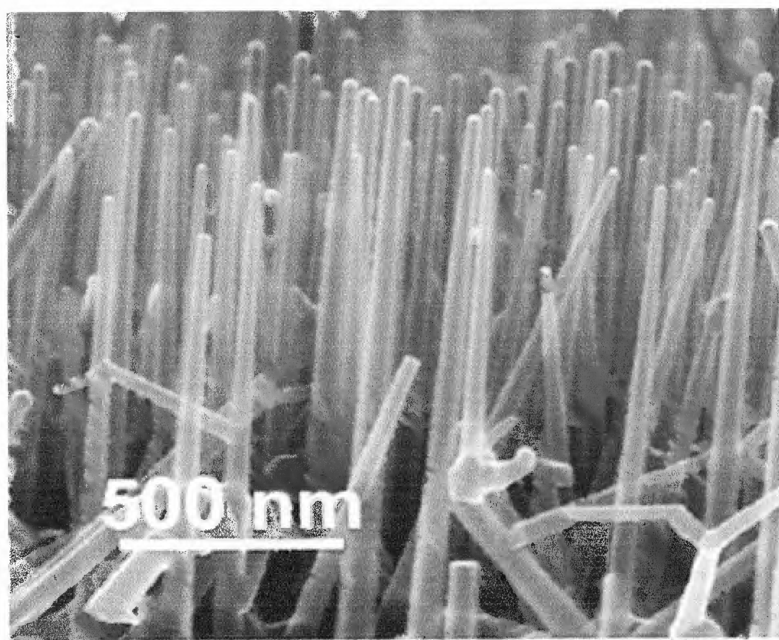

(b)

Figure 3.1 SEM image of Ge NWs (a) on (100) n^+ Si substrate and (b) on (111) p^+ Si substrate [10].

By optical characterization of the Ge NWs on Si substrate, additional information was obtained. Raman and low temperature PL spectra of Ge NWs on Si substrate are shown in Fig. 3.2a and b, respectively.

In the Raman spectrum of Ge NWs on (100) n^+ Si substrate, there are only two clear Raman peaks originated from Si substrate and Ge NWs, respectively; Si-Si vibrations at ~520 cm^{-1} and Ge-Ge vibrations at ~300 cm^{-1}. Fully symmetric and narrow FWHM of ~6 cm^{-1}, which is comparable with that of the bulk Ge, provides an additional proof that Ge NWs are unstrained and have high crystalline quality. Moreover, absence of Si-Ge vibration implies that Ge NWs/Si substrate interface region is very thin. With the Ge NWs samples grown on (111) p^+ Si substrate, very similar spectra were obtained.

The main PL spectrum peak, TO of Ge NWs on (111) p^+ Si substrate, which originates at the Ge NWs/Si substrate interface other than Ge NW volume or Si substrate [5], is red-shifted and broader compared to the PL spectrum from NWs grown on (100) substrates. This indicates that the intermixing at the base of NW is more efficient in samples grown on (111) substrate; Kamenev et al. attributed it to the difference of initial stage of NW growth due to the crystallographic orientation and possible differences in strain resulting from the differently oriented substrates.

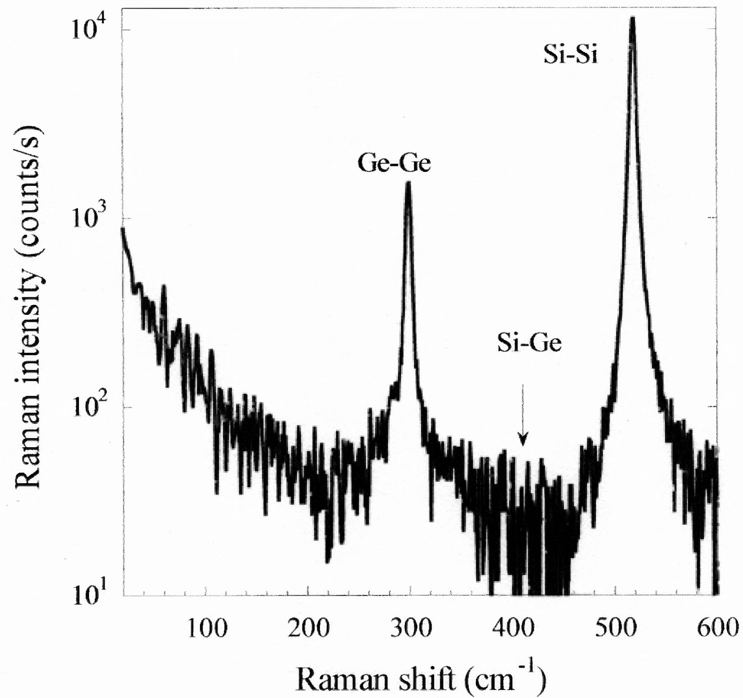

(a)

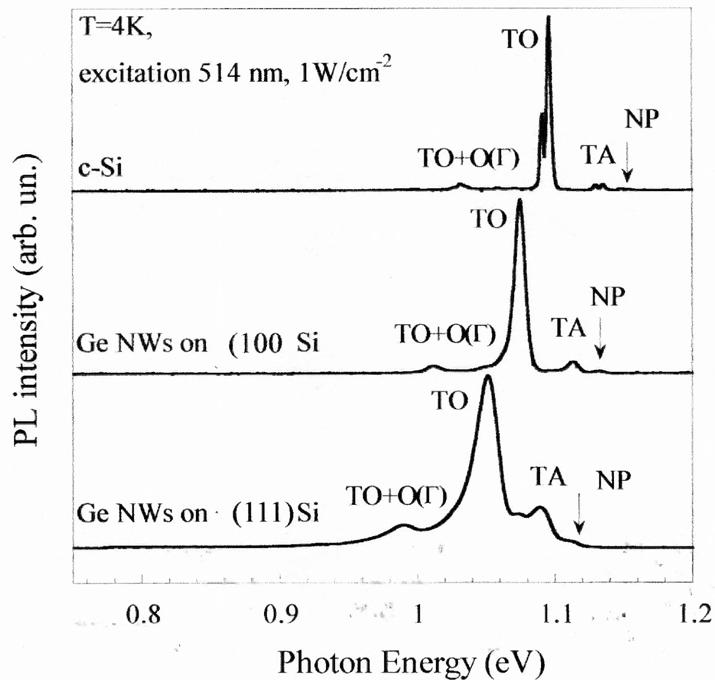

(b)

Figure 3.2 (a) Raman spectrum of the Ge NWs with an estimated NW length of 360 nm grown on a (111) p^+ Si substrate and (b) Low temperature PL spectra of c-Si, Ge NWs grown on (100) n^+ and (111) p^+ Si substrates [5].

3.1.2 Si/SiGe Cluster Superlattice Samples

The Si/SiGe clusters SL samples were grown by CVD or MBE. The samples structures consist of multiple layers of Si separating layer and SiGe clusters with different layer thicknesses and SiGe clusters sizes. The details are provided in Table 3.1.

Table 3.1 Structural data of Si/SiGe clusters SL samples; number of periods N; SiGe clusters heights d_{SiGe}; Si separating layer thickness d_{Si}.

Sample (Method)	d_{SiGe}, nm	d_{Si}, nm	N
`990 (CVD)	~3-7 nm	~10	10
991(CVD)	~3-7 nm	~20	10
1078(CVD)	~3-7 nm	~7.5	10
1813 (MBE)	~7 nm	~15	10
1831 (MBE)	~4 nm	~15	10

The CVD samples were prepared in a load-locked, single-wafer, lamp-heated CVD reactor in a H_2 ambient. The Si substrates were 15-25 Ω·cm Si (100) wafers, on which an undoped Si buffer layer was grown. The Ge was deposited at 600 °C using GeH_4 in H_2, with a total reactor pressure of 1.33 kPa. The Si separating layers were deposited at 600 °C using SiH_4, and each Si separating layer was 7.5-20 nm thick. Ten-pairs of Ge/Si layers were deposited. The Ge deposition rate was ~6 eq.-ML/min for 1 min to form well-defined pyramid-shape SiGe clusters with typical base lengths of ~30-70 nm and heights of ~3-7 nm.

The two MBE samples (1831 and 1813) studied in this work were grown in a VG Semicon V80 system using a methodology described in detail elsewhere [65, 66]. The substrates were lightly p-doped 10 Ω·cm Si (100) wafers. The sample 1831, grown at temperature T~650 °C, consists of 10 period $Si/Si_{1-x}Ge_x$ multiple layers with x~0.55 close to the middle of the SiGe clusters, and the sample 1813, grown at T~625 °C, consists of 10 periods of $Si_{1-x}Ge_x$ (x~0.53). TEM studies (Fig. 3.3) have shown that the Si/SiGe multilayers exhibit SiGe clusters vertical alignment [67]. The SiGe clusters height and Si separating layer thickness were kept constant throughout the entire multilayer structure. In addition, X-ray reflection and Raman measurements indicated that samples had chemically abrupt interfaces between the SiGe clusters and the Si separating layers [68].

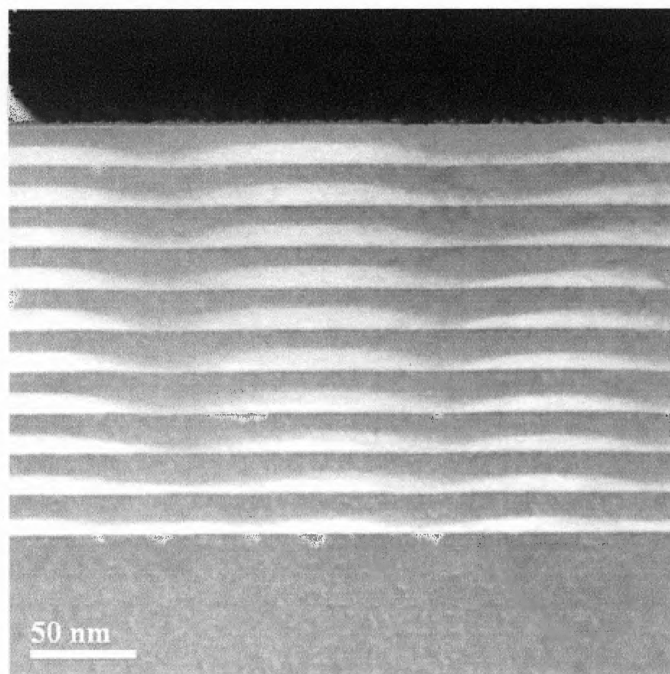

(a)

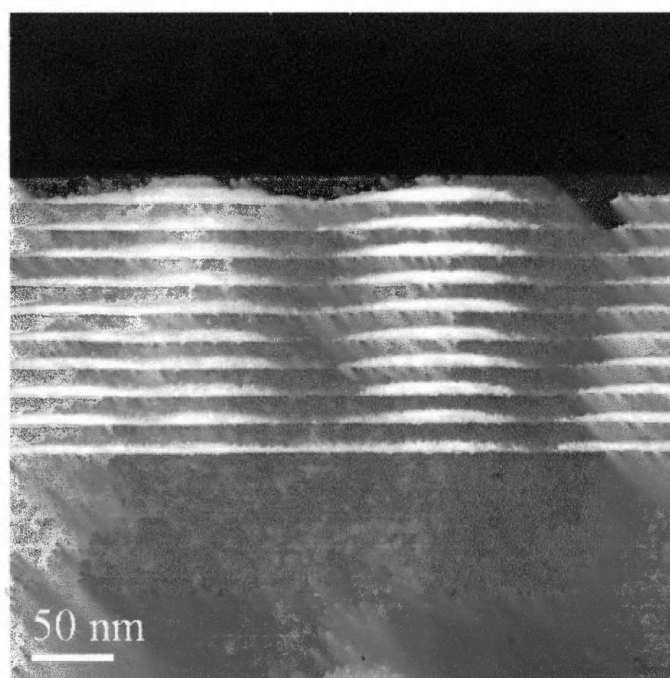

(b)

Figure 3.3 TEM images of MBE-grown Si/SiGe clusters SL samples: (a) sample 1813 and (b) sample 1831.

3.1.3 Contact Fabrication

Conventionally, the electrical studies of semiconductor NW have been focused on carrier transport in the NW rather than the electrical connection between the grown NW and the underlying substrate. Moreover, little information is available in case of lattice mismatched semiconductor NWs (e.g., Ge NWs) grown on Si platform. In this study, the electrical measurements were performed with two contacts fabricated on tips of Ge NWs and on back side of Si substrate. Thereby, carrier transport in Ge NW/Si substrate heterostructures with different types of Si substrate doping was investigated.

As a back side contact, indium was pressed onto the bottom of Si substrate. The indium contact has the advantage of being chemically stable once placed and robust to attachment of wires for electrical measurement.

Top contacts were made with different configurations. A graphite or metal contact was used for each configuration. For the measurement of 1400 nm-long Ge NWs on (100) n^+ Si substrate, two samples were prepared by fabricating different contacts on Ge NWs: one sample with metal contact which penetrates presumably toward the Ge NWs/Si substrate heterojunction interface and the other with a graphite contact on the tips of Ge NWs (Fig. 3.4).

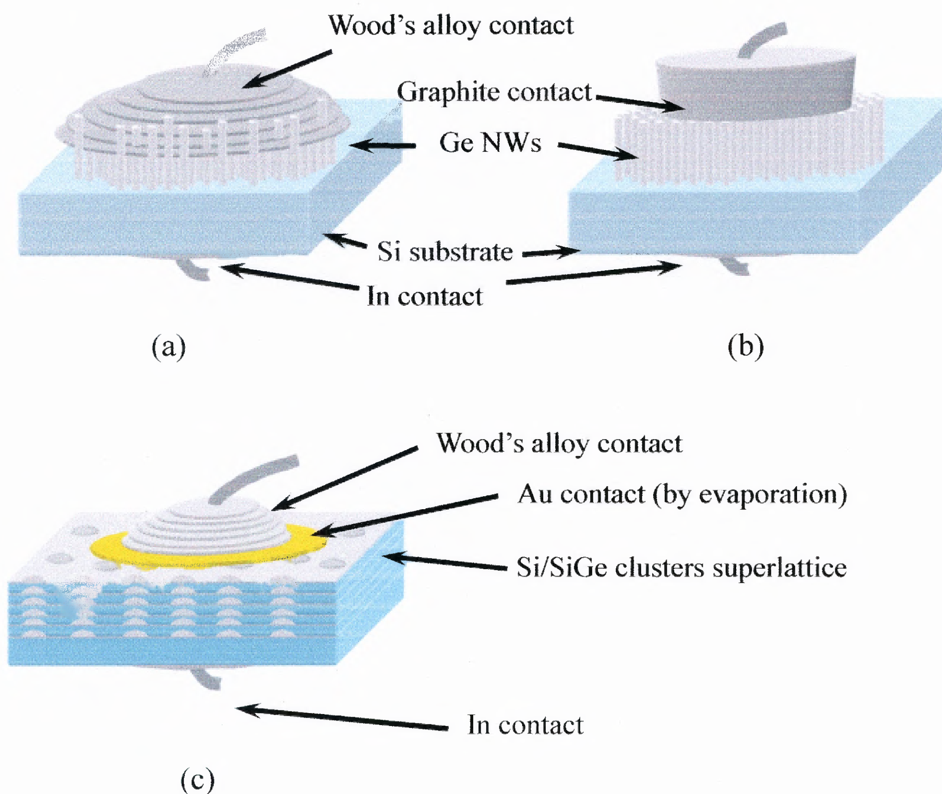

Figure 3.4 Schematic representations of the samples with contacts: (a) Wood's alloy contact and (b) graphite contact configuration on Ge NWs/Si substrate samples and (c) Wood's alloy contact configuration on Si/SiGe clusters SL sample.

The metal contact was fabricated by soldering Wood's alloy on the Ge NWs at low temperature. Wood's alloy is composed of bismuth, lead, tin, and cadmium, and the melting point is about 70 °C. In addition, it was necessary to guarantee the wood's alloy not to make a direct contact on Si substrate. A reference contact was made with Wood's alloy on the top of substrate for this purpose. By observing quite a different *I-V* characteristic from the measurement with the reference contact, compared to that with the Wood's alloy contact on top of Ge NWs, a successful contact fabrication was confirmed. The graphite contact was achieved by locating a sharp graphite tip on the Ge NWs.

Two more samples were prepared with graphite contacts on 360 nm-long Ge NWs on (111) p^+ Si substrate and the same length Ge NWs on (100) n^+ Si substrate.

For electroluminescence (EL) measurements, a CVD-grown Si/SiGe clusters SL sample (sample 991) was prepared with Au contacts on the surface with diameter of ~1 mm. Au was thermally evaporated through a metal shadow mask (Fig. 3.3c).

3.2 Measurements Setup and Procedures

3.2.1 Electrical Measurements

The arrangement of experimental apparatuses used for electrical measurements on Ge NW/Si substrates samples is shown in Fig. 3.5. The samples were placed in a sample holder with a cold finger inside a He closed-cycle cryostat and the sample temperature was controlled between 8 and 300 K. The cryostat chamber is equipped with two copper wires for sample biasing.

A He-Ne laser (633 nm, 5 mW) was used for sample photoexcitation in the electrical measurements. The laser beam was focused and guided with several lenses and mirrors to the sample through one of the cryostat windows (Fig. 3.5).

An electrometer (Keithley 6517A), which can generate DC source voltage, was used for the *I-V* measurement. The admittance data were measured by an impedance analyzer (HP 4192A). The impedance analyzer was operated in self-scanning mode under the control of a personal computer (PC).

A LabVIEW program developed for the electrometer and the impedance analyzer was used for all data acquisition and measurement control. Both *I-V* and admittance data were collected and recorded to PC and all the specifications of measurement, such as applied voltage and frequency range, sweeping interval during frequency and voltage scanning measurement, and oscillation level, was controlled by this program.

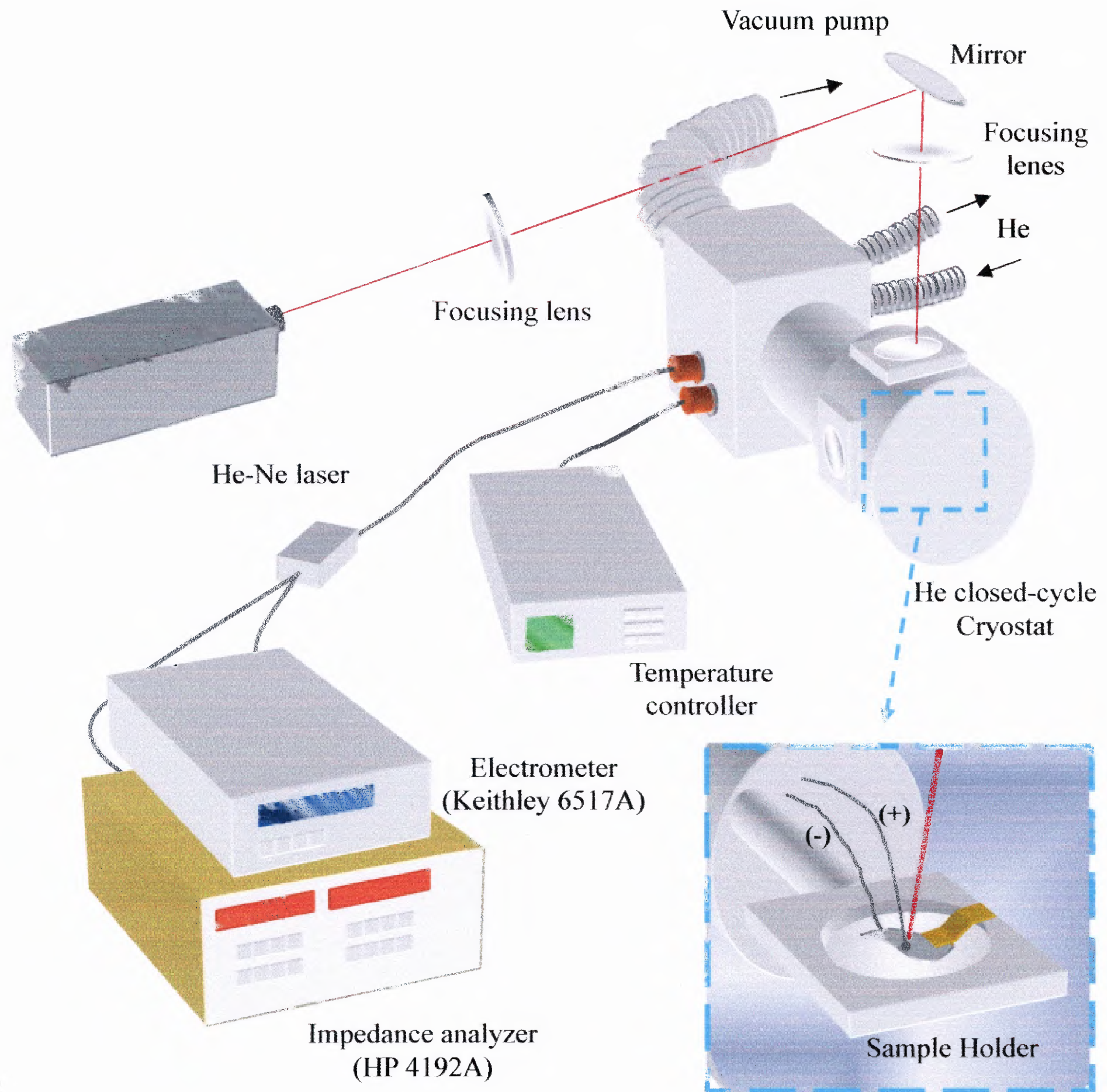

Figure 3.5 Apparatus setup for electrical measurements.

During admittance measurement, parallel conductance and capacitance of the sample were measured by selecting corresponding circuit mode in the LabVIEW program window between series R and X (impedance) mode and parallel G and C (admittance) mode. For each sample, conductance and capacitance as a function of bias voltage (G-V

and *C-V*) at a number of fixed frequencies were measured as well as conductance and capacitance as a function of frequency (*G-f* and *C-f*) at several fixed bias voltage. *G-V* and *C-V* scanning (In LabVIEW program, it is represented as voltage sweep mode) can be performed simultaneously at each selected fixed frequency and the same are *G-f* and *C-f* at each bias voltage (frequency sweep mode). At each scanning, the same measurements with sample illumination were also carried out. During the voltage scanning, frequency was sweeping up with logarithmical intervals between 5 Hz to 1.3 MHz automatically, where 130 points were selected, and for frequency scanning, voltage step was set to 10 mV. Oscillation level of source voltage was set to 30 mV.

For the electrical measurements on Si/SiGe clusters SL samples, a scanning-tunneling-microscope (STM) (attocube attoSTM-I) equipped with a liquid bath cryostat was used. The measurements were carried out at T=77 K by filling the bath with liquid nitrogen. After STM tip (cut $Pt_{0.9}Ir_{0.1}$ tip) automatic approach on the sample surface, *I-V* characteristics were measured using 'bias spectroscopy mode' offered by the system software. The *I-V* characteristics were spatially mapped by positioning the tip at local points 50 nm apart in *x* or *y* directions (parallel to the sample surface) as is schematically shown in Fig. 3.6. The *I-V* curve was scanned in a voltage range from -6 to 4V.

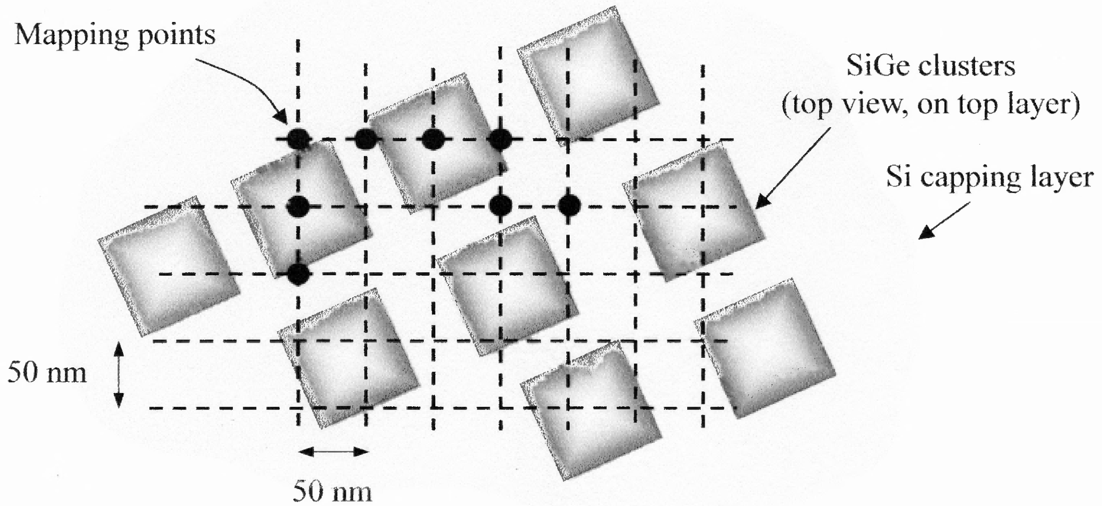

Figure 3.6 A schematic illustration of *I-V* mapping points.

3.2.2 Optical measurements

Figure 3.7 shows apparatus configuration used for PL measurements. For CW PL measurements, an Ar^+ laser (100 mW) was used for sample excitation. The laser can produce wavelengths of 514, 488, 457 nm and a multi-line as well. The excitation was in most case a multi-line modulated between ~100-200 Hz by a mechanical chopper, and the intensity varied from 0.1 to 10 W/cm^2. The PL signal from the sample was collected with two consecutive lenses placed along an optical path from a side window of the cryostat to a 0.5 m monochromator with single grating (Acton Research), where the signal was dispersed with spectral resolution of ~1 meV. The dispersed signal was detected by an air-cooled InGaAs photomultiplier tube (PMT) (Hamamatsu) using a standard lock-in technique in the spectral range 0.9-1.6 μm. During the measurements the

sample was kept in a closed-cycle He cryostat and the temperature was controlled between 8 and 300 K. The acquisition of spectra was controlled by a personal computer.

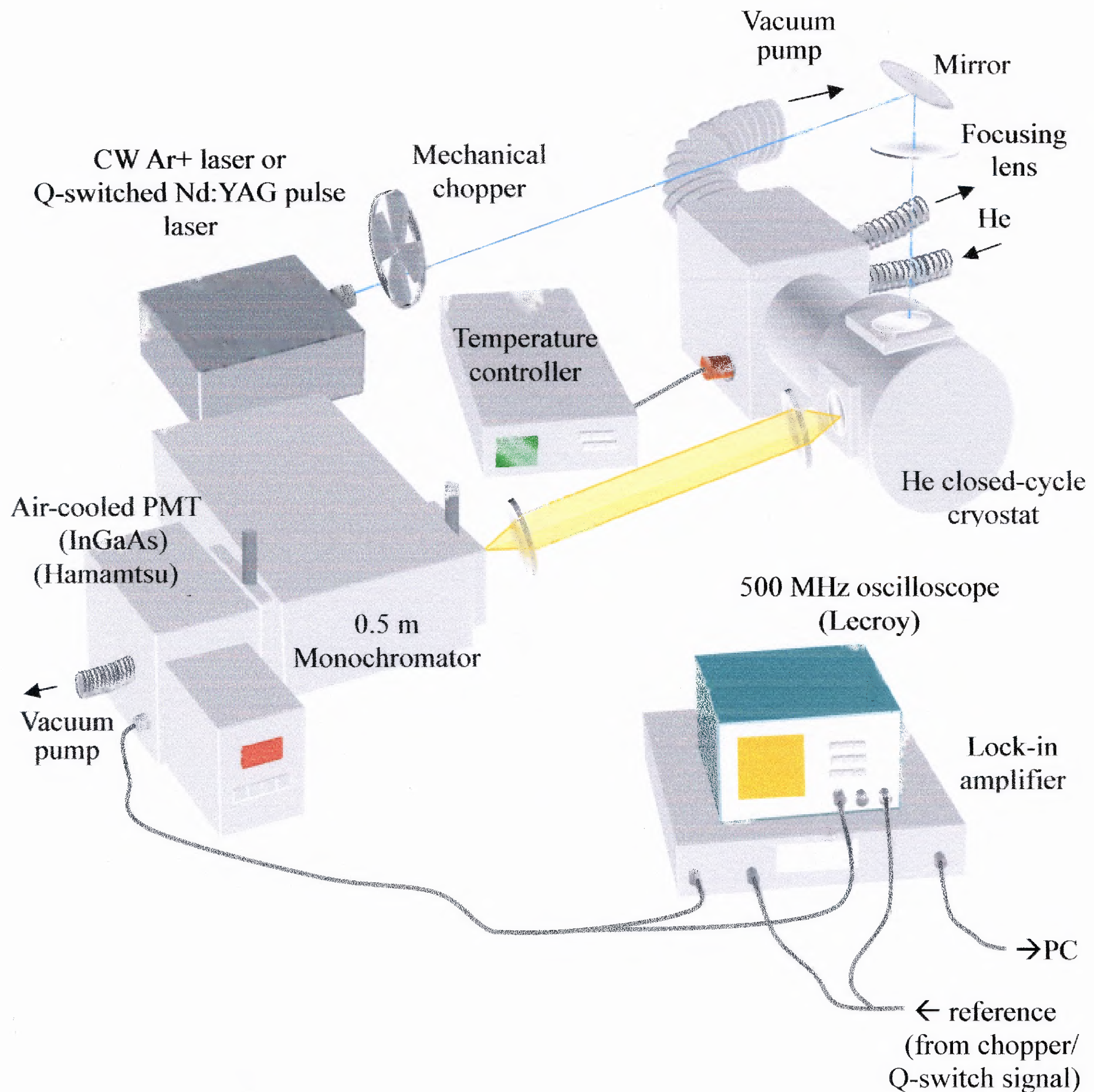

Figure 3.7 Apparatus setup for optical measurements.

For PL measurements under a pulsed laser excitation, a Q-switched Nd:YAG laser (Quentel) was used as an excitation source. The laser generates 6 ns duration pulse with a controllable repetition rate <20 Hz. The excitation wavelength was 532 nm using a

second harmonic generator. The laser pulse energy was attenuated using neutral density filters from 0.1 mJ/cm^2 to 10 mJ/cm^2. In PL decay measurements, the signal from the PMT was averaged over 1000 sweep with a 500 MHz digital oscilloscope (Lecroy). The detection time resolution was several nanosecond: the rise time of PMT was ~1 ns.

CHAPTER 4

RESULT AND DISCUSSION

4.1 Ge Nanowires/Si Substrate Heterostructures

As discussed in section 3.1.1, the previous optical studies on the samples have shown abrupt interfaces with a very thin Ge-Si transition layer, most likely due to the high growth rate and relatively low temperature of the VLS growth [5]. Here, a study of carrier transport in Ge NW/Si substrate heterostructures with different (p^+ and n^+) types of Si substrate doping is presented.

Initially, in this study, electrical measurements with respect to DC and AC conductivity were performed at room temperature on different length Ge NWs samples using graphite contacts on the tips of the NWs. After these measurements, the experimental focus was directed to the interfaces at Ge NWs and Si substrate heterojunctions, and the samples with the same length Ge NWs on different types of Si substrates were explored using metal contacts on the Ge NWs. *I-V* temperature dependences of the samples were investigated. During the measurements, interestingly, current instabilities and negative differential photoconductivity were observed in the sample with (111) p^+ Si substrate. The experimental results are explained using a model that considers energy band alignment and carrier transport in abrupt Ge NW/Si substrate heterojunctions.

4.1.1 Room Temperature DC Conductivity

At room temperature, diode-like rectifying *I-V* characteristics are found in samples of Ge NWs on (100) n^+ Si substrates under dark and photoexcitation (using He-Ne laser at 633 nm, 0.1 W/cm^2 intensity) as shown in Fig. 4.1a and b.

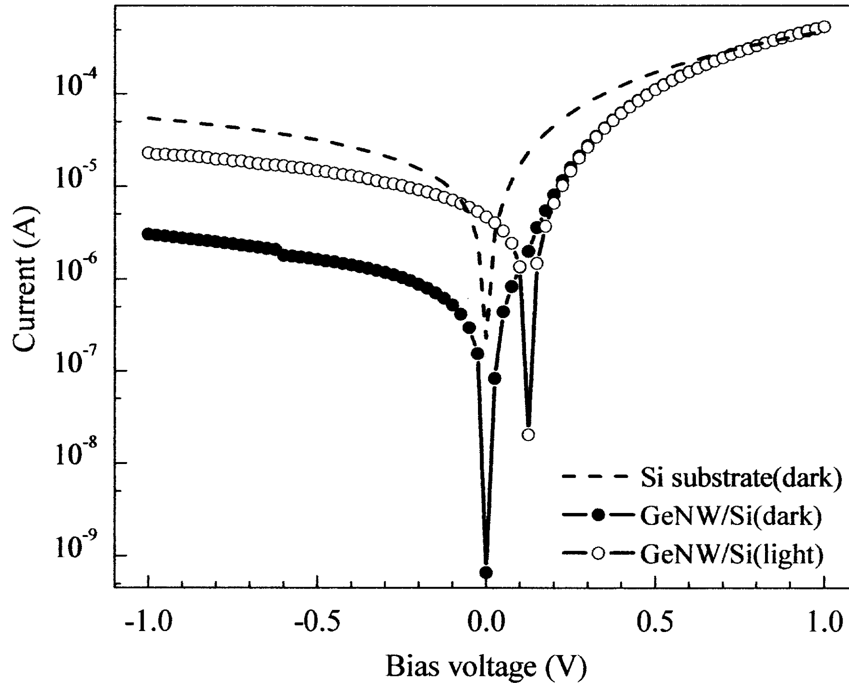

(a)

Figure 4.1 *I-V* data for samples of (a) 1400 nm Ge NWs on (100) n^+ Si substrate, (b) 710 nm Ge NWs on (100) n^+ Si substrate and (c) 1400 nm Ge NWs on (111) p^+ Si substrate with graphite contacts. *I-V* data measured using a graphite tip touching Si substrate surface outside of the Ge NW area are also plotted (dashed lines).

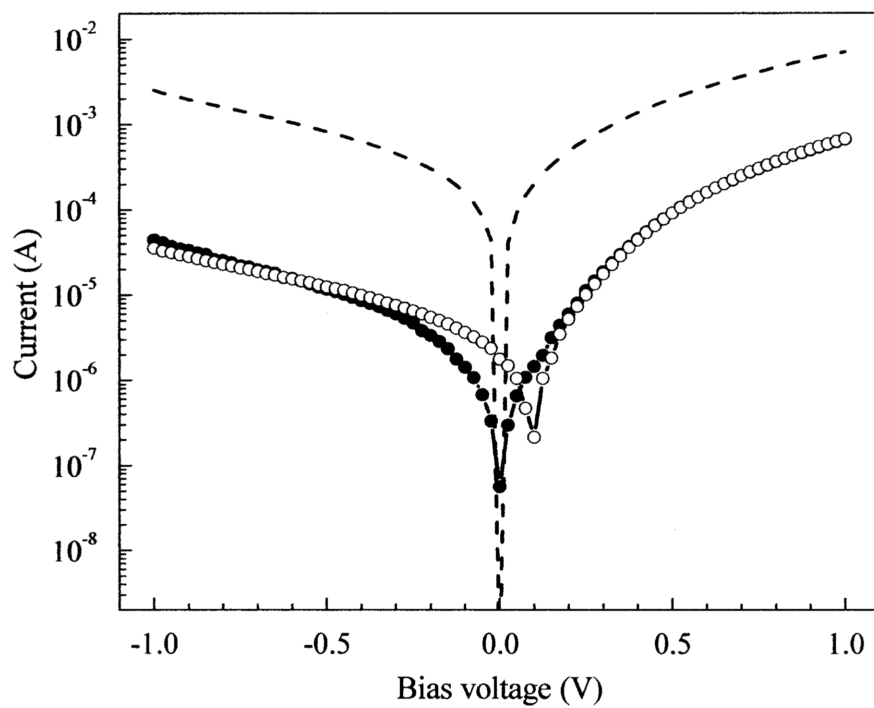

(b)

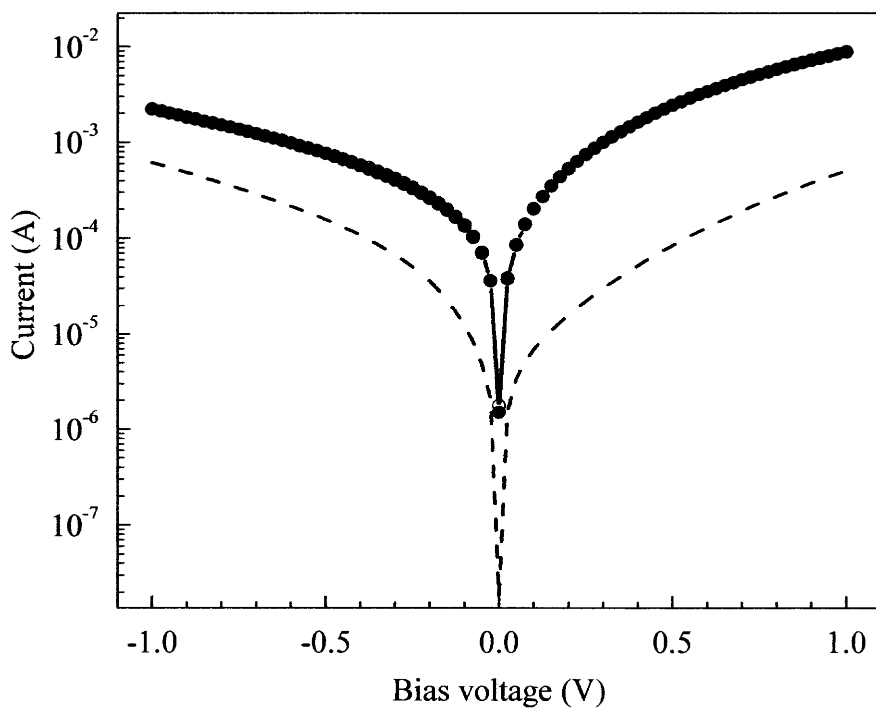

(c)

Figure 4.1 (continued)

A nearly parallel shift of *I-V* curves under photoexcitation is attributed to photocharging. The observed shifts of *I-V* curves are greater for longer Ge NWs, indicating that the charging in part can be associated with Ge NWs surfaces (presumably covered by Ge oxide). Samples of Ge NWs on (111) p^+ Si substrate exhibit a larger conductance but no photosensitivity is found under the same illumination conditions (Fig. 4.1c).

4.1.2 Room Temperature AC Conductivity

AC conductance G was measured as a function of AC signal frequency ω for samples with graphite contacts, and it shows several regions with different frequency dependencies. Figure 4.2 shows the data for the samples of Ge NWs on (111) p^+ Si substrates. Several types of $G(\omega)$ dependencies are observed: (i) the AC conductance is frequency independent at low frequencies (up to 1 kHz), (ii) from 1 kHz to 30 kHz, the AC conductance frequency dependence follows a power law $G \sim \omega^s$ with the power $s \sim 0.35$ for shorter and $s \sim 0.45$ longer Ge NWs on (111) p^+ Si, (iii) the AC conductance is frequency independent from 30 kHz to 1 MHz, (iv) it again follows the power law with $s \sim 1$, most likely due to a high-frequency contribution from space charge region in Ge NWs/Si substrate heterointerface. The observed power law in conductivity frequency dependence at relatively low frequencies is attributed to carrier hopping processes where carriers are localized on energy levels associated with structural defects within Ge NWs. The AC conductivity due to electron hopping between localized centers is known to have a similar dependence $\sigma_{AC}(\omega)=A\omega^s$ [69], where A is a constant which depends on temperature, ω is the angular frequency of the signal and s is generally <1.

The observed AC conductivity and photoconductivity in the samples of Ge NWs on (100) n^+ Si substrates show similar frequency dependencies. Strong photosensitivity of Ge NWs on (100) n^+ Si substrate samples is accompanied by insignificant frequency dependence (Fig. 4.2c).

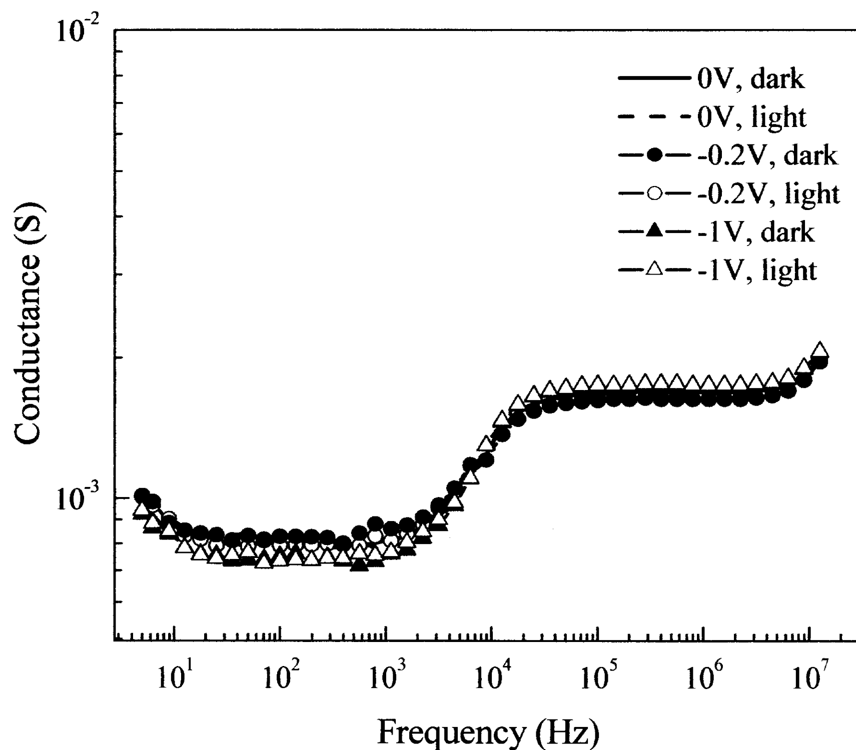

(a)

Figure 4.2 Conductance curves of (a) 1400 nm Ge NWs on (111) p^+ Si substrate, (b) 710 nm Ge NWs on (111) p^+ Si substrate and (c) 1400 nm Ge NWs on (100) n^+ Si substrate as a function of frequency (All the samples with graphite tip contacts).

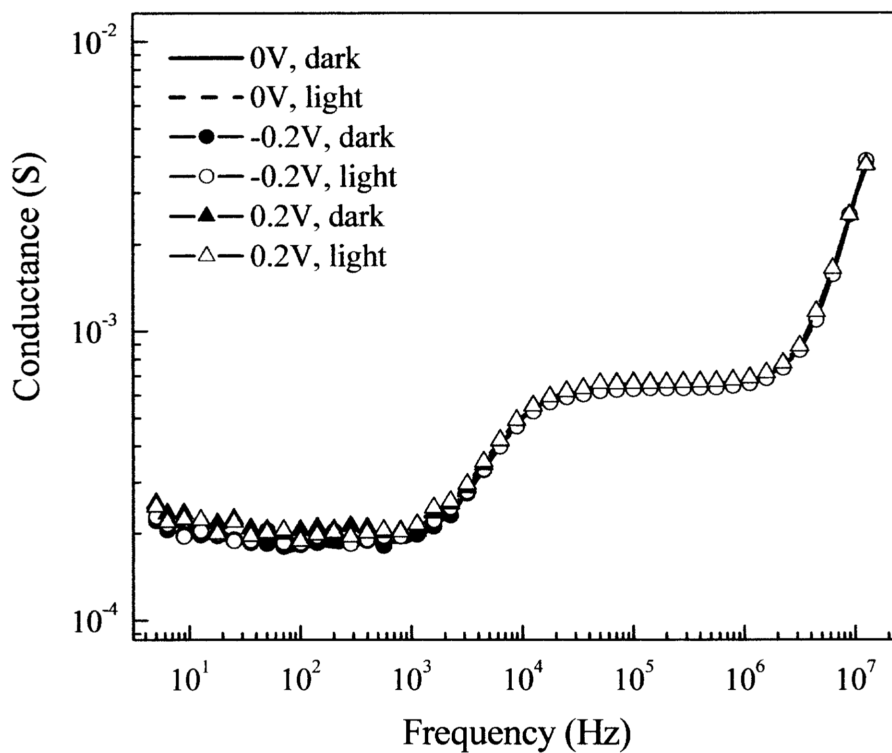

(b)

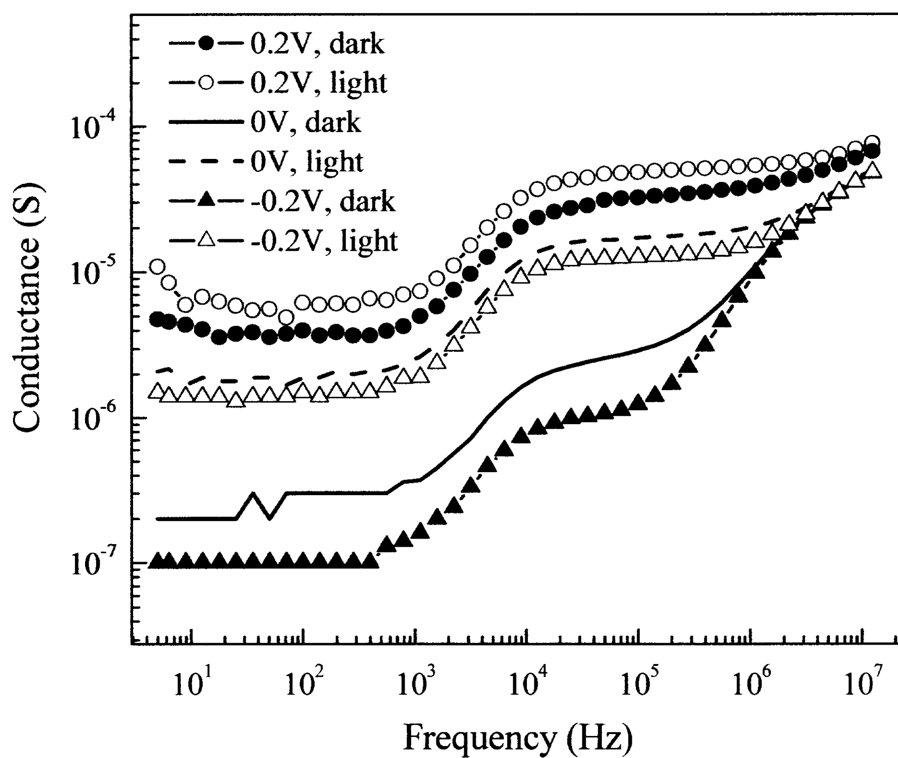

(c)

Figure 4.2 (continued)

The electrical properties of Ge NWs/Si substrate interface were investigated by measurements using samples of Ge NWs on (100) n^+ Si substrate with metal contacts. The observed significant frequency and voltage dependencies of conductance show a rectifying behavior, similar to a semiconductor heterojunction (Fig. 4.3).

The *G-V* data for a sample with a metal contact are consistent with the *I-V* measurements, and the *G-V* curves well correlate *I-V* curves at corresponding bias voltages (not shown). In addition, a large difference (~one order of magnitude) is found between the sample conductance under reverse bias measured under illumination and in the dark. Also, as it is shown in $G(\omega)$ dependencies, by increasing reverse bias and applying photoexcitation, frequency dependence of the junction conductance is decreased. This junction behavior is due to a wider space-charge region and higher concentration of photocarriers at Ge NWs/(100) n^+ Si interface.

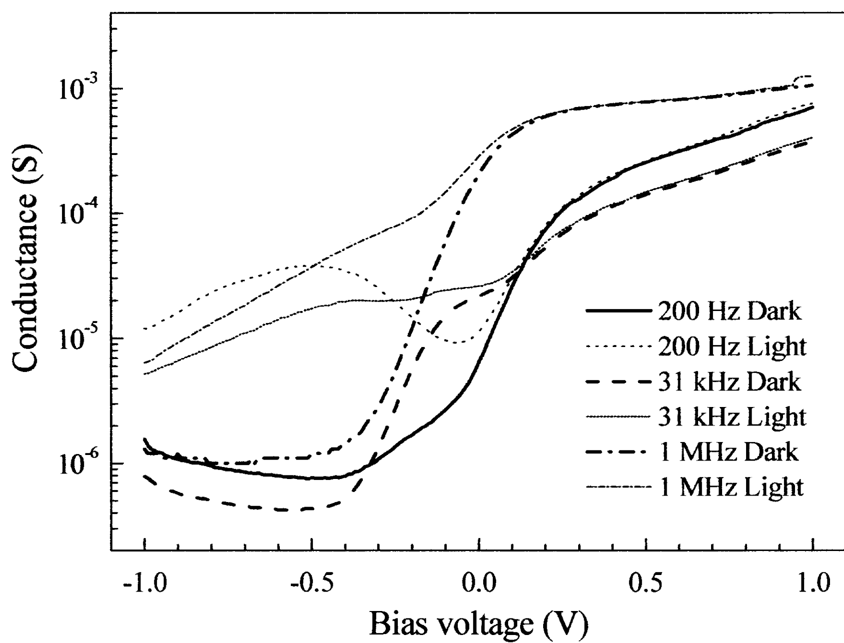

(a)

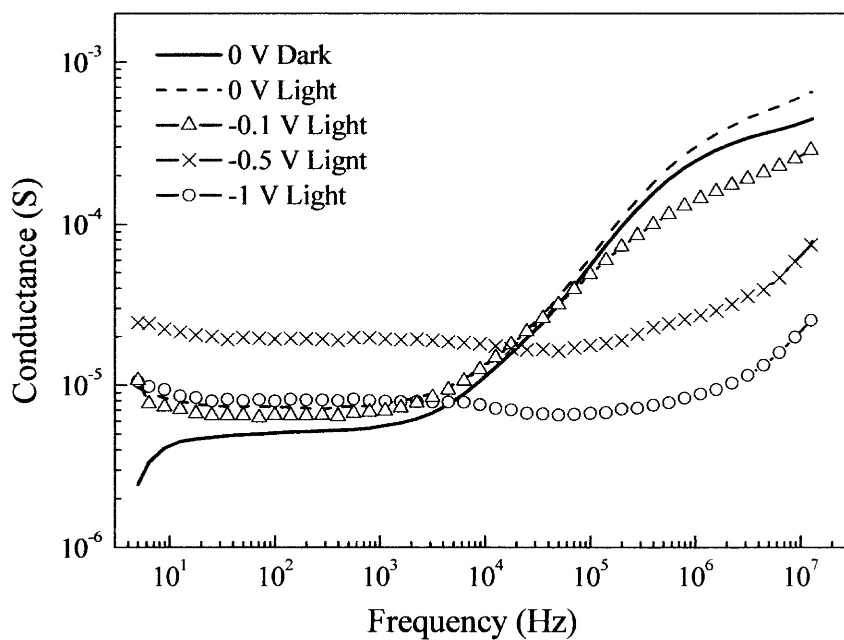

(b)

Figure 4.3 Conductance curves of 1400 nm Ge NWs on (100) n^+ Si substrate with metal contact as a function of (a) bias voltage and (b) frequency.

4.1.3 DC Conductivity Temperature Dependence

Two samples were prepared with 1400 nm length Ge NWs on (111) p^+ Si substrate and those grown on (100) n^+ Si substrate with metal contacts. All the measurements were performed in the temperature range from 38 to 280 K, and a He-Ne red laser was used for photoconductivity measurements. Figure 4.4 shows the *I-V* curves measured on Ge NWs/(111) p^+ Si substrate in semi-logarithmic and double logarithmic scales.

At forward bias <1 V and low temperatures (T<200 K), a superlinear *I-V* dependence (Fig. 4.4a and b) is found. At temperature T>250 K, very similar and nearly ohmic behavior is found for both, forward and reverse biases. Interestingly, at forward bias $V < 0.1$ V, current increases as temperature increases while at V~1 V, an increase in temperature results in a small current reduction. This behavior indicates a metal-like conductivity with a stronger carrier mobility temperature dependence compared to temperature dependence of carrier concentration. No photoconductivity has been found in these samples as can be seen in Fig. 4.4a.

Figure 4.5 shows *I-V* curves measured on Ge NWs on (100) n^+ Si substrate, which are characteristic of a heterojunction diode with rectifying behavior.

In contrast to the previous sample, Ge NW/n^+ Si samples show drastically different *I-V* data. At temperatures T>250 K, we observe diode-like *I-V* characteristics with easily detectable photoconductivity (Fig. 4.5a). At temperatures 150 K<T<200 K, measurements are complicated by current and photocurrent instabilities (Fig. 4.5b). At temperatures T<150 K reverse current stabilizes but drops drastically to ~10^{-11} A (Fig. 4.6). Dark current and photocurrent temperature dependencies under reverse bias of 0.5 V are summarized in Fig. 4.6.

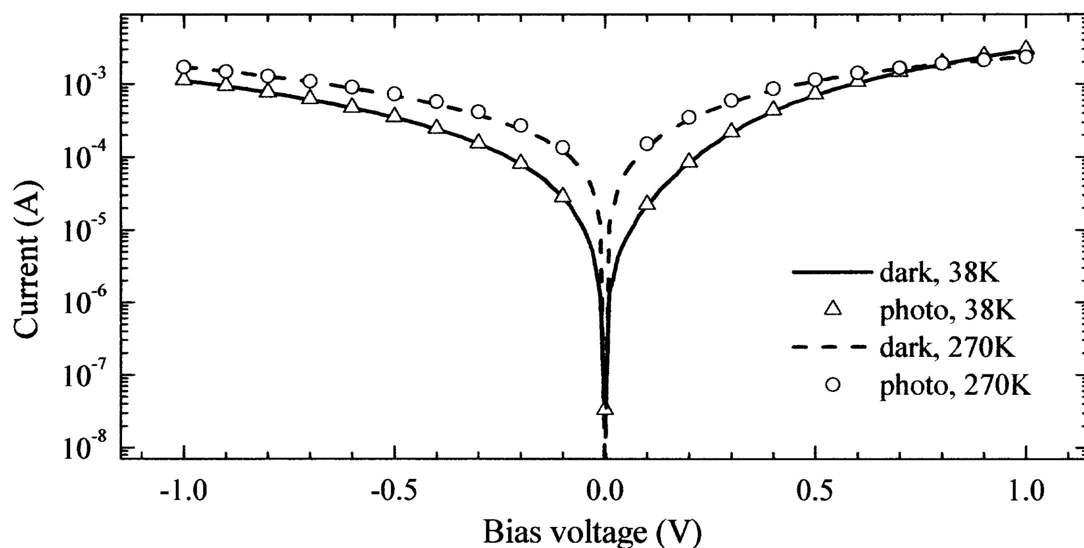

(a)

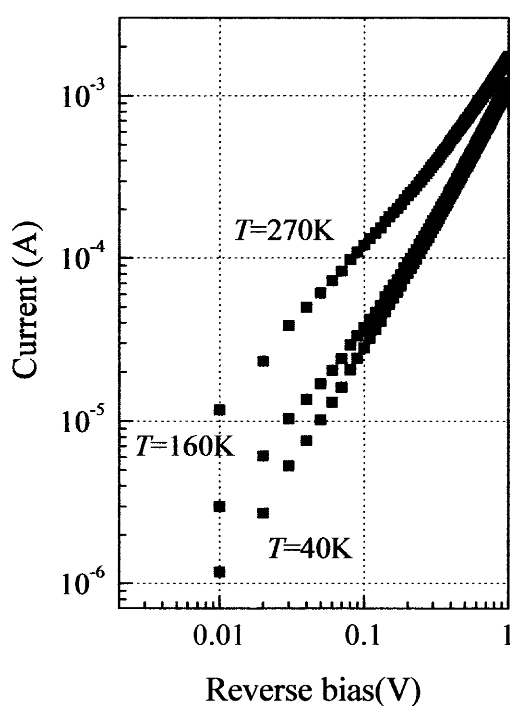

(b)

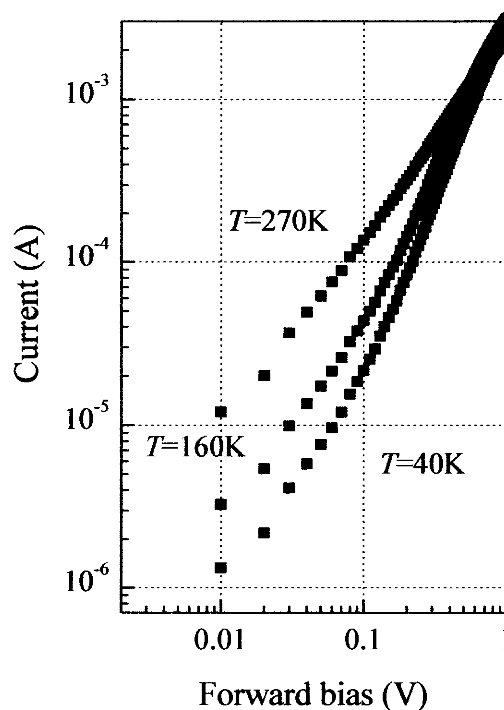

(c)

Figure 4.4 (a) *I-V* characteristics of Ge NWs grown on (111) oriented Si substrate at several temperatures under dark and illumination. The near ohmic dark *I-V* characteristics are shown for (b) reverse bias (positive voltage applied on Si substrate and negative on Ge NWs) voltage and (c) forward bias voltage.

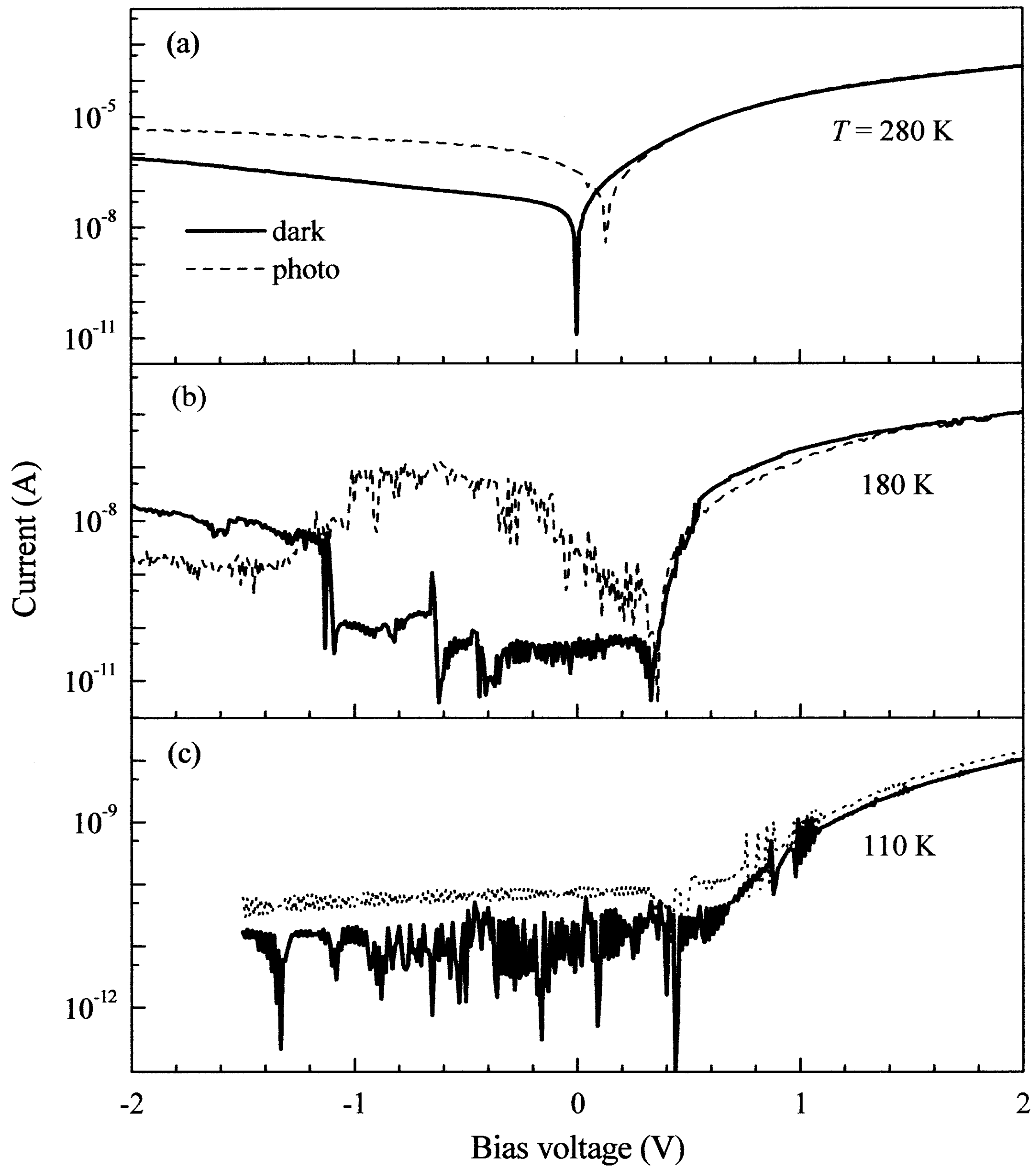

Figure 4.5 *I-V* characteristics in samples of Ge NWs grown on (100) oriented, n^+ Si substrate at three different temperatures (a) T=280 K, (b) T=180 K, and (c) T=110 K.

In both measurements (in dark and under ~100 mW/cm^2 He-Ne laser power illumination), an exponential conductivity temperature dependencies are found with activation energies of ~200 meV and ~60 meV, respectively. At temperatures T<180 K,

both dark current and photocurrent are practically temperature independent. In order to stabilize dark current and photocurrent under a higher reverse bias, a slow-chopped He-Ne laser was used. The current instabilities were detected during the "light-on" time interval, while during "light-off" dark current is found to be quite stable (Fig. 4.6, inset).

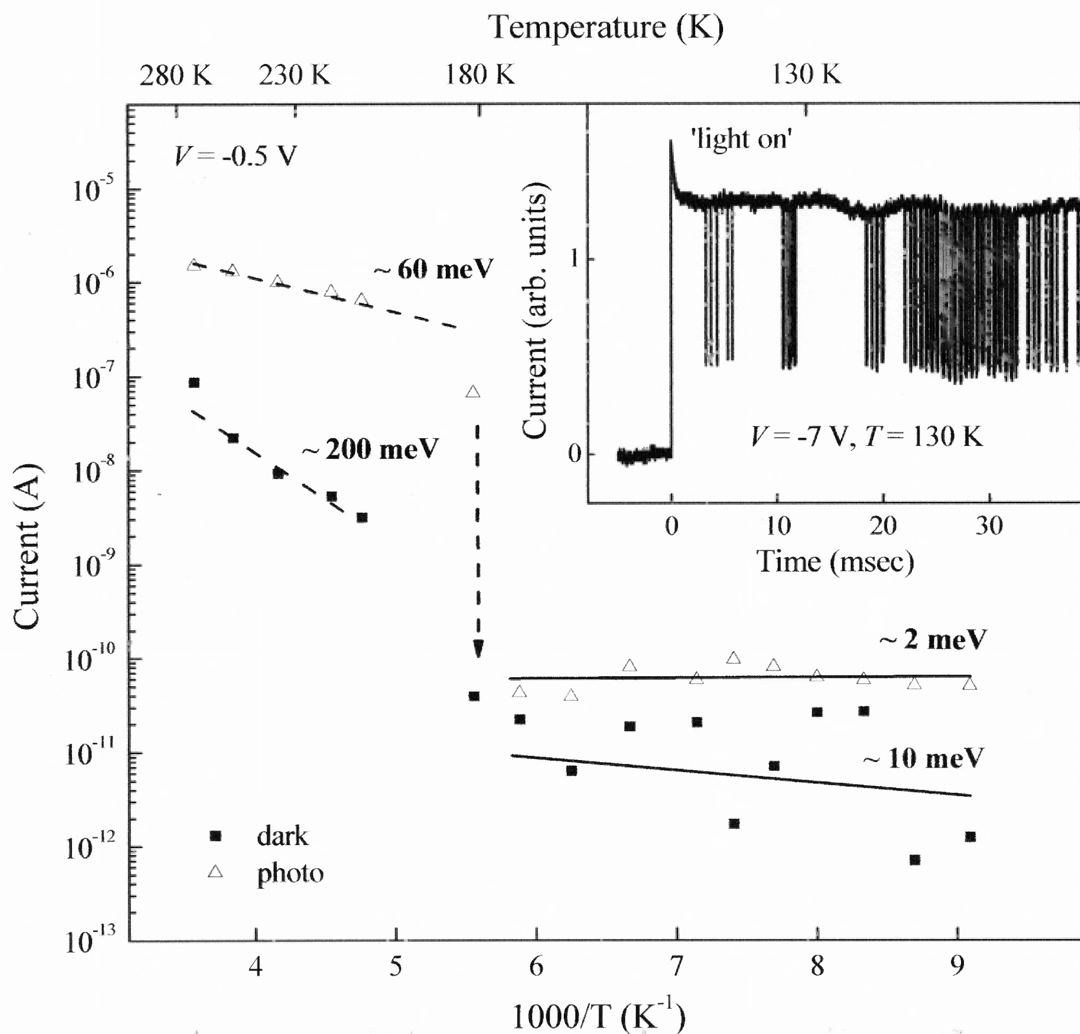

Figure 4.6 Photocurrent and dark current temperature dependences in Ge NW/n^+ Si samples at bias V=-0.5 V. Photocurrent is determined by subtracting dark current, and the calculated activation energies are shown. The inset shows a photocurrent transient under slow-chopped laser with clearly observed photocurrent oscillations during the "light-on" time interval.

During photoexcitation measurements, negative differential photoconductivity (NDP) was observed at relatively small forward bias at the temperature range above 210 K up to room temperature. Figure 4.7 shows details of photocurrent as a function of bias for Ge NW/n^+ Si samples at different temperatures at low level (~100 mW/cm^2) of photo-excitation. During the measurements, the relatively narrow temperature interval was chosen in order to avoid photocurrent instabilities. N-shaped *I-V* curves and negative differential photoconductivities are clearly observed with a peak near 0.3-0.5 V.

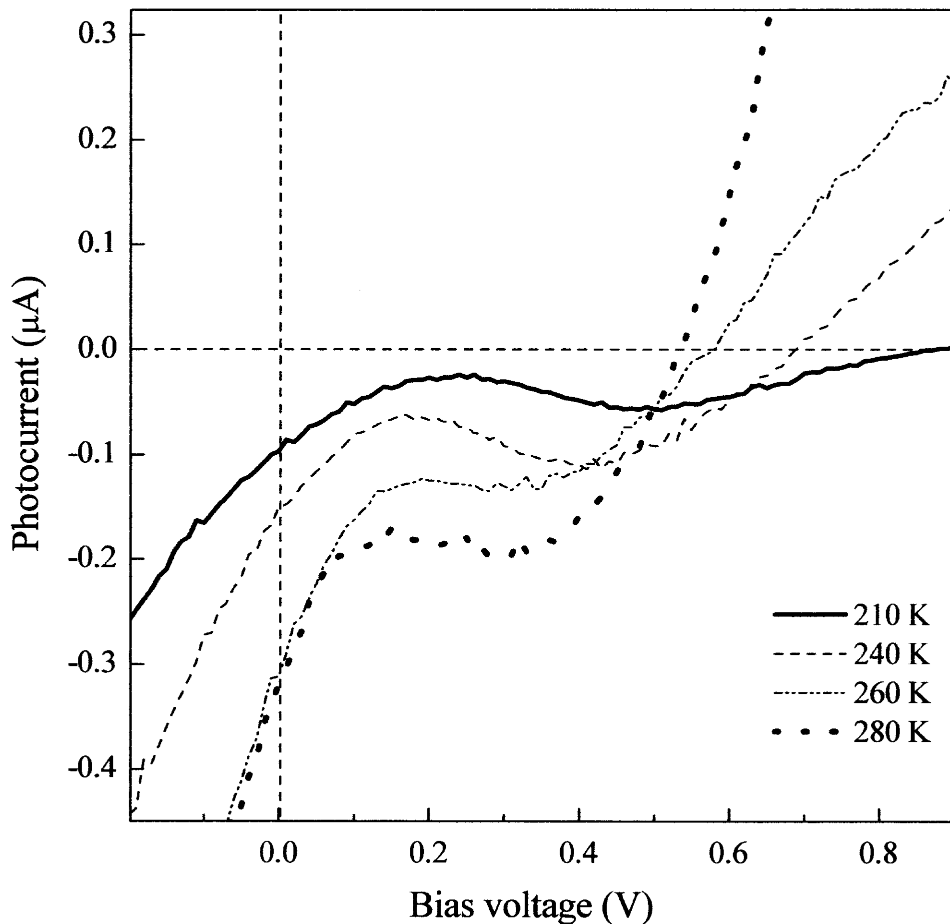

Figure 4.7 Photocurrent as a function of voltage at different (indicated) temperatures in Ge NW/n^+ Si samples showing clearly observed negative differential photoconductivity.

4.1.4 Carrier Transport in Ge Nanowire/Si Substrate Heterojunctions

The discussion starts with Ge NW/p^+ Si samples assuming that the Ge NW/Si substrate interface is abrupt, with a thin SiGe transition layer [5, 70]. Also, it should be considered that surface states on the free surfaces of Ge NW tend to induce *p*-type conductivity [71].

As mentioned previously in section 2.3, Ge and Si have almost the same electron affinity (χ_{Ge}=4.00 eV, χ_{Si}=4.05 eV), and therefore, very small conduction band discontinuity is expected [24, 72]. In addition, since the Ge NW diameter is ~40 nm, the effect of quantum confinement is believed to be negligible [5, 10], and valence band discontinuity of ~400 meV is anticipated due to difference between Si and Ge band gaps. However, for the Ge NW/p^+ Si sample, the observed strongly superlinear current as a function of forward bias between 0.1 V and 1 V at temperatures below 200 K indicates a small potential barrier for holes.

The band alignment, depicted in Fig. 4.8a, shows formation of degenerated hole gas at the Ge NW/p^+ Si interface due to energy band bending and it explains the experimentally observed low sample impedance and almost metallic conductivity with no significant carrier concentration temperature dependence at temperatures T>200 K and voltage approaching ~1 V. Note that significant interface defect density should result in Fermi level pinning, and it would make impossible the formation of degenerated hole gas at Ge NW/Si interface.

For Ge NW/n^+ Si samples, the energy band alignment is quite different, with significant potential barrier for majority carriers (electrons) due to Fermi level position near the middle of band gap in undoped Ge NWs (Fig. 4.8b). Roughly, the conduction band energy barrier can be estimated as less than half of the Ge band gap, and that is

consistent with the observed ~200 meV activation energy at small reverse bias. Also, this activation energy may reflect other thermionic processes (e.g., minority carrier generation, etc.). In these samples, the observed high impedance is due to the Ge NW/n^+ Si interface potential barrier and series resistance of an undoped Ge NWs.

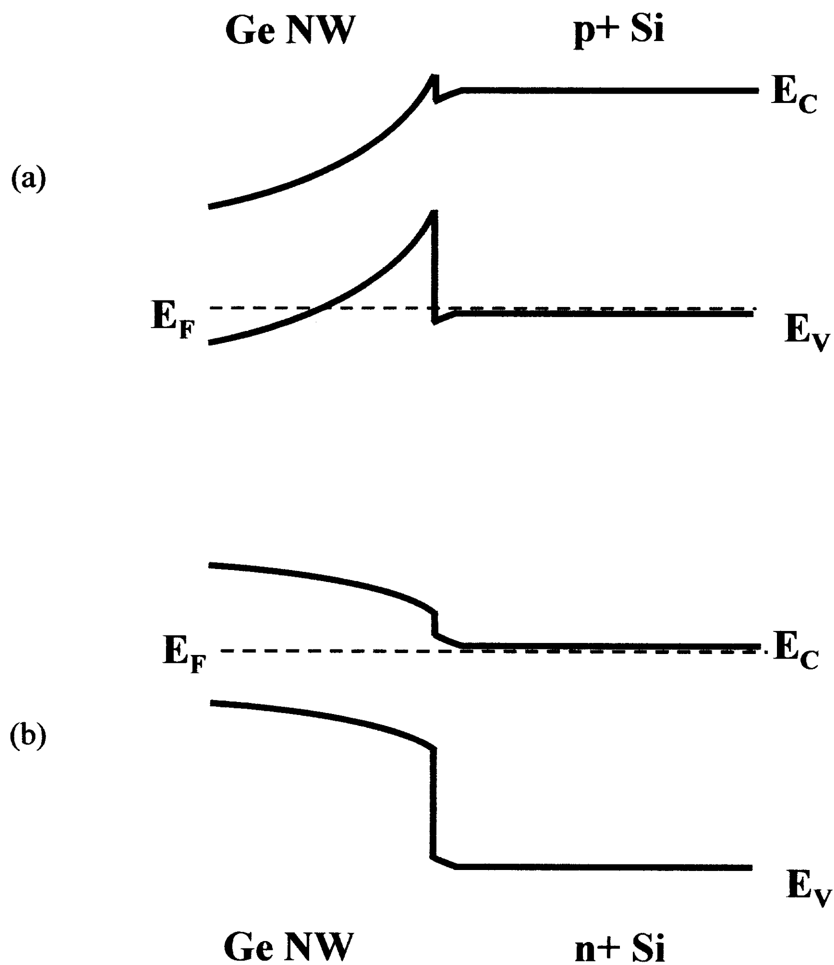

Figure 4.8 The proposed energy band alignment for (a) Ge NW/p^+ Si and (b) Ge NW/n^+ Si heterojunctions.

The proposed energy band alignment, however, explains Ge NW/*n*+ Si sample electrical properties only at temperatures T>180 K. At lower temperatures, the dark current decreases with a much lower activation energy and becomes almost undetectable (<10^{-11} A). At temperatures of 120 K<T<200 K, the photocurrent exhibits instabilities. With further decrease of temperature, the photocurrent also stabilizes at a lower value and shows practically no temperature dependence (Fig. 4.6).

This very unusual behavior can be explained by assuming an abrupt interface between Ge NWs and Si substrate. Both, Si and Ge are indirect band gap semiconductors with conduction band minima located in different crystallographic directions, (111) in Ge and (100) in Si. Thus, electron transport across an abrupt Si/Ge heterointerface requires not only energy conservation but also carrier momentum conservation, most likely via phonon-assisted process. As temperature decreases, the phonon concentration also decreases, resulting in the observed drastic reduction of conductivity and photoconductivity. Dark conductivity temperature dependence is controlled by Ge NW/n^+ Si interface energy barrier, while the observed photoconductivity activation energy of ~60 meV is close to the energy of transverse optical phonons in Si [73].

The observed dark- and photocurrent instabilities, as well as negative differential photoconductivity, can also be explained by considering electron transport across an abrupt, defect-free Si/Ge heterointerface. A sudden decrease in electron mobility for electrons crossing Ge NW/n+ Si substrate heterointerface might lead to a non-uniform distribution of electric field along Ge NWs, similarly to the Gunn effect, which is observed in multivalley semiconductors such as GaAs [74], and also to Γ−X transitions

in III-V based superlattices and heterojunctions [75, 76]. It is worth noting that NDC has also been reported in bulk Ge, but requires a millimeter long single crystal Ge samples.

Finally, important questions should be addressed about structural defects at Ge NW/Si hetero-interface and the role of Si substrate crystallographic orientation. It is well known that, in most cases, VLS-grown Ge NWs have strong (111) preferential crystallographic orientation [77, 78]. Thus, Ge NWs on (111) Si grow straight up, while on (100) Si Ge NWs are inclined of ~55° to the Si substrate normal. Since no pinning of Fermi level has been found in both samples, and photo-sensitivity of Ge NW/n^+ Si samples at temperatures T>180 K is significant, it is concluded that Ge NW-Si substrate interface defect density is low.

The observed drastic decrease of electrical conductivity at low temperature in Ge NW/n^+ Si samples grown on (100) Si might, however, be explained due to carrier capture on defect states. However, a significant density of Ge NW/Si substrate interface defects should result in effective pinning of Fermi level, screening of the electric field and other effects inconsistent with the experimental data. Also, the previously published optical measurements where high efficiency, band-to-band PL is found from the same samples support the conclusion [5].

At the same time, Ge NW outer surface, especially in the case of no intentional passivation, might have some structural defects [3]. Nevertheless, their density should be comparable for both types of micron-long Ge NW samples, grown on (100) and (111) Si substrates. Therefore, a conclusion is that the Si substrate doping is more important for formation of Ge NW/Si heterojunctions and their energy band alignment, while the Si substrate crystallographic orientation mostly controls Ge NW growth directions.

In summary, electrical properties of Ge NWs grown on p^+ and n^+ Si substrates with different, (100) and (111) crystallographic orientations have been studied. The results, including demonstration of nearly metallic conductivity due to degenerated hole gas at Ge NW/p^+ Si heterointerface, observation of step-like temperature dependence in electron transport across Ge NW/n^+ Si substrate heterojunction, current instabilities and negative differential photoconductivity are explained using a model of an ideal Ge NW/Si substrate heterointerface where electron transport is controlled by the interface energy barriers and requires momentum conservation via phonon-assisted process.

4.2 Si/SiGe Clusters Superlattices

Here, this study presents carrier transport and optical properties of 3D Si/SiGe clusters SLs prepared by MBE or CVD.

STM-assisted electrical measurements were conducted on an MBE-grown sample possessing nearly perfect vertical alignment of SiGe clusters. *I-V* characteristics were mapped on the sample surface at a low temperature. The experimental results reflecting lateral inhomogeneity of the sample structure provided critical information to explain carrier transport mechanism in 3D Si/SiGe clusters SL.

Temperature dependent PL measurements were performed under various sample photoexcitation levels using CW Ar^+ laser on the multiple CVD samples with different structural parameters (i.e., different Si separating layer thicknesses) to investigate PL thermal quenching mechanisms. PL dynamics under a high carrier density condition were also studied using a Q-switched Nd:YAG pulse laser.

4.2.1 Carrier Transport in Si/SiGe Clusters Superlattices

An MBE grown Si/SiGe clusters SL sample (sample 1813), which exhibits nearly perfect vertical self-alignment of SiGe clusters (Fig. 3.3a) were investigated with respect to electrical carrier transport by employing an STM technique.

The sample structure consists of 10 periods of $Si/Si_{1-x}Ge_x$ (x~0.55) on a *p*-type Si substrate with Si separating layers thickness of ~15 nm. The SiGe clusters in the sample measure ~7 nm in vertical and ~100 nm in lateral dimension.

The advantage of using an STM tip for electrical measurements compared to a

contacting electrode (e.g., a lithographically defined mesa-type contact) on sample surface is that one can probe a single vertical stack of the clusters since the STM tip provides much narrower current path via tunneling and hence much higher spatial resolution. In the sample, two different vertical transport channels are conceivable depending on the tip location: (i) a channel through a cluster stack which consists of Si/SiGe clusters SL and (ii) a channel between cluster stacks which consists of Si/SiGe WL SL. The latter is practically identical to a Si channel since WLs are very thin and Si-rich.

The measurements were performed at a liquid nitrogen temperature of 77 K via spatial *I-V* mapping procedure on local points separated 50 nm apart on the sample surface as is shown schematically in Fig. 3.6. For sample photoexcitation, a built-in infra-red light emitting diode (LED) attached to the STM scanner was used. The bias-controlled LED intensity was varied 66-500 nW. Since the entire Si/SiGe clusters SL region is ~150 nm thick, the radiation is mostly absorbed in the Si substrate. Therefore, the experimental conditions can be modeled as a metal-insulator-semiconductor (MIS) structure with a vacuum tunneling gap as an insulator, and in the structure, photogenerated carriers are injected from the substrate. Depending on the sign of the applied bias, electron or hole injection takes place in the sample. The bias was applied to the sample while the tip is grounded.

During the measurement, a variety of *I-V* characteristics were achieved proving the experimental capability to resolve the different local transport characteristics. Two different mapping points where their *I-V* characteristics exhibit clear contrast were found as shown in Fig. 4.9 and 4.10.

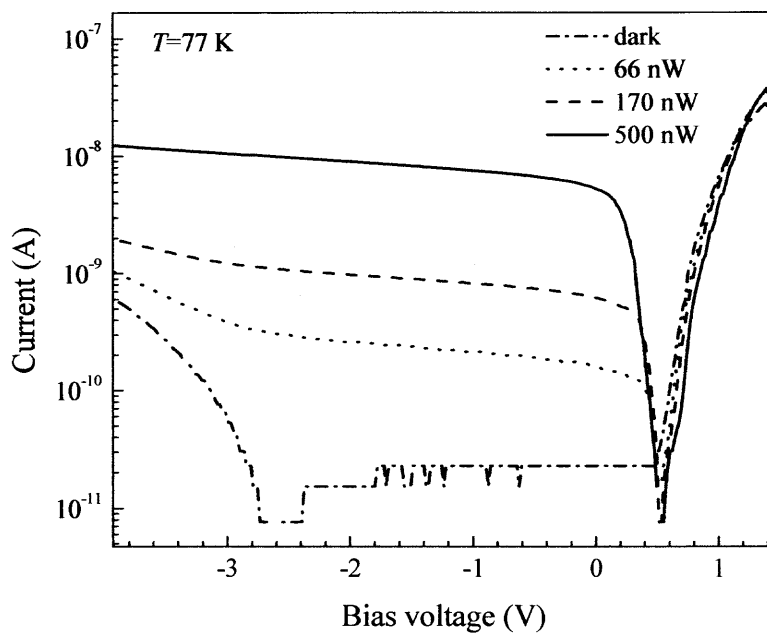

(a)

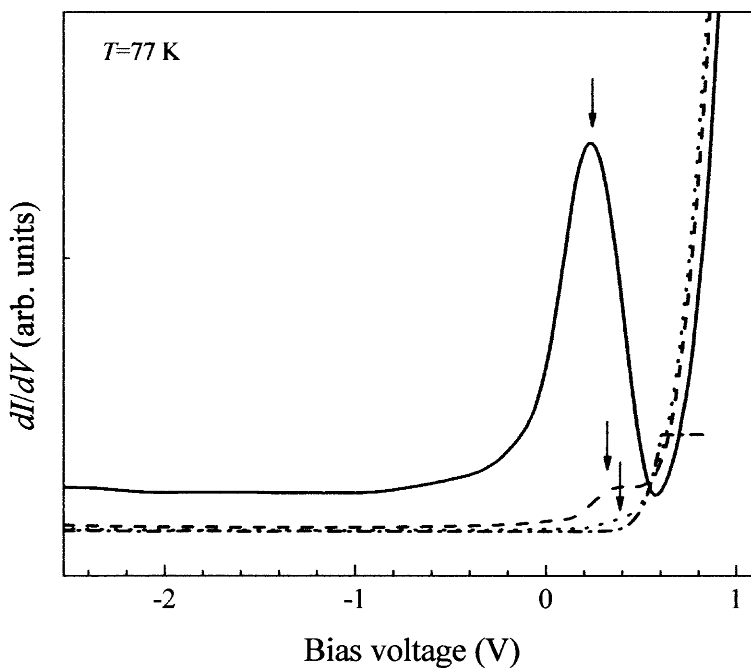

(b)

Figure 4.9 (a) *I-V* curves measured at a local point under dark and different intensity illumination showing typical diode-like characteristics and (b) their differential conductance curves. The sign of the voltage is shown for the bias applied to the Si substrate. Note the different scales (linear or logarithmic) at vertical axes.

In Fig. 4.9a, the *I-V* characteristics observed under positive and negative sample bias are found to be similar to those of a Schottky diode under forward and reverse bias, respectively. Photosensitivity is easily found in the sample under bias voltages below ~0.5. Under dark condition, the sample current exhibits sharp and near exponential increase at $V>0.5$ V with increasing bias up to ~1 V while the current saturates at $-2\ \mathrm{V}<V<-0.5$ V. At higer negative bias <-2, the current shows superlinear increase with increasing negative bias. A possible explanation is a field enhanced detrapping (e.g., impact ionization) process of charges trapped on the sample surface states, which is well-known process in similar MOS structure [79, 80]. Figure 4.9 (b) shows differential conductance curves (*I-V* curves are numerically differentiated). In each curve, a conductance peak (indicated by an arrow) is found at $0.1<V<0.5$. The origin of this behavior will be discussed later.

Figure 4.10 (a) shows *I-V* characteristics measured at the other mapping point. At negative bias, step-like structures are observed under sample illumination, which are manifested as a series of peaks in differential conductance curves at their respective bias voltages of V~0.66, 1.10, 1.85 and 2.60 V (Fig. 4.10b). As shown in the figure, the conductance peaks are observed to be more pronounced (i.e., higher peak-to-valley value) with increasing excitation intensity and bias voltage.

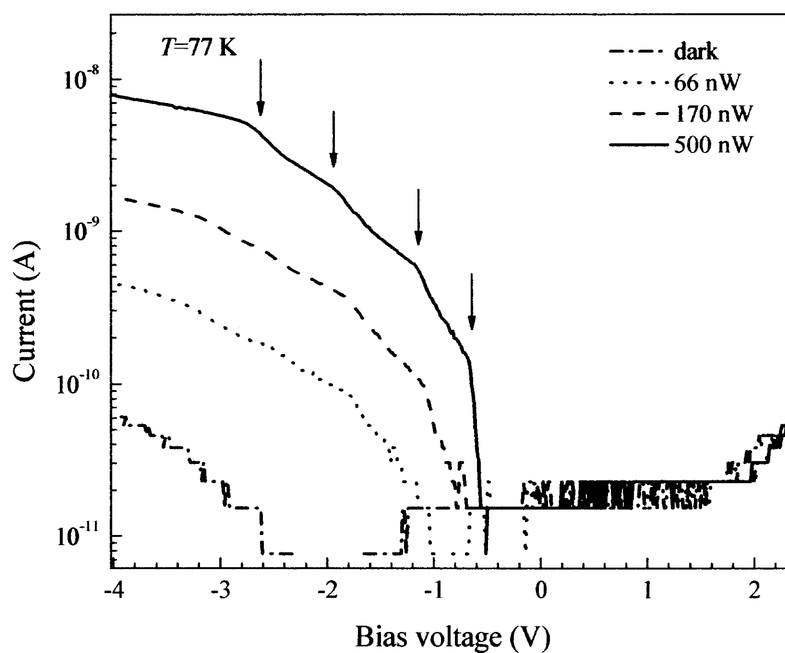

(a)

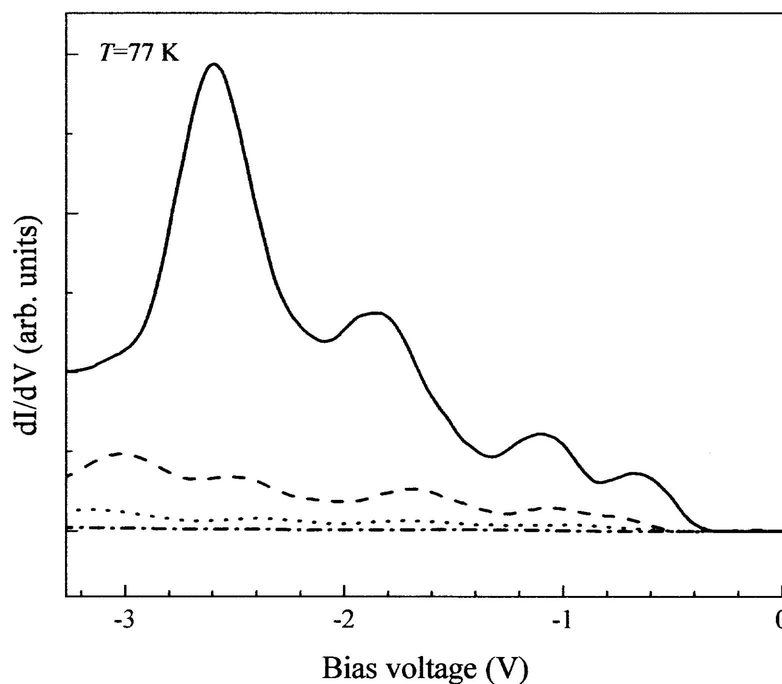

(b)

Figure 4.10 (a) *I-V* curves measured at a local point under dark and different intensity illumination showing step-like features and (b) their differential conductance curves.

Figure 4.11 shows a simple schematic energy band diagram of the sample when the STM tip is at a position between SiGe clusters stacks under different bias conditions, which is basically an MIS structure comprised of Si, an insulating layer and a Pt tip.

This diagram successfully explains the *I-V* characteristics shown in Fig. 4.9a. Thus, the observed transport characteristics are attributed to a vertical channel between SiGe clusters stacks. Without bias, since Pt has high work function of 5.65 eV, the Fermi level of the tip is below the valence band edge of the sample surface (Fig. 4.11a). At small positive sample bias, the holes (majority carriers) in Si are not allowed to tunnel into the tip. When the positive bias increases, the Femi level of the tip is above the valence band edge of Si at the surface, and the holes in Si can tunnel to the tip (Fig. 4.11b). Therefore, the sharp increase observed in the *I-V* characteristic at ~0.5 V can be ascribed to the onset of the hole current tunneling from Si to the tip. However, the condition changes when the sample is illuminated. Photogenerated electrons also contribute to the tunneling current by overcoming the Schottky barrier formed near the sample surface in the conduction band. With the sample bias decreasing from a considerable positive voltage, the photogenerated electrons start to tunnel into the tip over the Schottky barrier (diffusion current). With further decrease of positive bias voltage, when the barrier height becomes small at V~0 V, the electron current exhibits saturation (drift current). This accounts for the conductance peaks observed at 0 V<V<~0.5 V in *I-V* curves under sample illumination.

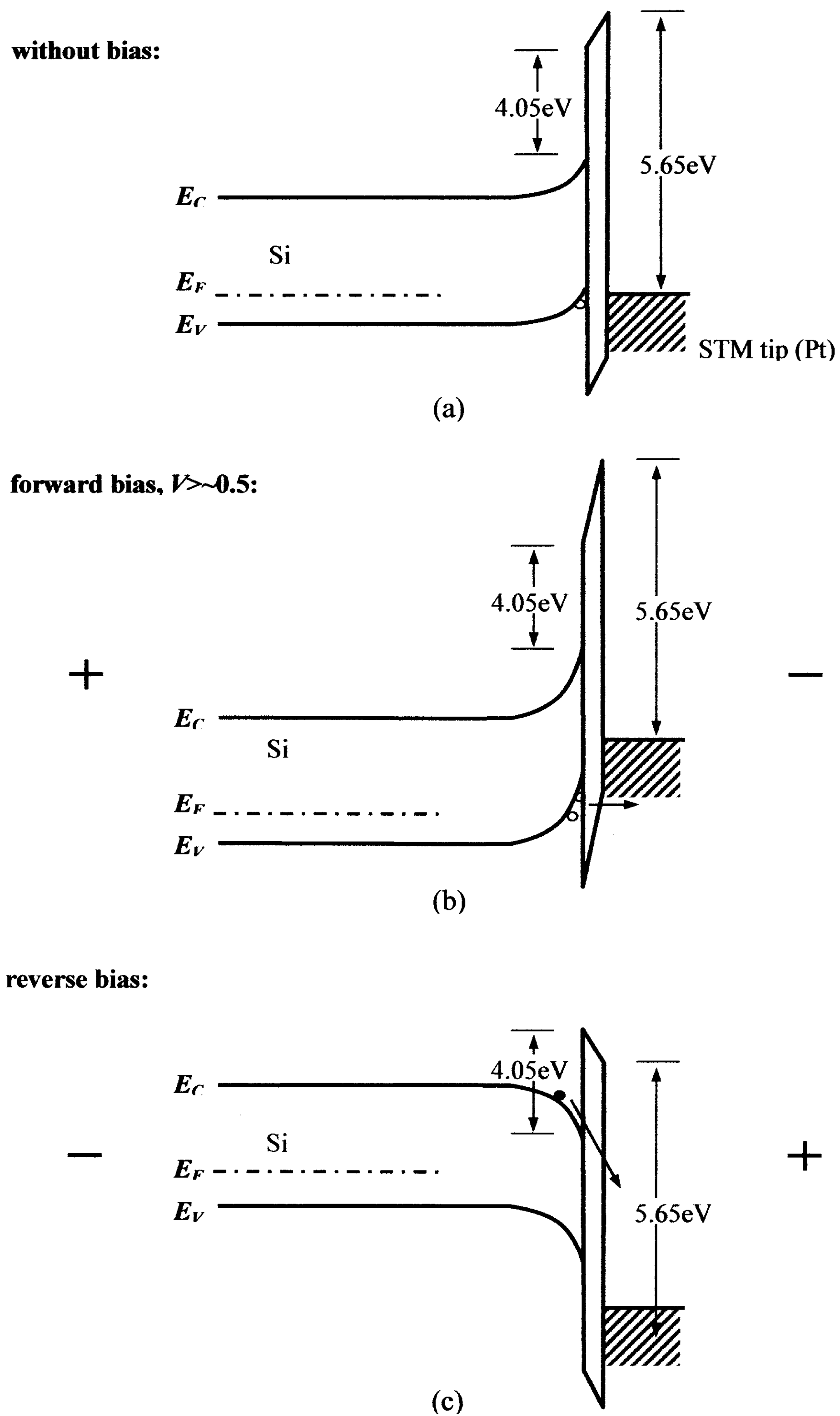

Figure 4.11 Schematic energy band diagram of the sample structure when the tip is placed between the SiGe clusters vertical stacks for different bias conditions: (a) without bias, (b) forward bias and (c) reverse bias.

Next, in order to explain how the series of conductance peaks arise when the tip is located on the vertical stack of SiGe clusters, a schematic energy band diagram shown in Fig. 4.12 is considered. Here, the Si/SiGe clusters SL can be modeled using type-II energy band alignment and most of band discontinuity exists in the valence band. In the schematic energy band diagram, the trapped holes in SiGe clusters valence band reduce the energy band bending in the SL layer due to the suspected charging effect. When this is the case, more of the applied bias is accommodated by the vacuum gap between the tip and the sample surface. In this condition, under positive sample bias, the electron transport should overcome increased conduction barrier height, and also the hole transport from the sample to the tip should be limited by hole trapping in the valence band in SiGe clusters. As a result, the current at positive sample bias significantly reduces compared to that observed when the tip is located between the cluster stacks. The slow increase of positive bias current with increasing bias is attributed to the suspected carrier leakage around SiGe clusters, which is not considered in the diagram.

On the other hand, when negative bias is applied to the sample, the electron transport becomes dominant over a nominal Schottky barrier while holes are still trapped in SiGe clusters. As can be seen in Fig. 4.10a, the on-set voltages of reverse bias current decreases with increasing excitation intensity, which is explained by reduced energy band bending due to the increased trapped charges in the clusters. Note that these are not found in *I-V* curves of Fig. 4.9a which corresponds to the experimental condition that the tip is between the cluster stacks.

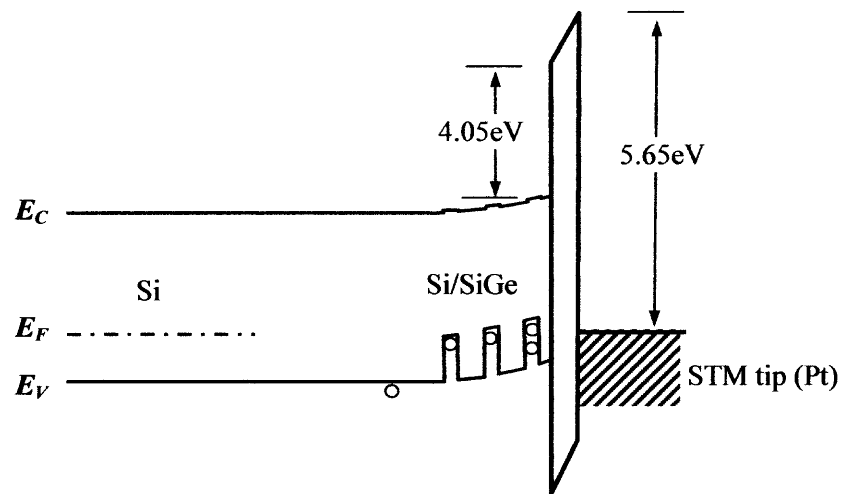

Figure 4.12 Schematic energy band diagram of the sample structure (without bias) when the tip is placed on the SiGe clusters vertical stacks.

Then, the question concerned with the observation of the series of conductance peaks with increasing negative bias can be addressed now. As pointed out previously, both Si and Ge are indirect band gap semiconductors with conduction-band minima located in different crystallographic directions: <111> in Ge and <100> in Si. The SiGe clusters in the sample have ~55 % Ge content, and X-ray reflection and Raman measurements have indicated that samples had chemically abrupt interfaces [67, 81]. Hence, for the electron transport through a channel composed of alternating Si layers and SiGe clusters, even though there are weak energy barriers for electrons (conduction band discontinuities are negligible), emission or absorption of a phonon at the interface is required in order to satisfy crystal momentum conservation. Particularly, phonon emission requires a condition that the electron potential energy difference between the conduction band valley minima in Si and SiGe clusters matches the phonon energy for

the inter-valley scattering. This indicates that the energy band at every period of SL should be aligned such that there is minimum voltage drop matching phonon energy available for electron transfer. Accordingly, as the sample negative bias increases, a high field domain forms at the interfaces until the above condition is met, and this eventually gives rise to electron transport by successive emission of phonons. If this is the case, the conductance peak should appear only once at a certain sample bias which provides the above condition.

Considering the sample structure, however, it is likely that electrons are allowed to drift around the SiGe clusters without such energy band alignment at Si/SiGe clusters interfaces. Thus, as bias voltage increases (i.e., depletion region near the sample surface expands into substrate), when the surface-nearest period reaches the alignment condition, the electrons from the substrate drift around the clusters over the prior 9-period distance, and when arriving at the last period, they drift through the clusters with phonon assistance. Subsequent increase of bias increases the number of the aligned periods, and this gives rise to successive step-like increase in sample current. These processes are schematically shown in Fig. 4.13.

While the observed result can be qualitatively understood, no appropriate quantitative modeling at this point is available to relate a relevant phonon energy in Si or Ge (~36-58 meV) to the observed conductance peak separations; a nonuniform field distribution (vertically and laterally) from the tip to the substrate should be considered in such calculations.

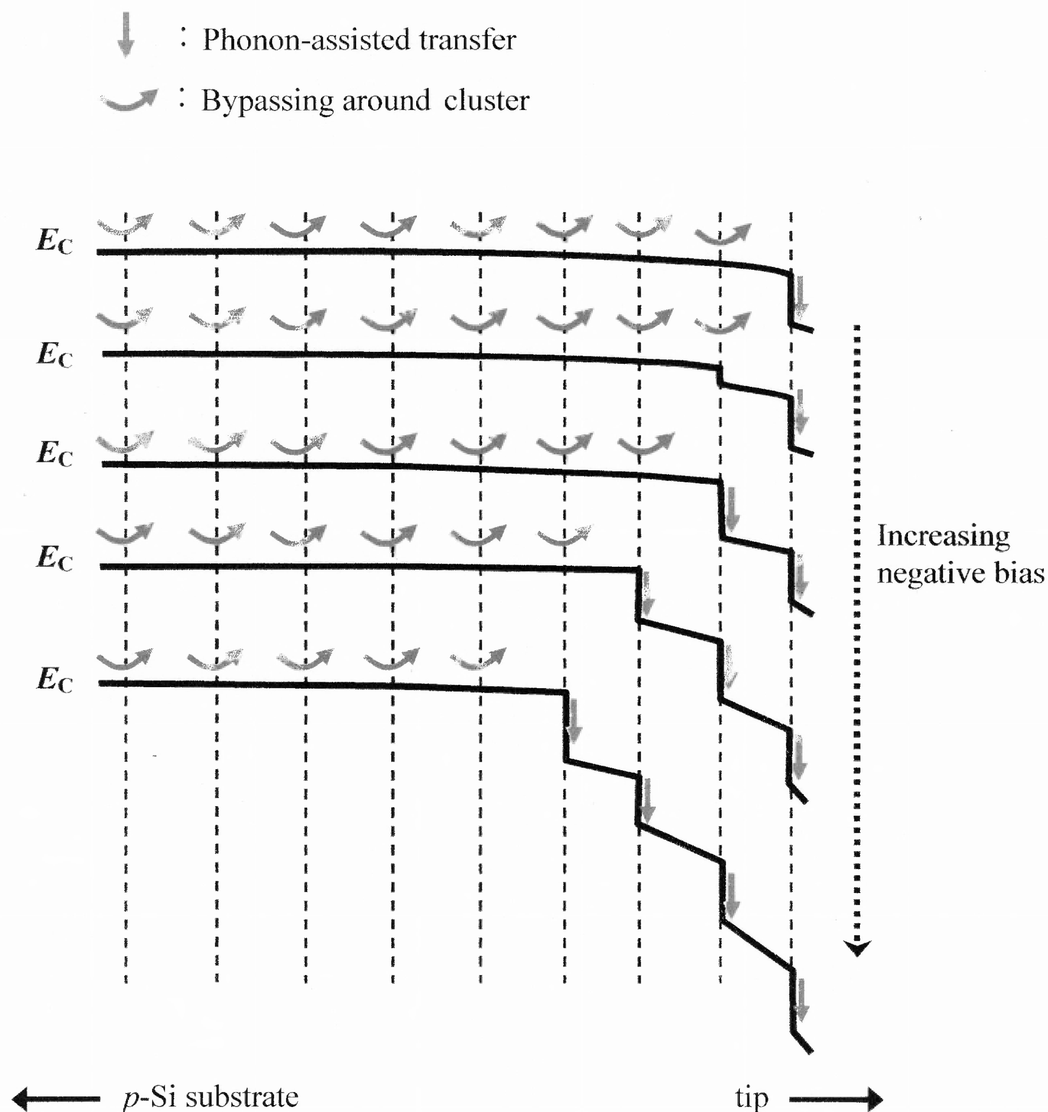

Figure 4.13 Schematic diagram showing variation of conduction energy band in Si/SiGe clusters SL as sample negative bias increases. Dashed lines indicate the heterointerfaces. Conduction band offset at the Si/SiGe interfaces is ignored.

4.2.2 Low Temperature Photoluminescence

PL measurements were carried out on the CVD samples with different Si separating layer thicknesses (7.5, 10 and 20 nm) using Ar^+ laser and a lock-in amplifier. The excitation

intensity was varied over two orders of magnitude from 0.1 to 10 W/cm^2. Sample temperature was varied from 8 to 270 K in a closed-cycle He cryostat. During the measurements, the samples with different Si layer thicknesses exhibited very similar PL spectra at the same experimental condition. Figure 4.14 shows normalized PL spectra measured under different excitation intensities from sample 991 (20 nm Si separating layers).

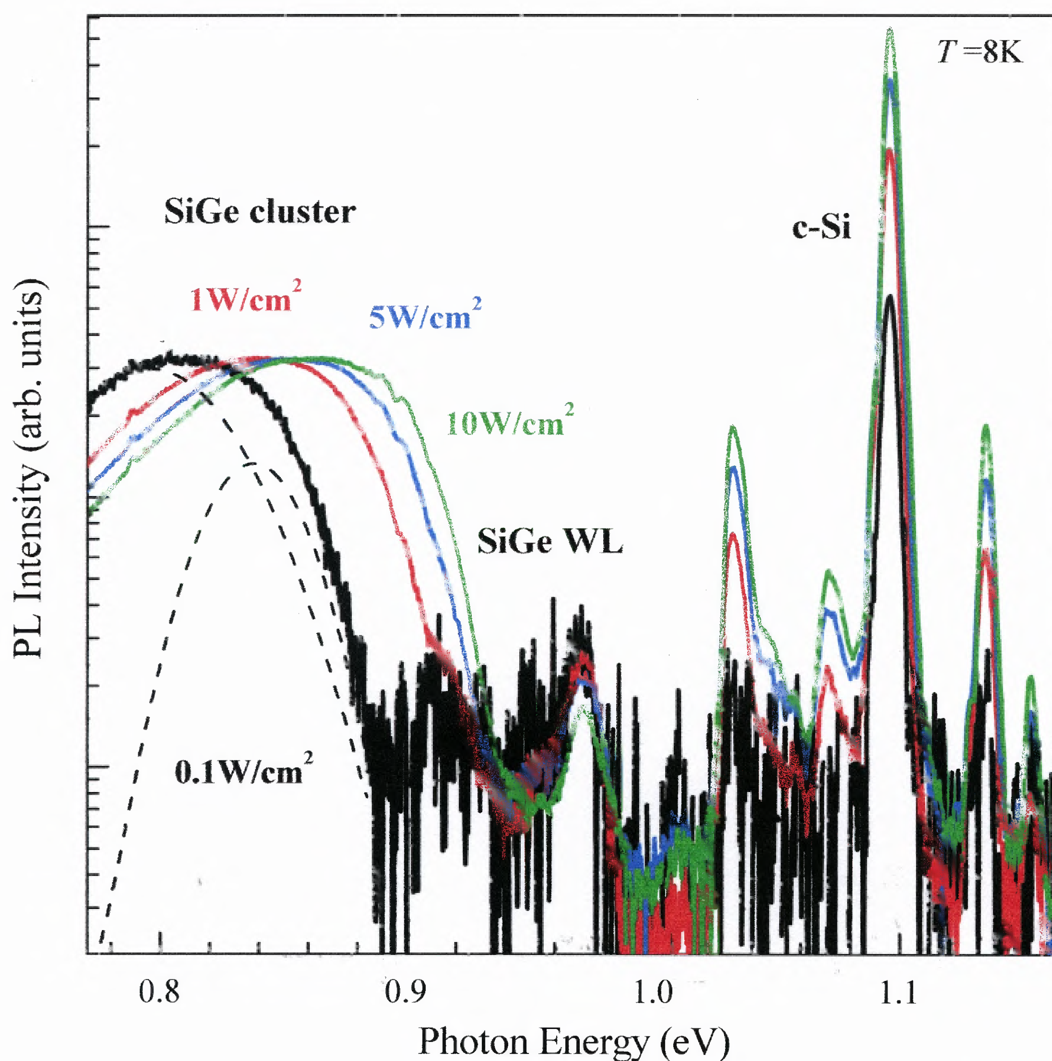

Figure 4.14 Low temperature (T=8 K) normalized PL spectra measured at different excitation intensities. SiGe clusters PL at 0.1 W/cm^2 excitation is fitted with two Gaussian curves (thin dashed lines). Note vertical logarithmic scale.

In the figure, at low excitation intensity, PL attributed to SiGe clusters at low photon energies <0.9 eV, two PL peaks at 0.916 eV and 0.972 eV related to transverse optical (TO) phonon and no-phonon (NP) transitions in SiGe WL and crystalline Si PL above photon energy 1.0 eV are observed. In addition, as the PL excitation intensity increases, PL spectra associated with SiGe clusters continuously shift toward higher photon energies (i.e., blue shift).

The PL spectra at photon energies <0.9 eV are well-fitted by two Gaussian peaks as shown in Fig. 4.14 for the PL spectrum at 0.1 W/cm^2 excitation. Figure 4.15 presents the dependence of these two PL peak energies and their full width at half maximum (FWHM) as a function of excitation intensities. For all the measured PL spectra at different excitation intensities, the two PL peaks at phonon energies <0.9 eV are found to be separated by ~43 meV with FWHM values of ~78 and 47 meV. These two PL peaks are attributed to NP transition and TO phonon replica in the SiGe clusters, respectively [60, 82, 83]. The separation energy of ~43 meV is close to the phonon energy of TO_{SiGe} [53].

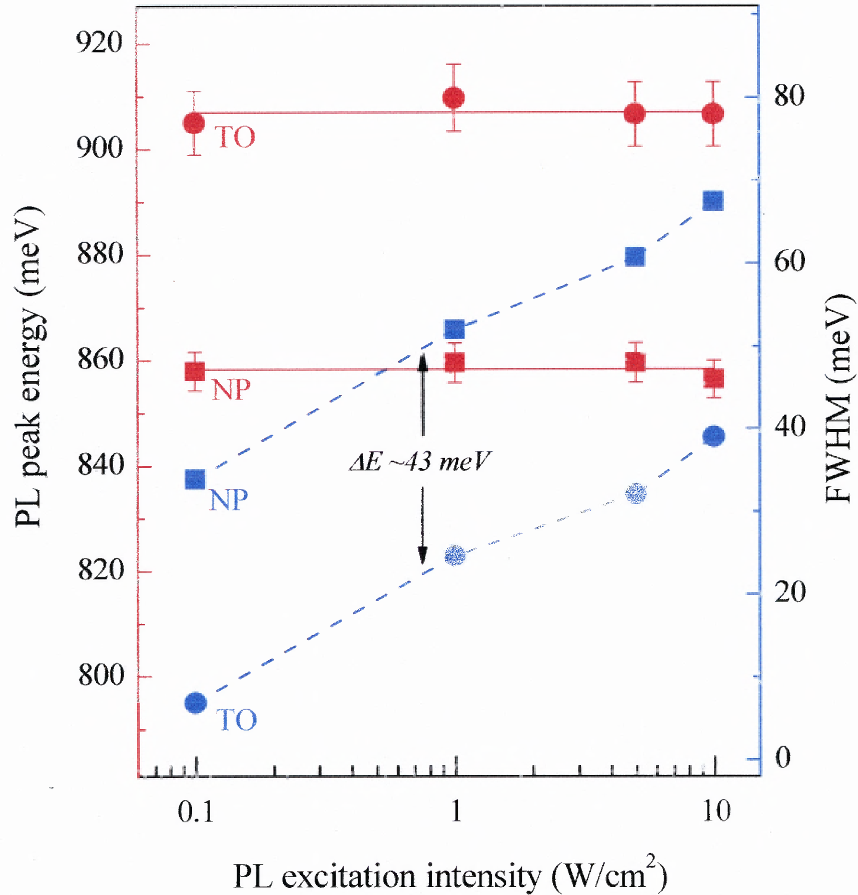

Figure 4.15 Peak positions and FWHM of the two fitting curves with increasing PL excitation intensity.

4.2.3 Photoluminescence Temperature Dependence

Figure 4.16 shows PL spectra measured at temperatures from 8 to 210 K under excitation intensity of 5 W/cm^2. As sample temperature increases, the PL from SiGe WLs disappears at temperatures higher than ~50 K, while the PL from SiGe clusters is clearly observed at temperatures up to 210 K. The PL spectra attributed to SiGe clusters show redshift with increasing temperature, which correlates with the temperature dependence of band gaps in Si and Ge [84].

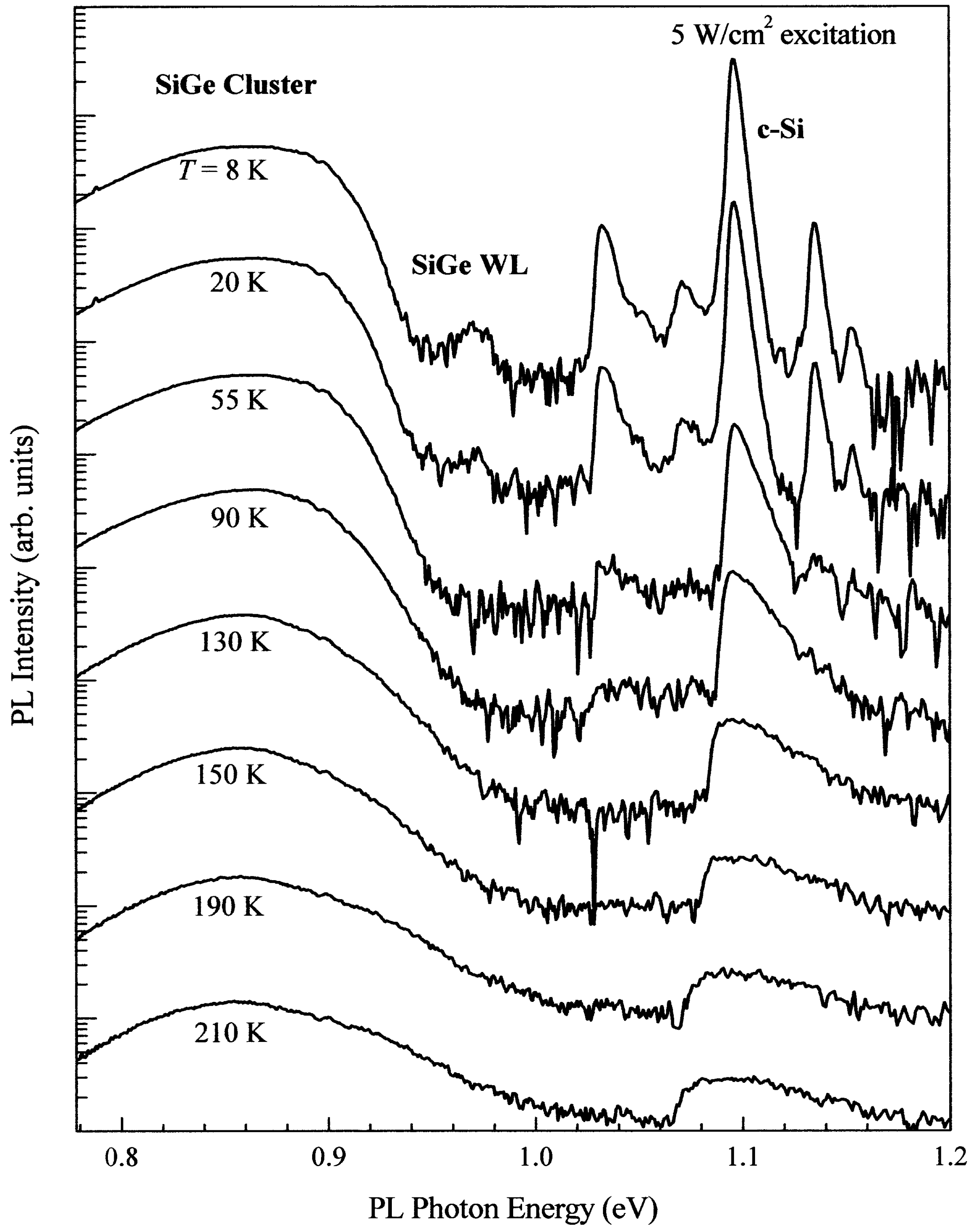

Figure 4.16 PL spectra measured between T=8 and 210 K at 5 W/cm^2 laser excitation. The spectra are shown on a logarithmic scale and vertically shifted for clarity.

The temperature dependences of the integrated PL intensity from SiGe clusters were measured at different excitation intensities (~0.1-10 W/cm^2). Within the range of the used excitation intensities, since the PL peak separation energies and their FWHM remain the same, the integrated PL intensities measured at different excitation intensities can be directly compared.

Figure 4.17 shows a modified (note double logarithmic scale) Arrhenius plot of the normalized integrated PL intensity of the SiGe clusters at the different excitation intensities. The PL intensity at the lowest used excitation intensity (0.1 W/cm^2) is well described by a standard equation $I_{PL}(T) = 1/[1 + C_1 \exp(-E_1/kT) + C_2 \exp(-E_2/kT)]$ (for example, see ref. 81) with two thermal quenching activation energies of E_1~15 meV and E_2~120 meV.

However, at higher excitation intensities, the PL intensity temperature dependence once deviates from the preceding exponential roll-off path with increasing sample temperature, eventually showing drastic decrease. Such behavior is found to be most pronounced under the highest excitation intensity used. Fitting of experimental data (performed separately for the temperature ranges above ~150 K or below ~150 K) at the highest excitation intensity (10 W/cm^2) reveals thermal activation energies of E_1~15 and E_2~150 meV for T<150 K and ~340 meV for T>150 K.

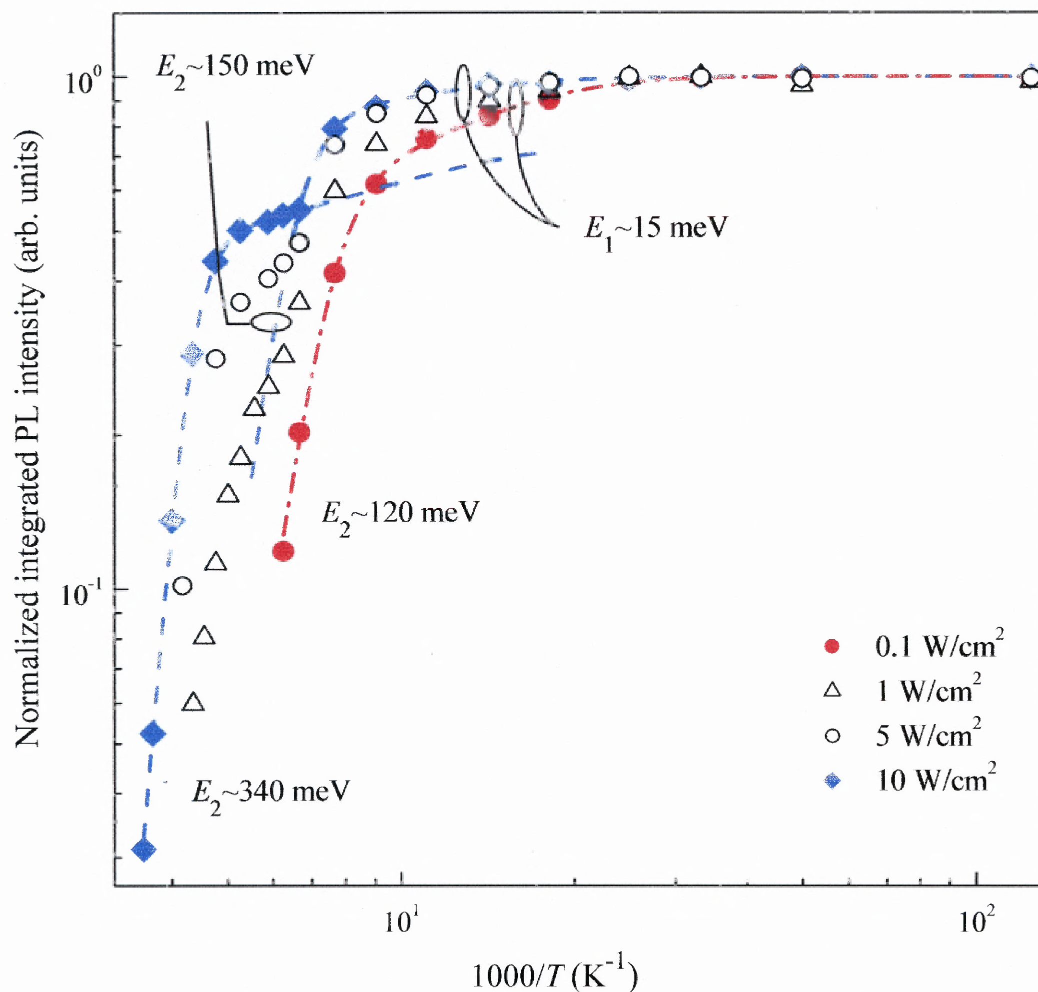

Figure 4.17 SiGe clusters integrated PL intensity temperature dependence for various excitation intensities and fitting curves with two (indicated) thermal quenching activation energies. Dashed lines are extension of the fitting curves beyond the fitted data range. Note logarithmic scale along vertical and horizontal axes.

Figure 4.18 compares PL quenching behavior found in samples with different Si separating layer thicknesses. In the sample with 7.5 nm Si layer (sample 1078), the same excitation-independent PL thermal quenching activation energy E_1~15 meV is found at low temperatures, and E_2 at high temperatures increases from ~60 to 70 meV as excitation intensity increases.

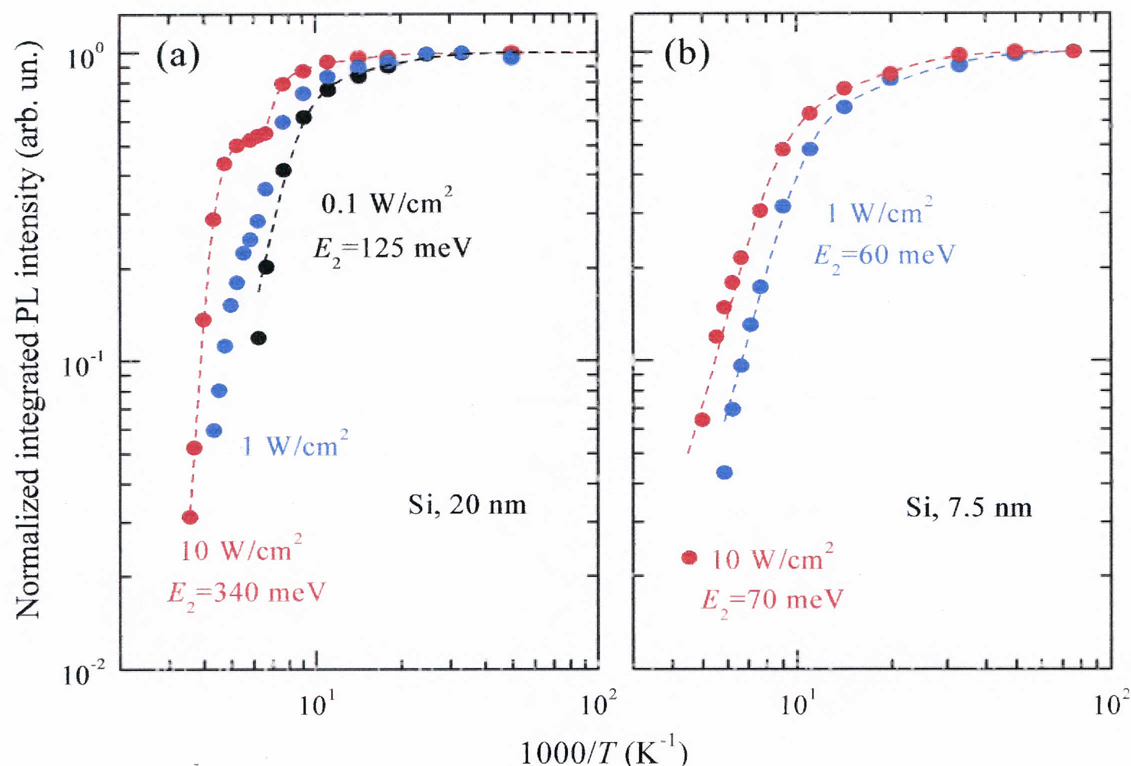

Figure 4.18 Temperature dependence of SiGe clusters integrated PL intensity measured from samples with (a) 20 nm and (b) 7.5 nm thick Si separating layers at different excitation intensities. The dash lines show fittings using two thermal quenching activation energies. The values of E_2 are shown.

Figure 4.19 shows the PL intensity temperature dependence measured repeatedly by heating or cooling the sample continuously. The measurement started with sample heating from T=8 K after cooling the sample in the dark (without photoexcitation). During the first cycle (heating and cooling under photoexcitation), PL intensity thermal hysteresis was found. This PL intensity hysteresis as a function of temperature disappears after a complete heating/cooling cycle; however, under the same excitation intensity, the PL thermal quenching activation energy does not change. This effect is less pronounced in the sample with 7.5 nm Si layers.

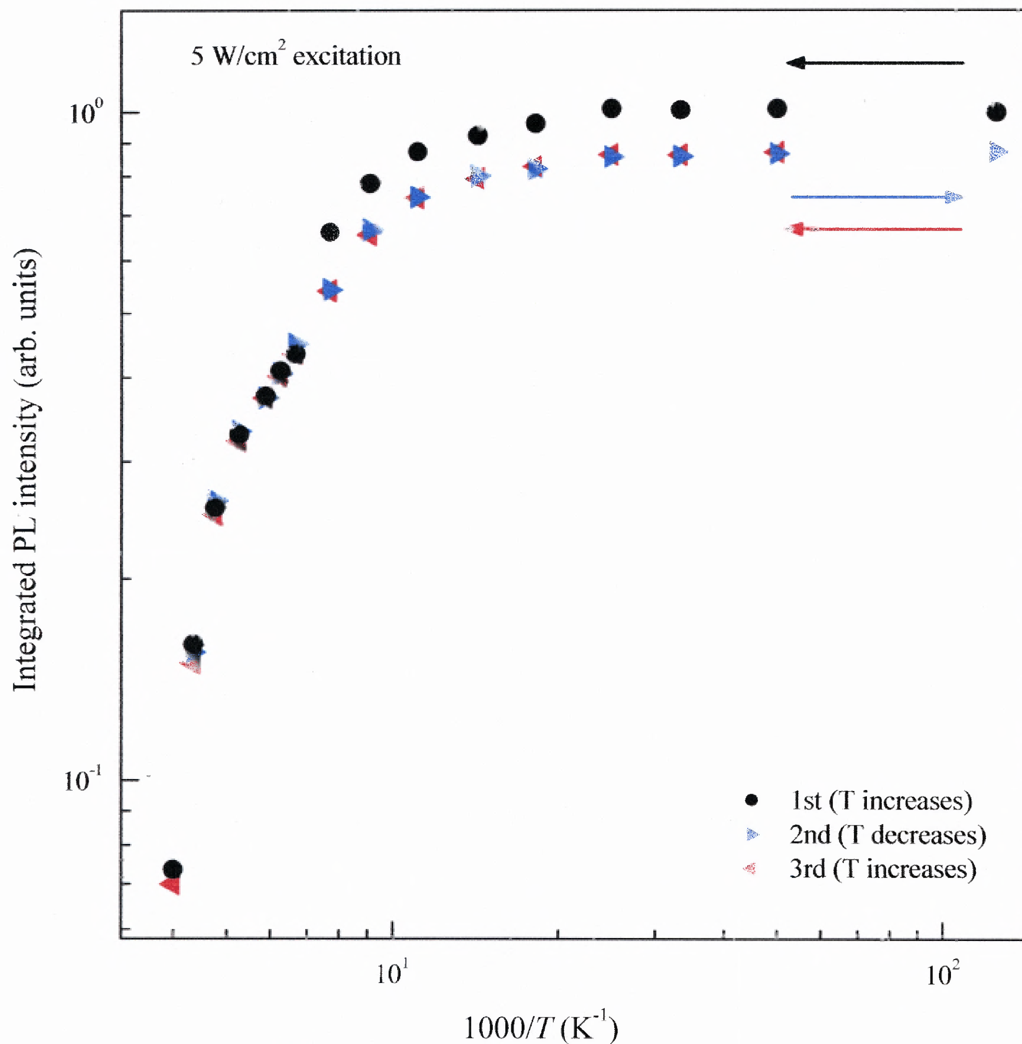

Figure 4.19 The integrated PL intensity in the samples with 20 nm thick Si separating layers measured during the heating/cooling cycles under an excitation intensity of 5 W/cm^2.

4.2.4 Photoluminescence Thermal Quenching in Si/SiGe Clusters Superlattices

It has been known that Si/SiGe pyramid-like clusters can be modeled as nanostructures with type II energy band alignment in the direction of growth and possible SiGe valence band energy quantization [60, 85]. In this model, since electrons and holes are localized

in different regions, carrier recombination via such spatially indirect transition require a longer time. In addition, the PL intensity saturation should be more pronounced at lower PL photon energies because stronger confinement provides weaker electron-hole wave function overlap, and this, at least in part, might contribute to the observed blue shift of the PL peak as excitation intensity increases.

The observed excitation-independent PL thermal quenching activation energy of ~15 meV is close to the exciton binding energy in fluctuations of SiGe alloy composition [53, 86, 87]. Therefore, it is concluded that one of the mechanisms of PL thermal quenching is thermal dissociation of excitons. Besides, electron transport in 3D Si/SiGe clusters SL is limited by a small (~10-15 meV) conduction band energy barrier. Thus, the found PL thermal quenching activation energy of ~15 meV could also be associated with electron diffusion in Si/SiGe clusters SL. In contrast, hole diffusion is controlled by large valence band energy barriers at Si/SiGe heterointerfaces. Two major mechanisms of hole transport can be considered: (i) hole tunneling and (ii) hole thermionic emission. Hole tunneling in 3D Si/SiGe nanostructures with thin (5–7 nm) Si separating layers and nearly perfect SiGe clusters vertical self-alignment could be very efficient [88, 89]. These nanostructures are mostly grown by molecular beam epitaxy and exhibit the PL thermal quenching activation energy of ~60 meV [81]. The same PL thermal quenching activation energy is found in CVD-grown samples with 7.5 nm thick Si separating layers at the lowest used excitation intensity. It is suggested that in Si/SiGe clusters SL with thin Si layers at low excitation intensity, electron-hole separation and nonradiative carrier recombination are mainly controlled by hole tunneling between SiGe clusters. Due to significant variations in SiGe clusters size, shape, and chemical composition, the process

of hole tunneling could be assisted by phonon emission and/or absorption [90]. Therefore, the found PL thermal quenching activation energy is close to the Si TO phonon energy. In the sample with 20 nm thick Si layers, where SiGe clusters vertical self-alignment is practically absent, probability of hole tunneling is reduced, and hole thermionic emission over the Si/SiGe heterointerface barrier is playing a bigger role; SiGe clusters vertical self-alignment is known to disappear as Si layers thickness increases above ~10 nm [52]. Thus, in this sample the PL thermal quenching activation energy is expected to be greater, and it has been found in the experiments. In this simple model, an efficient hole tunneling between adjacent SiGe nanoclusters requires not only reasonably low and thin energy barriers but also a low carrier concentration (i.e., enough number of empty adjacent SiGe clusters). By increasing photoexcitation (i.e., number of photogenerated carriers), hole tunneling can effectively be suppressed since fewer empty adjacent SiGe clusters can be found. At high excitation intensity, assuming (i) a negligible value of the conduction band offset compared to that in valence band and (ii) nearly pure Ge composition in SiGe clusters core [91], the maximum anticipated PL thermal quenching activation energy should be $E_2 \leq E_{g\text{-}Si} - E_{g\text{-}Ge} \leq 400$ meV. This value sets the upper limit in the activation energy of PL intensity thermal quenching in 3D SiGe multilayer nanostructures, and it is close to the activation energy of $E_2 \sim 340$ meV which has been found under the highest used excitation intensity.

The observed hysteresis in the PL intensity as a function of temperature can also be explained under the same assumption. This effect is found to be stronger in the samples with thicker Si separating layers and it suggests an important role of a nonuniform in-depth absorption of light due to $>10^5$ cm^{-1} absorption coefficient at photon

energies >2.5 eV. In our experiment, the samples are cooled down to T=8 K without photoexcitation (i.e., in the dark), and then they are exposed to the strongly absorbed laser light. At a low temperature and high photoexcitation, a large and nonuniform in-depth carrier concentration is created. By charging SiGe nanoclusters, vertical hole tunneling is effectively suppressed because of the decreased number of empty clusters involved in the tunneling process. This effect is similar to the "optical memory" effect in SiGe clusters and quantum dots and it increases the PL intensity at low temperature. To remove the "frozen" hole distribution, a higher temperature is required and the effect can be erased by performing a complete cycle of heating and cooling under continuous illumination.

4.2.5 Electroluminescence

EL measurements were performed on the sample 991 with metal contacts in the temperature range from 30 to 150 K under relatively low value of negative bias voltages ranging from -2.5 to -7 V. The sample was prepared with a simple Schottky barrier type structure as is described in chapter 3. The sample I-V curves at T=30 K current exhibited clear rectifying behavior with forward bias characteristics under sample negative bias, and practically no EL was observed under sample positive bias. The measured EL spectra are shown in Fig 4.20.

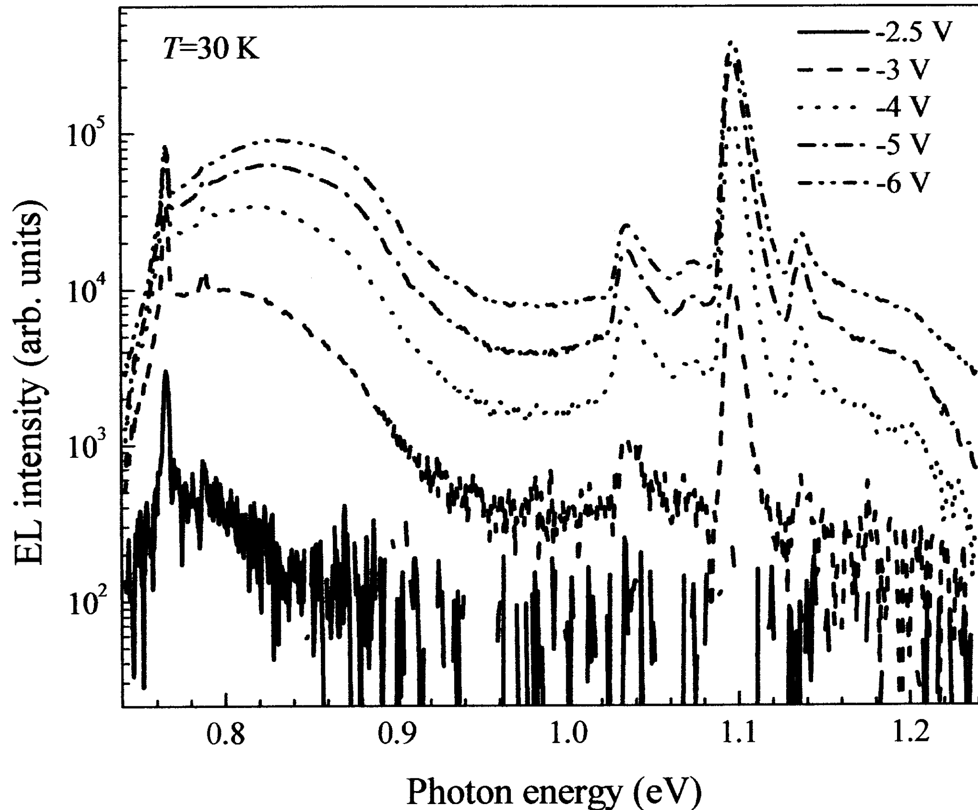

Figure 4.20 Low temperature (*T*=30 K) EL spectra at different sample bias.

The EL spectra due to the SiGe clusters are broad with an asymmetric spectral shape similar to the PL spectra, and they can be well fitted by two Gaussian bands separated by ~45 meV (Fig. 4.21). This energy is close to characteristic optical phonon energy in SiGe, proving that the EL mechanism is nearly identical to that of the PL. The integrate EL intensity is nearly linear as a function of the applied voltage (Fig. 4.22). The EL intensity as a function of temperature is also similar to that found in PL, and the EL thermal quench activation is ~130 meV (Fig. 4.23a). The sample current as a function of temperatures shows clear anti-correlation with the EL intensity and exhibits activation energy of ~140 meV (Fig. 4.23b).

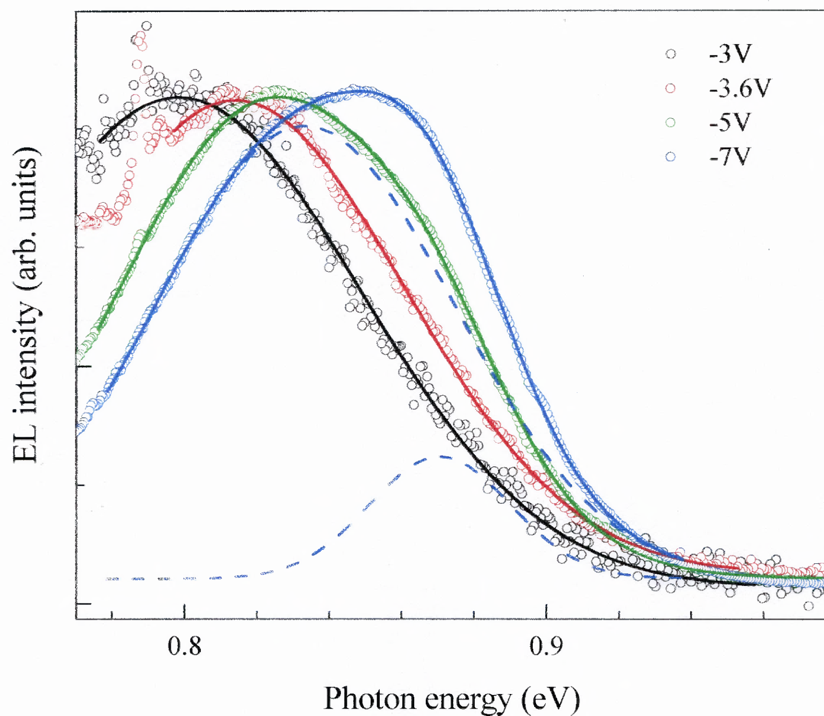

Figure 4.21 Normalized EL spectra originating from SiGe clusters at different sample bias. Solid lines are fitting curves which are deconvoluted into two symmetric Gaussian curves (dashed lines).

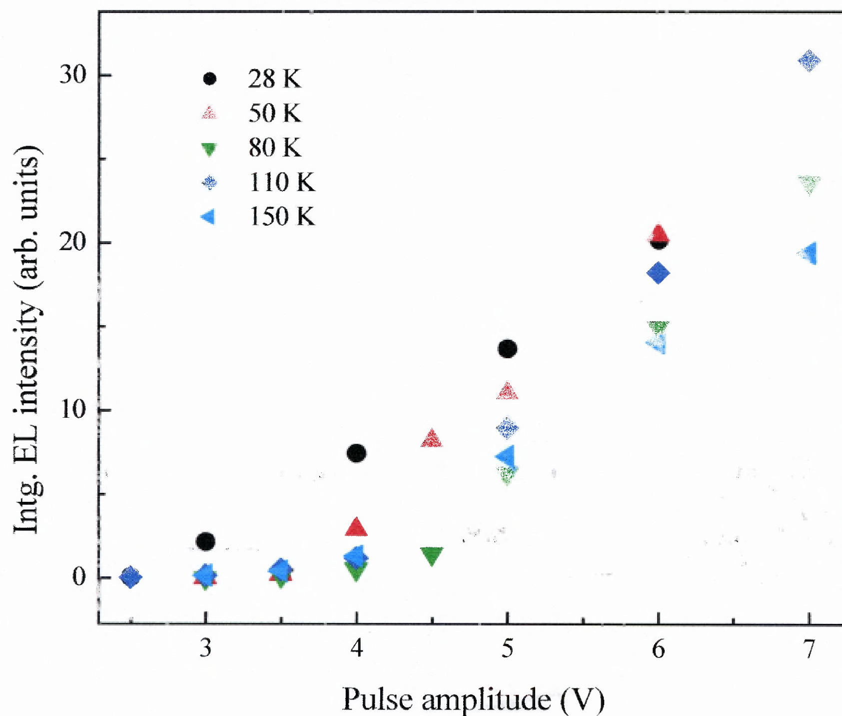

Figure 4.22 Integrated EL intensity as a function of the pulsed voltage amplitude measured at indicated temperatures.

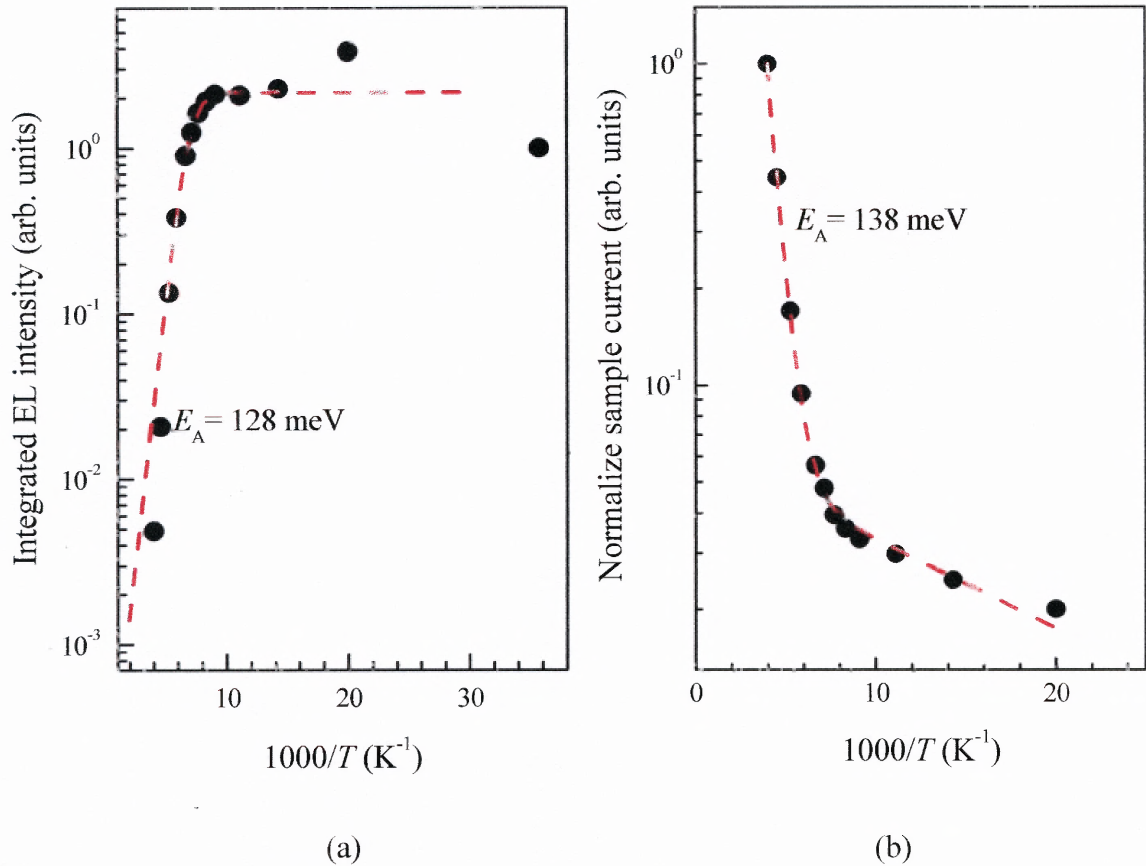

Figure 4.23 (a) Sample current and (b) EL intensity as a function of the reciprocal temperatures at V=-5 V. The thermal activation energies form fits are also shown.

4.2.6 Photoluminescence under high intensity excitation

Understanding of high density carrier dynamics in semiconductor nanostructures is a prerequisite for applications in light-emitting devices. An MBE grown sample (sample 1831) was investigated temporally and spectrally on PL at high excitation intensities using 6 ns pulse duration Q-switched Nd:YAG laser with pulse energies of ~0.1-10 mJ/cm^2 as well as at low excitation using Ar$^+$ cw laser with excitation intensities of ~0.01-10 W/cm^2.

For PL measurements under a pulsed laser excitation, second harmonic of the

Nd:YAG laser was used with 532 nm excitation wavelength and a repetition frequency of 10 Hz. The signal has been averaged using a LeCroy digital storage oscilloscope. The overall time resolution of the system was ~3 ns.

Figure 4.24 shows low temperature (T=15 K) PL spectra measured using cw Ar^+ laser excitation under different excitation intensities. The PL associated with carrier radiative recombination in SiGe clusters exhibits evolution of multiple (more than two) PL peaks as excitation intensity increases, which is most likely related to the achieved better control over composition and size distribution of SiGe clusters during the sample MBE growth compared to those in the CVD samples. The SiGe clusters PL intensity is found comparable to that of the Si PL at 1.096 eV.

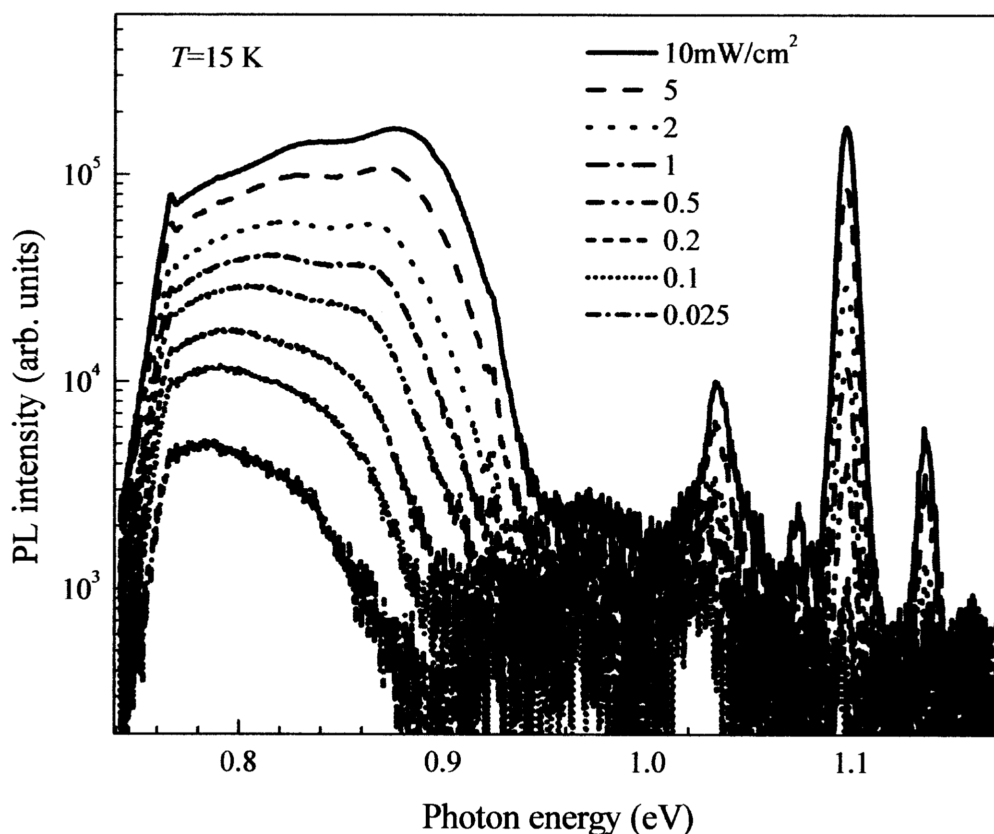

Figure 4.24 Low temperature (T=15 K) PL spectra of sample 1831 measured at different excitation intensities.

At higher excitation intensities (above 5 kW/cm^2), measured under pulse excitation, the SiGe clusters PL is observed to quench or saturate quickly with increasing excitation intensity as shown in Fig. 4.25. In addition, the SiGe PL is found only at photon energies below ~0.9 eV. On the other hand, at 1.079 eV near Si FE PL peak (TO phonon involved peak), a broad PL peak is found, which is luminescence due to a condensed phase of electron and hole carriers known as electron-hole droplet (EHD) in Si [92, 93]; the much smaller new peaks observed at ~1.02 and 1.12 eV are other phonon (TA and TO+O$^{\Gamma}$) replicas.

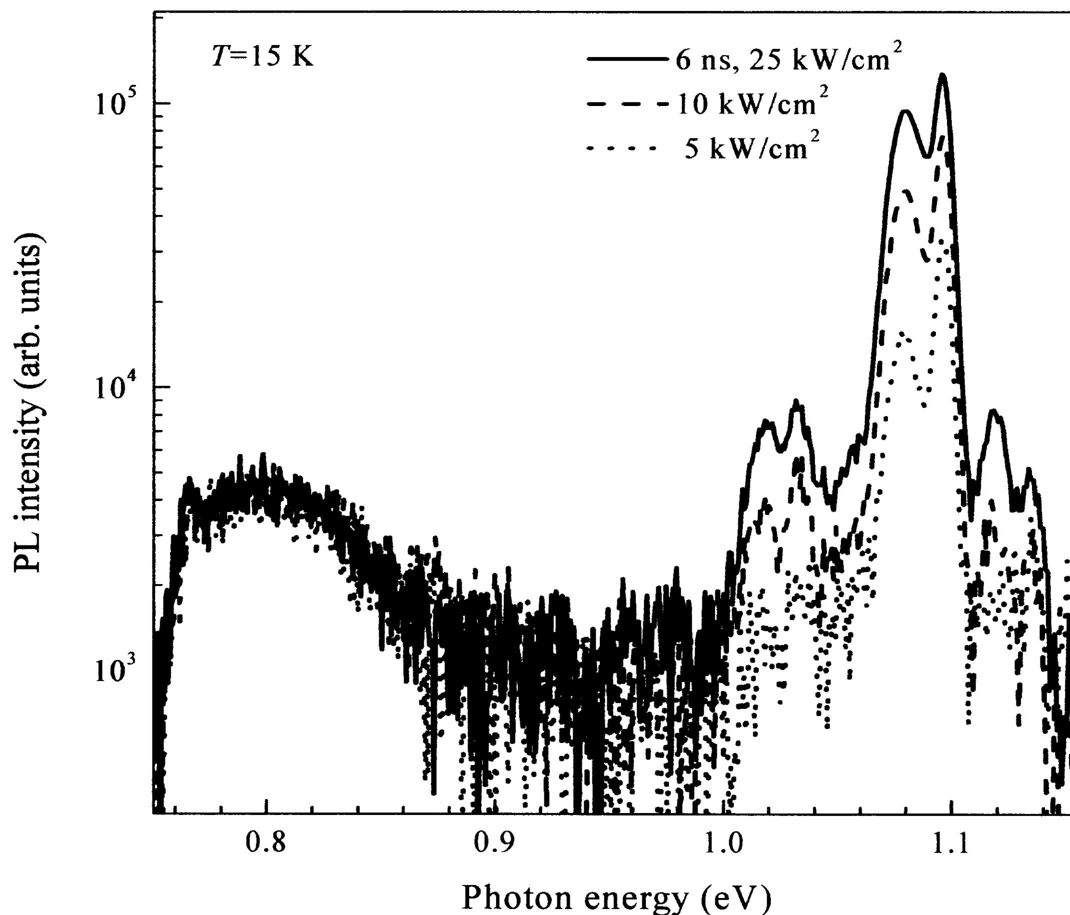

Figure 4.25 Low temperature (T=15 K) PL spectra measured at different excitation intensities using Nd:YAG Q-switched pulse laser.

Figure 4.26 shows PL spectra in the Si PL spectral range collected under pulse excitation intensities of ~0.01-1 MW/cm^2 (or energy density ~0.1-10 mJ/cm^2). The broad PL at the lower photon energy side of the FE PL peak grows quickly and slightly shifts to higher photon energies with increasing excitation intensity due to increased participation of electron-hole plasma (EHP) in recombination process with possible sample heating. The FE PL peak intensity increases near linearly with power n~1.2 and the EHD peak intensity show a superlinear dependence with n~1.8.

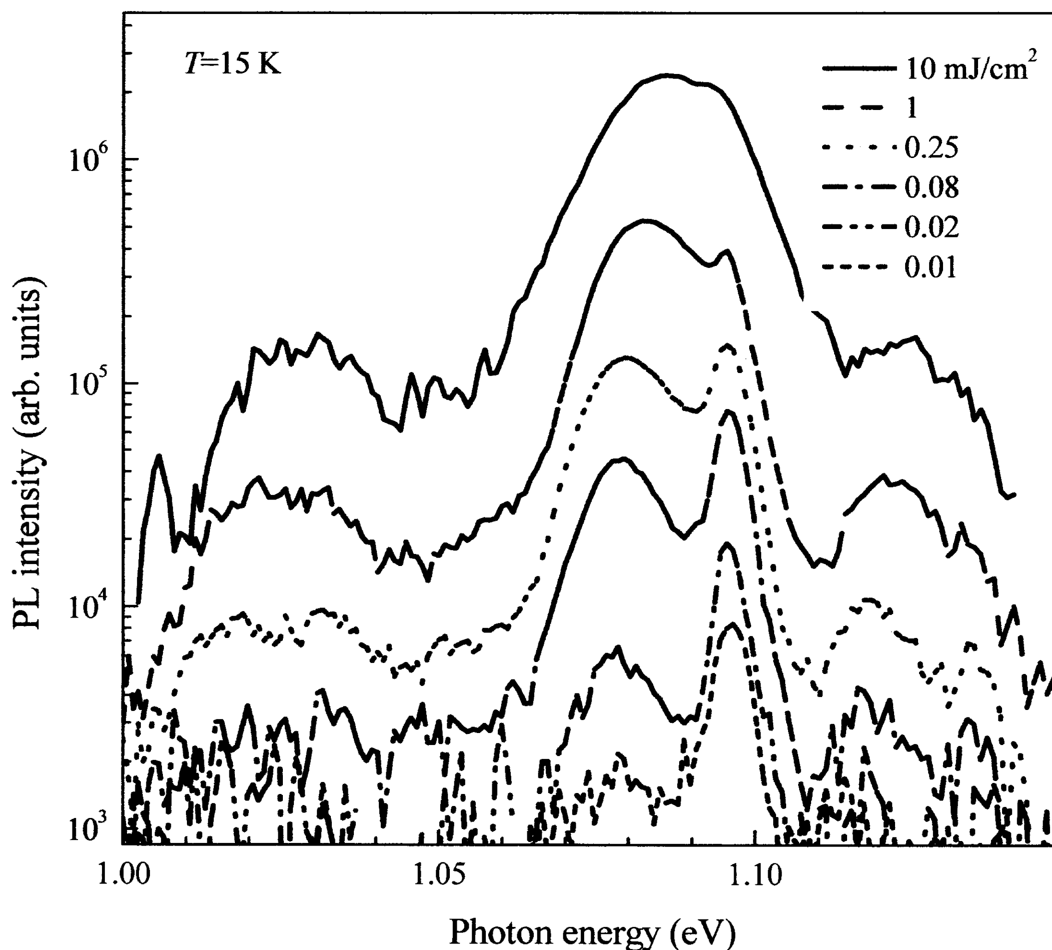

Figure 4.26 Low temperature (T=15 K) PL spectra measured in Si-related spectral region at different excitation intensity using Nd:YAG Q-switched pulse laser.

Figure 4.27 shows excitation dependence of normalized PL transients from the SiGe clusters (at 0.873 eV) and the EHDs (at 1.079 eV) measured under different pulse energy densities of ~0.1-10 mJ/cm^2; during the measurement, the PL due to SiGe clusters at photon energies ranging from ~0.75 to 0.9 eV revealed similar temporal behaviors under the same excitation intensity. The SiGe clusters PL shows fast decay component immediately after pulse excitation, which becomes faster with increasing excitation intensity, and at the later times, it decays very slow with lifetime of ~10^{-4}-10^{-2} s. In addition, an unusual SiGe PL behavior is found at the highest excitation intensity of 10 mJ/cm^2: the initial fast decay is followed by first rising and then decaying PL component (Fig. 4.27a). Contrarily, the PL from EHDs shows a rise time of ~100 ns, and at the highest excitation, the PL Si EHD PL decays initially slow with lifetime of ~200 ns and a very fast decay component with lifetime of ≤20 ns follows later. Under lower excitations, the initial slow EHD PL components gradually disappear and decay near exponentially with characteristic lifetime $\tau_{EHD} \geq 50$ ns. These clear anti-correlations between the PL dynamics at 0.873 eV and 1.079 eV indicates that the observed Si EHD PL mostly originates within thin Si layers separating SiGe clusters rather than the Si substrate.

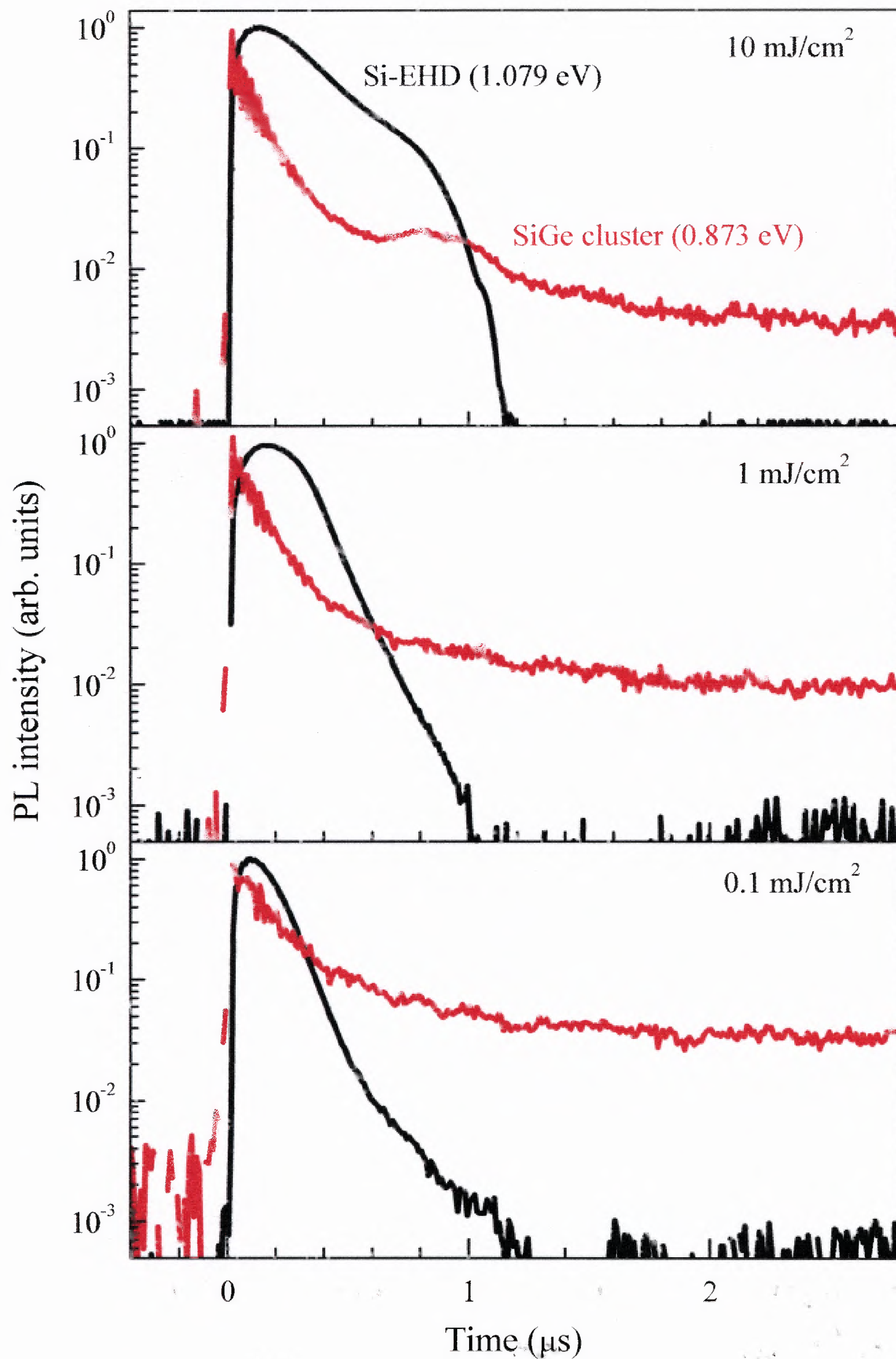

Figure 4.27 PL dynamics under different (indicated) pulsed laser energy densities recorded at photon energies associated with SiGe PL (~ 0.873 eV) and Si EHD PL (~ 1.079 eV). Note vertical logarithmic scale.

Figure 4.28 shows the temperature dependence of PL intensity measured at 1.079 eV. At low excitation of ~100μJ/cm^2, the PL intensity decreases exponentially while at the highest excitation intensity of 10 mJ/cm^2 it is roughly temperature independent up to T=270 K.

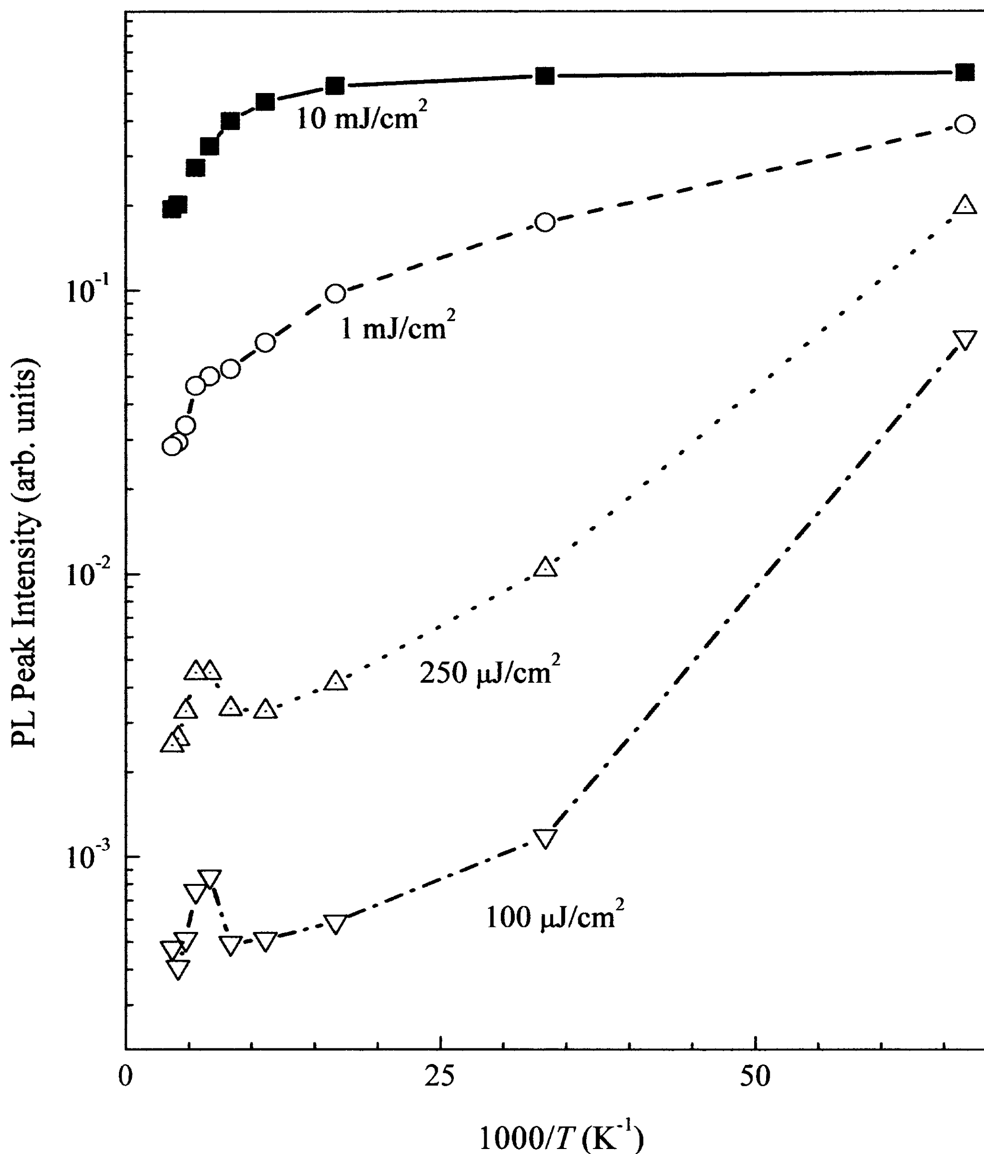

Figure 4.28 PL peak intensities as functions of reciprocal temperature measured at different (indicated) excitation energy densities.

4.2.8 Electron-Hole Condensate and Carrier Relaxation in Si/SiGe Cluster Superlattice

The experimental results can be explained using type-II energy band alignment at Si/SiGe clusters interface. At low excitation intensities, electrons localized in Si layers mostly recombine radiatively with holes confined in valence band of SiGe clusters near Si/SiGe interface (Fig. 4.29a). This recombination process exhibits a long radiative lifetime ranging from 10^{-4} to 10^{-2} s since electrons and holes are spatially separated at the type-II interface [81]. With increasing excitation intensity, accelerated Auger process with much shorter recombination lifetime $\leq$20 ns dominates the recombination process. It has been known that Auger rate in Si/SiGe QW with thickness of several nanometers increases by ~100 times compared to that in bulk Si and Ge [94]. At the same time, this process involving one electron and two holes at each event generates 'Auger holes' with energies of 0.7-0.8 eV, which are redistributed into Si layers during thermalization (Fig. 4.29b). This Auger hole ejection from SiGe clusters into Si barriers results in accumulation of both electrons and holes within the nanometer-thick Si layers. This mechanism is qualitatively similar to the previously reported "Auger fountain" in III-V heterostructures with type II energy band alignment [95]. Subsequently, the high excess carrier concentration in Si layers results in electron-hole condensation (i.e., EHD) which has recombination lifetime$\geq$50 ns. Due to the carrier recombination and accompanying evaporation processes in EHDs, the EHDs undergo first-order transition into gas phase electron and holes, which occurs in smaller droplets below a critical size. Successively, the released holes can be recaptured into SiGe clusters valence band (Fig. 4.29c), which accounts for the observed SiGe PL rising component at later times after pulse excitation.

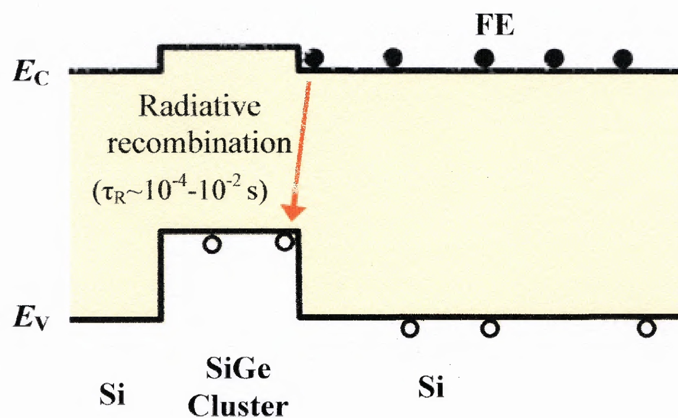

(a)

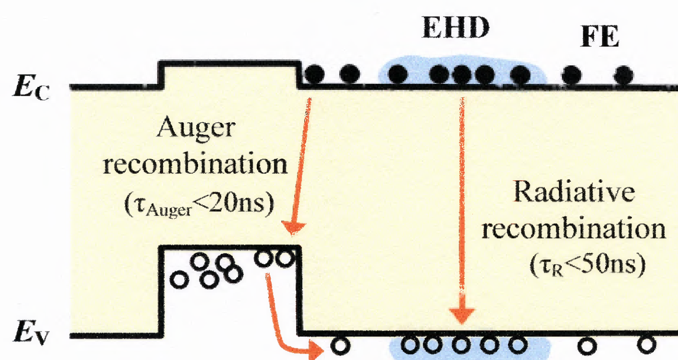

(b)

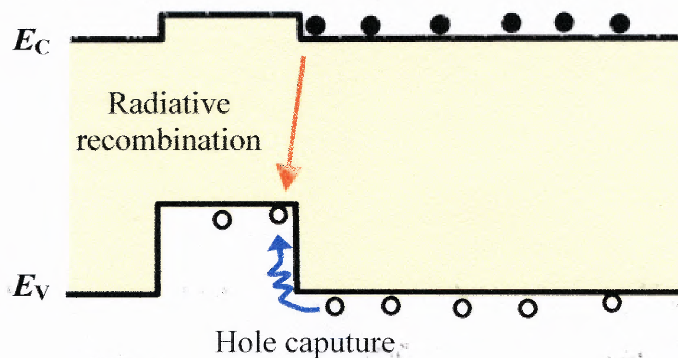

(c)

Figure 4.29 Schematic representation of different recombination processes in Si/SiGe 3D nanostructures with a type II energy band alignment at Si/SiGe heterointerface (a) at low excess carrier concentration, (b) at high excess carrier concentration and (c) During ~0.1- 1 μs after the laser pulse.

In bulk Si, when excess carrier concentration approaches near density-of-states (DOS) ($\sim 10^{-19}$ cm^{-3}), EHDs can be formed directly from hot dense photoexcited EHP [92]. However, in 3D Si/SiGe clusters SL, their formation is controlled by Auger-mediated supply of hot holes. Moreover, the formation seems to be significantly enhanced by a reduction of DOS in thin (~15 nm) and partially strained Si layers and by a suppressed carrier diffusion in the direction of growth due to the layer-by-layer heterostructure of Si and SiGe. The enhanced carrier-carrier and carrier-phonon interaction in EHDs increases local lattice temperature and produces additional non-equilibrium phonons with the energy-momentum dispersion quite different compared to that at thermal equilibrium [96, 97, 98]. The significantly disturbed phonon spectrum contributes to an increase of probability of the phonon-assisted transitions, and recombination lifetime drops down.

The observed EHD PL intensity in the Si/SiGe clusters shows superlinear dependence on the used excitation intensities using pulse energy densities of ~0.01-10mJ/cm^2. Furthermore, this fast growing PL intensity reveals short PL lifetime compared to that of FE PL (reportedly, FE radiative recombination time is $\tau_R \sim 10^{-3}$ s in bulk Si) [99]. Since PL intensity is, as a rule, inversely proportional to the radiative lifetime, it is suggested that the experimentally observed fast PL decay ($\tau_{EHD} \sim 50$ ns) is associated with the short EHD radiative recombination.

Auger recombination in bulk Si has a lifetime $\tau_{Auger} = \frac{1}{Cn^2}$, where n is carrier concentration and $C \sim 10^{-31}$-10^{-30} $cm^6 \cdot s^{-1}$ [100]. Therefore, in the Si/SiGe clusters SL, at high carrier concentration enough to form EHDs ($n \sim 10^{18}$-10^{19} cm^{-3}), their radiative recombination (with $\tau_{EHD} \sim 50$ ns) successfully competes with non-radiative Auger process. In addition, at these excitation intensities, carrier diffusion along the nanometer thick Si

layers is strongly suppressed since carrier concentration is comparable to the Si DOS. Thus, high concentration of excess carriers provides both, highly efficient (because of fast transitions) and nearly temperature independent (because of the suppressed diffusion and, possibly, saturation of non-radiative recombination channels) radiative recombination.

CHAPTER 5

CONCLUSION

This dissertation has presented a detailed investigation of optical properties and carrier transport in quasi-one (i.e., Ge NW/Si substrate heterojunction) and three-dimensional (i.e., cluster morphology) Si/SiGe nanostructures. This chapter serves as a summary of the experimental work and original contribution to the field.

5.1 Summary of Conclusions

There are several important results and their contributions about the work conducted for this dissertation, which may be summarized as follows:

- Exponential dependence of conductivity on temperature, current instability and negative differential photoconductivity have been observed in Ge NWs/(100) n^+ Si substrate heterostructures. The proposed explanation is based on an abrupt and defect-free Si/Ge heterointerface. Future work in this direction can be focused on novel device applications such as an RF emitters and thermoelectric devices.

- STM-assisted electrical measurements have been conducted on Si/SiGe clusters nanostructures, and provided vital information explaining critical details in carrier transport mechanism.

- A novel mechanism explaining the observed excitation dependent PL thermal quenching in Si/SiGe clusters nanostructures has been suggested and the presented experimental results show how PL can be extended to near room temperature without significant quantum efficiency thermal quenching.

- 'Auger fountain' has been observed for the first time in Si/SiGe clusters nanostructures and the demonstrated carrier recombination mechanism is found to provide an optimal condition for fast and efficient EHDs luminescence, which successfully competes with non-radiative band-to-band Auger process in nanometer-thick Si layers.

5.2 Final Thoughts

For the last several decades, Si/SiGe heterostructure systems have been intensively studied and eventually used in commercially available electronic devices. Bi-CMOS technology utilizing enhanced mobility in these systems via band structure engineering is already playing a major role in high frequency applications competing with III-V compound semiconductors. At the same time, nowadays, low-dimensional nanostructured Si/SiGe material systems are considered as promising candidates for even more advanced electronic and optoelectronic applications where drastic modification of electrical and optical properties leads to new physical phenomena and hence many novel device concepts.

The experimental results presented in this dissertation provides valuable insight into the use of low-dimensional Si/SiGe nanostructures for electronic and optoelectronic devices as well as several promising practical achievements. It seems clear that continued theoretical and experimental work aimed at elucidating the observed phenomena in these nanostructures should lead to the development of novel devices with a promise to be eventually monolithically integrated in the CMOS environment.

REFERENCES

1. F. Schaffler, "High-mobility Si and Ge structures", Semiconductor Science and Technology **12** (12), 1515-1549 (1997).

2. T. Takagahara and K. Takeda, "Theory of the quantum confinement effect on excitons in quantum dots of indirect-gap materials", Physical Review B **46** (23), 15578-15581 (1992).

3. G. Gu, M. Burghard, G. T. Kim, G. S. Dusberg, P. W. Chiu, V. Krstic, S. Roth, and W. Q. Han, "Growth and electrical transport of germanium nanowires", Journal of Applied Physics **90** (11), 5747-5751 (2001).

4. J. R. Heath, J. J. Shiang, and A. P. Alivisatos, "Germanium quantum dots: Optical properties and synthesis", Journal of Chemical Physics **101** (2), 1607-1615 (1994).

5. B. V. Kamenev, V. Sharma, L. Tsybeskov, and T. I. Kamins, "Optical properties of Ge nanowires grown on Si(100) and (111) substrates: Nanowire-substrate heterointerfaces", physica status solidi (a) **202** (14), 2753-2758 (2005).

6. C. N. R. Rao, F. L. Deepak, G. Gundiah, and A. Govindaraj, "Inorganic nanowires", Progress in Solid State Chemistry **31** (1-2), 5-147 (2003).

7. A. P. Levitt, *Whisker Technology*. (Wiley-Interscience, New York, 1970).

8. P. R. Couchman and W. A. Jesser, "Thermodynamic theory of size dependence of melting temperature in metals", Nature **269** (5628), 481-483 (1977).

9. M. Alcoutlabi and G. B. McKenna, "Effects of confinement on material behaviour at the nanometre size scale", J. Phys. Cond. Matt. **17** (15), R461-R524 (2005).

10. T. I. Kamins, X. Li, R. S. Williams, and X. Liu, "Growth and Structure of Chemically Vapor Deposited Ge Nanowires on Si Substrates", Nano Letters **4** (3), 503-506 (2004).

11. T. I. Kamins, R. S. Williams, D. P. Basile, T. Hesjedal, and J. S. Harris, "Ti-catalyzed Si nanowires by chemical vapor deposition: Microscopy and growth mechanisms", Journal of Applied Physics **89** (2), 1008-1016 (2001).

12. S. Hofmann, C. Ducati, R. J. Neill, S. Piscanec, A. C. Ferrari, J. Geng, R. E. Dunin-Borkowski, and J. Robertson, "Gold catalyzed growth of silicon nanowires by plasma enhanced chemical vapor deposition", Journal of Applied Physics **94** (9), 6005-6012 (2003).

13. Y. Wu and P. Yang, "Direct Observation of Vapor-Liquid-Solid Nanowire Growth", Journal of the American Chemical Society **123** (13), 3165-3166 (2001).

14. M. Ohring, *Material Science of Thin Films: Deposition and Structure*. (Academic Press, 2001).

15. G. Wedler, J. Walz, T. Hesjedal, E. Chilla, and R. Koch, "Stress and relief of misfit strain of Ge/Si(001)", Physical Review Letters **80** (11), 2382-2385 (1998).

16. Y. Kataoka, H. Ueba, and C. Tatsuyama, "Structural properties of heteroepitaxial Ge films on a Si(100)-2 x 1 surface", Journal of Applied Physics **63** (3), 749-759 (1988).

17. J. Tersoff, C. Teichert, and M. G. Lagally, "Self-organization in growth of quantum dot superlattices", Physical Review Letters **76** (10), 1675-1678 (1996).

18. O. G. Schmidt, O. Kienzle, Y. Hao, K. Eberl, and F. Ernst, "Modified Stranski--Krastanov growth in stacked layers of self-assembled islands", Applied Physics Letters **74** (9), 1272-1274 (1999).

19. R. L. Anderson, "Experiments on Ge-GaAs heterojunctions", Solid-State Electronics **5** (5), 341-344 (1962).

20. A. Franciosi and C. G. Van de Walle, "Heterojunction band offset engineering", Surface Science Reports **25** (1-4), 1-140 (1996).

21. L. Kleinman, "Comment on the average potential of a Wigner solid", Physical Review B **24** (12), 7412-7414 (1981).

22. J. P. Douglas, "Silicon-Germanium Strained Layer Materials in Microelectronics", Advanced Materials **11** (3), 191-204 (1999).

23. G. Abstreiter, H. Brugger, T. Wolf, H. Jorke, and H. J. Herzog, "Strain-induced two-dimensional electron gas in selectively doped Si/Si_xGe_{1-x} superlattices", Physical Review Letters **54** (22), 2441-2444 (1985).

24. C. G. Van de Walle and R. M. Martin, "Theoretical calculations of heterojunction discontinuities in the Si/Ge system", Physical Review B **34** (8), 5621-5634 (1986).

25. C. G. Van de Walle, "Band lineups and deformation potentials in the model-solid theory", Physical Review B **39** (3), 1871-1883 (1989).

26. D. V. Lang, R. People, J. C. Bean, and A. M. Sergent, "Measurement of the band gap of Ge_xSi_{1-x}/Si strained-layer heterostructures", Applied Physics Letters **47** (12), 1333-1335 (1985).

27. C. Herring and E. Vogt, "Transport and deformation-potential theory for many-valley semiconductors with anisotropic scattering", Physical Review **101** (3), 944-961 (1956).

28. R. People, "Indirect band gap of coherently strained Ge_xSi_{1-x} bulk alloys on (001)

silicon substrates", Physical Review B **32** (2), 1405-1408 (1985).

29. M. M. Rieger and P. Vogl, "Electronic-band parameters in strained $Si_{1-x}Ge_x$ alloys on $Si_{1-y}Ge_y$ substrates", Physical Review B **48** (19), 14276-14287 (1993).

30. K. Brunner, "Si/Ge nanostructures", Reports on Progress in Physics **65** (1), 27-72 (2002).

31. Y. Shiraki and A. Sakai, "Fabrication technology of SiGe hetero-structures and their properties", Surface Science Reports **59** (7-8), 153-207 (2005).

32. O. G. Schmidt, K. Eberl, and Y. Rau, "Strain and band-edge alignment in single and multiple layers of self-assembled Ge/Si and GeSi/Si islands", Physical Review B **62** (24), 16715-16720 (2000).

33. O. G. Schmidt and K. Eberl, "Multiple layers of self-assembled Ge/Si islands: Photoluminescence, strain fields, material interdiffusion, and island formation", Physical Review B - Condensed Matter and Materials Physics **61** (20), 13721-13729 (2000).

34. M. Larsson, A. Elfving, P. O. Holtz, G. V. Hansson, and W. X. Ni, "Luminescence study of Si/Ge quantum dots", Physica E: Low-dimensional Systems and Nanostructures **16** (3-4), 476-480 (2003).

35. Q. Tang, X. Liu, T. I. Kamins, G. S. Solomon, and J. S. Harris, "Twinning in $TiSi_2$-island catalyzed Si nanowires grown by gas-source molecular-beam epitaxy", Applied Physics Letters **81** (13), 2451-2453 (2002).

36. J. L. Taraci, J. W. Dailey, T. Clement, D. J. Smith, J. Drucker, and S. T. Picraux, "Nanopillar growth mode by vapor-liquid-solid epitaxy", Applied Physics Letters **84** (26), 5302-5304 (2004).

37. M. Lu, M.-K. Li, L.-B. Kong, X.-Y. Guo, and H.-L. Li, "Synthesis and characterization of well-aligned quantum silicon nanowires arrays", Composites Part B: Engineering **35** (2), 179-184 (2004).

38. I. H. Campbell and P. M. Fauchet, "EFFECTS OF MICROCRYSTAL SIZE AND SHAPE ON THE ONE PHONON RAMAN SPECTRA OF CRYSTALLINE SEMICONDUCTORS", Solid State Communications **58** (10), 739-741 (1986).

39. B. Li, D. Yu, and S.-L. Zhang, "Raman spectral study of silicon nanowires", Physical Review B **59** (3), 1645 (1999).

40. Y. F. Zhang, Y. H. Tang, N. Wang, C. S. Lee, I. Bello, and S. T. Lee, "Germanium nanowires sheathed with an oxide layer", Physical Review B **61** (7), 4518-4521 (2000).

41. P. Y. Yu and M. Cardona, *Fundamentals of semiconductors: Physics and*

Materials Properties. (Springer-Verlag, New York, 2001).

42. P. J. Dean, J. R. Haynes, and W. F. Flood, "New radiative recombination processes involving neutral donors and acceptors in silicon and germanium", Physical Review **161** (3), 711-729 (1967).

43. Z. G. Bai, D. P. Yu, J. J. Wang, Y. H. Zou, W. Qian, J. S. Fu, S. Q. Feng, J. Xu, and L. P. You, "Synthesis and photoluminescence properties of semiconductor nanowires", Materials Science and Engineering B **72** (2-3), 117-120 (2000).

44. B. J. Pawlak, T. Gregorkiewicz, and C. A. J. Ammerlaan, "Alteration of band structure in Si nanocrystals", Materials Science and Engineering: C **15** (1-2), 273-275 (2001).

45. S.-W. Chung, J.-Y. Yu, and J. R. Heath, "Silicon nanowire devices", Applied Physics Letters **76** (15), 2068-2070 (2000).

46. Y. Cui, X. Duan, J. Hu, and C. M. Lieber, "Doping and Electrical Transport in Silicon Nanowires", Journal of Physical Chemistry B **104** (22), 5213-5216 (2000).

47. D. J. Eaglesham and M. Cerullo, "Dislocation-free Stranski-Krastanow growth of Ge on Si(100)", Physical Review Letters **64** (16), 1943-1946 (1990).

48. Y. W. Mo and M. G. Lagally, "Scanning tunneling microscopy studies of the initial stages of germanium growth on Si(001)", Materials Science and Engineering B **14** (3), 311-316 (1992).

49. J. M. Baribeau, D. C. Houghton, T. E. Jackman, and J. P. McCaffrey, "Molecular beam epitaxy growth of Ge on (100) Si", Journal of the Electrochemical Society **136** (4), 1158-1162 (1989).

50. G. Medeiros-Ribeiro, A. M. Bratkovski, T. I. Kamins, D. A. A. Ohlberg, and R. S. Williams, "Shape transition of germanium nanocrystals on a silicon (001) surface from pyramids to domes", Science **279** (5349), 353-355 (1998).

51. F. M. Ross, R. M. Tromp, and M. C. Reuter, "Transition states between pyramids and domes during Ge/Si island growth", Science **286** (5446), 1931-1934 (1999).

52. J. M. Baribeau, X. Wu, N. L. Rowell, and D. J. Lockwood, "Ge dots and nanostructures grown epitaxially on Si", Journal of Physics: Condensed Matter **18** (8), R139-R174 (2006).

53. J. Weber and M. I. Alonso, "Near-band-gap photoluminescence of Si-Ge alloys", Physical Review B **40** (8), 5683-5693 (1989).

54. R. Apetz, L. Vescan, A. Hartmann, C. Dieker, and H. Luth, "Photoluminescence and electroluminescence of SiGe dots fabricated by island growth", Applied Physics Letters **66** (4), 445-447 (1995).

55. S. S. Iyer and Y. H. Xie, "Light emission from silicon", Science **260** (5104), 40-46 (1993).

56. U. Gnutzmann and K. Clausecker, "Theory of direct optical transitions in an optical indirect semiconductor with a superlattice structure", Applied Physics **3** (1), 9-14 (1974).

57. S. Satpathy, R. M. Martin, and C. G. Van de Walle, "Electronic properties of the (100) (Si)/(Ge) strained-layer superlattices", Physical Review B **38** (18), 13237-13245 (1988).

58. H. Presting, H. Kibbel, M. Jaros, R. M. Turton, U. Menczigar, G. Abstreiter, and H. G. Grimmeiss, "Ultrathin SimGen strained layer superlattices - A step towards Si optoelectronics", Semiconductor Science and Technology **7** (9), 1127-1148 (1992).

59. K. Eberl, O. G. Schmidt, S. Schieker, N. Y. Jin-Phillipp, and F. Phillipp, "Formation and optical properties of carbon-induced Ge dots", Solid-State Electronics **42** (7-8), 1593-1597 (1998).

60. J. Wan, G. L. Jin, Z. M. Jiang, Y. H. Luo, J. L. Liu, and K. L. Wang, "Band alignments and photon-induced carrier transfer from wetting layers to Ge islands grown on Si(001)", Applied Physics Letters **78** (12), 1763-1765 (2001).

61. V. Belyavskii and S. Shevtsov, "Inhomogeneous broadening of the ground electron level in a quantum dot array", Semiconductors **36** (7), 821-827 (2002).

62. S. K. Zhang, H. J. Zhu, F. Lu, Z. M. Jiang, and X. Wang, "Coulomb charging effect in self-assembled Ge quantum dots studied by admittance spectroscopy", Physical Review Letters **80** (15), 3340-3343 (1998).

63. H. Zhou, S. Huang, Y. Rao, Z. Jiang, and F. Lu, "Quantum levels in Ge quantum dots studied by photocurrent spectroscopy and admittance spectroscopy", Solid State Communications **125** (3-4), 161-164 (2003).

64. A. Dvurechenskii and A. Yakimov, "Type-II Ge/Si quantum dots", Semiconductors **35** (9), 1095-1105 (2001).

65. J. M. Baribeau, T. E. Jackman, D. C. Houghton, P. Maigne, and M. W. Denhoff, "Growth and characterization of $Si_{1-x}Ge_x$ and Ge epilayers on (100) Si", Journal of Applied Physics **63** (12), 5738-5746 (1988).

66. J. M. Baribeau, D. J. Lockwood, M. W. Lockwood, M. W. C. Dharma-Wardana, N. L. Rowell, and J. P. McCaffrey, "Growth and characterization of Si-Ge atomic layer superlattices", Thin Solid Films **183** (1-2), 17-24 (1989).

67. N. L. Rowell, J. P. Noel, D. C. Houghton, A. Wang, L. C. Lenchyshyn, M. L. W. Thewalt, and D. D. Perovic, "Exciton luminescence in $Si_{1-x}Ge_x$/Si

heterostructures grown by molecular beam epitaxy", Journal of Applied Physics **74** (4), 2790-2805 (1993).

68. H. K. Shin, D. J. Lockwood, and J. M. Baribeau, "Strain in coherent-wave SiGe/Si superlattices", Solid State Communications **114** (10), 505-510 (2000).

69. M. Pollak and T. H. Geballe, "Low-frequency conductivity due to hopping processes in silicon", Physical Review **122** (6), 1742-1753 (1961).

70. E.-K. Lee, B. V. Kamenev, L. Tsybeskov, S. Sharma, and T. I. Kamins, "Carrier transport in Ge nanowire/Si substrate heterojunctions", Journal of Applied Physics **101** (10), 104303-104304 (2007).

71. T. Hanrath and B. A. Korgel, "Influence of Surface States on Electron Transport through Intrinsic Ge Nanowires", Journal of Physical Chemistry B **109** (12), 5518-5524 (2005).

72. T. Baier, U. Mantz, K. Thonke, R. Sauer, F. Schafler, and H. J. Herzog, "Type-II band alignment in $Si/Si_{1-x}Ge_x$ quantum wells from photoluminescence line shifts due to optically induced band-bending effects: Experiment and theory", Physical Review B **50** (20), 15191-15196 (1994).

73. Landolt-Börnstein, *Numerical Data and Functional Relationships in Science and Technology*. (Springer-Verlag, New York, 1982).

74. J. B. Gunn, "Microwave oscillations of current in III-V semiconductors", Solid State Communications **1** (4), 88-91 (1963).

75. Y. Zhang, X. Yang, W. Liu, P. Zhang, and D. Jiang, "New formation mechanism of electric field domain due to Gamma-X sequential tunneling in GaAs/AlAs superlattices", Applied Physics Letters **65** (9), 1148-1150 (1994).

76. E. E. Mendez, E. Calleja, and W. I. Wang, "Tunneling through indirect-gap semiconductor barriers", Physical Review B **34** (8), 6026-6029 (1986).

77. Y. Wu, Y. Cui, L. Huynh, C. J. Barrelet, D. C. Bell, and C. M. Lieber, "Controlled Growth and Structures of Molecular-Scale Silicon Nanowires", Nano Letters **4** (3), 433-436 (2004).

78. V. Schmidt, S. Senz, and U. Gosele, "Diameter-Dependent Growth Direction of Epitaxial Silicon Nanowires", Nano Letters **5** (5), 931-935 (2005).

79. B. L. Yang, P. T. Lai, and H. Wong, "Conduction mechanisms in MOS gate dielectric films", Microelectronics Reliability **44** (5), 709-718 (2004).

80. C. Williams, "Kinetics of trapping, detrapping, and trap generation", Journal of Electronic Materials **21** (7), 711-720 (1992).

81. B. V. Kamenev, L. Tsybeskov, J. M. Baribeau, and D. J. Lockwood, "Coexistence of fast and slow luminescence in three-dimensional $Si/Si_{1-x}Ge_x$ nanostructures", Physical Review B (Condensed Matter and Materials Physics) **72** (19), 193306-193304 (2005).

82. B. V. Kamenev, E.-K. Lee, H. Y. Chang, H. Han, H. Grebel, L. Tsybeskov, and T. I. Kamins, "Excitation-dependent photoluminescence in Ge/Si Stranski-Krastanov nanostructures", Applied Physics Letters **89** (15), 153106-153103 (2006).

83. V. Le Thanh, V. Yam, P. Boucaud, F. Fortuna, C. Ulysse, D. Bouchier, L. Vervoort, and J. M. Lourtioz, "Vertically self-organized Ge/Si(001) quantum dots in multilayer structures", Physical Review B **60** (8), 5851-5857 (1999).

84. P. Lautenschlager, P. B. Allen, and M. Cardona, "Temperature dependence of band gaps in Si and Ge", Physical Review B **31** (4), 2163-2171 (1985).

85. P. Boucaud, V. Le Thanh, V. Yam, S. Sauvage, N. Meneceur, M. Elkurdi, D. Dèbarre, and D. Bouchier, "Aspects of Ge/Si self-assembled quantum dots", Materials Science and Engineering B **89** (1-3), 36-44 (2002).

86. L. C. Lenchyshyn, M. L. W. Thewalt, J. C. Sturm, P. V. Schwartz, E. J. Prinz, N. L. Rowell, J. P. Noel, and D. C. Houghton, "High quantum efficiency photoluminescence from localized excitons in $Si_{1-x}Ge_x$", Applied Physics Letters **60** (25), 3174-3176 (1992).

87. Y. Shiraki, H. Sunamura, N. Usami, and S. Fukatsu, "Formation and optical properties of SiGe/Si quantum structures", Applied Surface Science **102**, 263-271 (1996).

88. S. S. Rhee, G. K. Chang, T. K. Carns, and K. L. Wang, "SiGe resonant tunneling hot-carrier transistor", Applied Physics Letters **56** (11), 1061-1063 (1990).

89. R. Duschl, O. G. Schmidt, and K. Eberl, "Epitaxially grown Si/SiGe interband tunneling diodes with high room-temperature peak-to-valley ratio", Applied Physics Letters **76** (7), 879-881 (2000).

90. H. Qin, A. W. Holleitner, K. Eberl, and R. H. Blick, "Coherent superposition of photon- and phonon-assisted tunneling in coupled quantum dots", Physical Review B **64** (24), 241302-241305 (2001).

91. B. V. Kamenev, L. Tsybeskov, J. M. Baribeau, and D. J. Lockwood, "Photoluminescence and Raman scattering in three-dimensional $Si/Si_{1-x}Ge_x$ nanostructures", Applied Physics Letters **84** (8), 1293-1295 (2004).

92. J. Shah and A. H. Dayem, "Formation of electron-hole liquid in optically excited Si: Results of fast time-resolved spectroscopy", Physical Review Letters **37** (13), 861-864 (1976).

93. M. Tajima and S. Ibuka, "Luminescence due to electron-hole condensation in silicon-on-insulator", Journal of Applied Physics **84** (4), 2224-2228 (1998).

94. C. J. Williams, E. Corbin, M. Jaros, and D. C. Herbert, "Auger recombination in strained SixGe1-x/Si superlattices", Physica B: Condensed Matter **254** (3-4), 240-248 (1998).

95. W. Seidel, A. Titkov, J. P. Andr, P. Voisin, and M. Voos, "High-efficiency energy up-conversion by an "Auger fountain" at an InP-AlInAs type-II heterojunction", Physical Review Letters **73** (17), 2356-2359 (1994).

96. W. F. Brinkman and T. M. Rice, "Electron-hole liquids in semiconductors", Physical Review B **7** (4), 1508-1523 (1973).

97. J. C. Hensel and R. C. Dynes, "Interaction of electron-hole drops with ballistic phonons in heat pulses: The phonon wind", Physical Review Letters **39** (15), 969-972 (1977).

98. M. E. Msall and J. P. Wolfe, "Phonon production in weakly photoexcited semiconductors: Quasidiffusion in Ge, GaAs, and Si", Physical Review B **56** (15), 9557-9564 (1997).

99. J. D. Cuthbert, "Recombination kinetics of excitonic molecules and free excitons in intrinsic silicon", Physical Review B **1** (4), 1552-1557 (1970).

100. W. Gerlach, H. Schlangenotto, and H. Maeder, "On the radiative recombination rate in silicon", Physica Status Solidi (A) Applied Research **13** (1), 277-283 (1972).